Autonomous Fire Suppression Using Feedback Control for a Firefighting Robot

Joshua G. McNeil

Dissertation submitted to the faculty of the Virginia Polytechnic Institute and State University in partial fulfillment of the requirements for the degree of

Doctorate of Philosophy
In
Mechanical Engineering

Brian Y. Lattimer, Co-Chair
Alexander Leonessa, Co-Chair
Kevin B. Kochersberger
Daniel D. Lee
Alfred L. Wicks

December 14, 2015
Blacksburg, VA

Keywords: firefighting robot, fire suppression, water classification, probabilistic classification, trajectory modeling, feedback control

Autonomous Fire Suppression Using Feedback Control for a Firefighting Robot

Joshua G. McNeil

ABSTRACT

There is an increasing demand for robotics in dangerous and extreme conditions to limit human exposure and risk. An area in which robots are being considered as a support tool is in firefighting operations to reduce the number of firefighter injuries and deaths. One such application is to increase firefighting performance through localized fire suppression.

This research focused on developing an autonomous suppression system for use on a mobile robotic platform. This included a real-time close proximity fire suppression approach, appropriate feature selection and probabilistic classification of water leaks and sprays, real-time trajectory estimation, and a feedback controller for error correction in longer-range firefighting. The close proximity suppression algorithm uses IR fire detection IR stereo processing to localize a fire. Feedback of the fire size and fire target was used to manipulate the nozzle for effective placement of the suppressant onto the fire and experimentally validated with tests in high and low visibility environments.

To improve performance of autonomous suppression and for inspection tasks, identification of water sprays and leaks is a critical component. Bayesian classification was used to identify the features associated with water leaks and sprays in thermal images. Appropriate first and second order features were selected by using a multi-objective genetic algorithm optimization. Four textural features were selected as a method of discriminating water sprays and leaks from other non-water, high motion objects.

Water classification was implemented into a real-time suppression system as a method of determining the yaw and pitch angle of a water nozzle. Estimation of the angle orientation provided an error estimate between the current path and desired nozzle orientation. A proportional-integral (PI) controller was used to correct for forced errors in fire targeting and performance and response was shown through indoor and outdoor suppression tests with wood-crib fires. The autonomous suppression algorithm was demonstrated through fire testing to be at least three times faster compared with suppression by an operator using tele-operation.

Acknowledgements

I would like to thank the following people without whom this goal could not have been achieved:

The greatest thanks goes to Liz, who has always been supportive and keeps me happy and looking forward to coming home after a long day.

My family and friends for their love, unending support and confidence in me without which I could not achieve this.

Dr. Brian Lattimer for the countless hours of advising and discussions on such a cool and challenging project. Your expertise and support have helped me become a better researcher and engineer.

Drs. Leonessa, Kochersberger, Wicks, Lee, and Asbeck, for their time and knowledge and willingness to be a part of my committee.

Joseph Starr for friendship and knowledge and willingness to always help with the numerous experiments and setups, coding projects and issues, and research discussions through the years.

All other members of the EXTREME Lab (Jong, Brian, Christian, Nahid, Jonathan, Robert, Yoon, etc.) for friendship, advice, and all your help with research and experiments.

The entire Mechanical Engineering Department for all your work behind the curtain making sure research projects run smoothly.

The Office of Naval Research for sponsoring this research.

Table of Contents

List of Figures

List of Tables

1 Introduction

1.1 Motivation

In 2013, 65,880 firefighters in the U.S. alone were injured in the line of duty with 64 deaths in 2014 [1-4]. In addition to injuries on-duty, there exists the risk of exposure to infectious diseases and hazardous conditions. The leading causes of injury include overexertion or strain (26.5%), falling or slipping (22.7%), exposure to fire products, chemicals, or radiation (12.6%), and contact with objects (12%) [3-5]. Conditions inside of structure fires and wildland fires range from clear to zero visibility which influences human behavior [6-9] in addition to making firefighting difficult [3,4]. Firefighting robots are beginning to be considered as a support tool to reduce firefighter risk and increase performance. One aspect of the firefighting robot is a system that autonomously detects and suppresses fires in the field of view. Effective suppression tactics can reduce the amount of water used which decreases the amount of water damage. Water damage can often exceed fire damage, especially in structure fires that use sprinkler systems or where external application of water is not well targeted onto the fire.

Robots such as Rainbow 5 in Japan [10], LUF60 in Germany [11], and F2GB [11] are remotely controlled to suppress fires using large spray pattern hoses and are designed for outdoor firefighting due to the size of the platforms. Indoor operating firefighting robots include FireSearcher [10], Tehzzeb [12], QinetiQ [13], Firemote 4800 [14], and Archibot [14]. These robots include vision sensors to assist an operator in assessing the situation of dangerous environments from a safe distance and make decisions on how to proceed [15] or in identifying and communicating with humans in the environment. The limitations of remote control of these robots are reliance on limited information provided to the operator by the robot in a given situation, lack of control of multiple robots by a single operator, and limitations in wireless communication causing unstable connections for data collection and processing or failures in the system during operation. Remote controlled robots will ultimately lead to fully autonomous systems in the future.

The number of autonomous firefighting robots are limited. AFFMP from Malaysia [16] extinguishes small flames using a mounted fan. Hoyarobot [17] is a support tool for relaying information back to operators and voice communication with victims. FINE [14] is designed to extinguish small fires inside homes but details are not publically accessible. The other area of

autonomous suppression research is in fixed systems known as fire monitors which are often positioned in high-clearance warehouses or other storage areas [20]. Fire monitors use an imaging system, visual or IR, mounted on top of a water nozzle which is manipulated using a pan-tilt system. The monitor is alerted with externally placed fire detectors and begin searching a space for a fire using a narrow band indicator mounted rigidly with a high pressure water nozzle. Upon detection, the nozzle is actuated in a circular or sweeping pattern in an attempt to extinguish the fire until no longer detected. A linear assumption is made between the nozzle origin and the detected flame area. Chen et. al [19] developed an automatic fire searching system using remote-controlled fire monitors based on one CCD camera fixed at the end of the fire monitor nozzle.

In large areas, the time it takes for smoke particulate or heat to reach detectors may lead to larger fires and propagation of flames. Video based detection is an active area of research to serve detection of fire in larger spaces or outdoors. While the fire can be detected and system alerted using a number of different strategies, how to put out the fire still needs to be addressed. Inefficient application of water can lead to more water damage than that done by fire to property and other valuables. Some automatic jet fire extinguishing devices have been designed [18] but the accuracy of the devices will reduce in windy conditions and there is no accounting for errors in the initial placement of the water jet. Due to the limitations of the one camera system, response and scanning times of these systems can be improved [20].

The shipboard autonomous firefighting robot (SAFFiR), the first autonomous humanoid firefighting robot, has been developed at Virginia Tech to locate and suppress fires onboard naval ships and inside structures. An early prototype of SAFFiR suppressing a wood-crib fire is shown in Fig. 1.1. Advancements in intelligent algorithms and perception have been developed in this project [21-26]. The research on firefighting robots has not shown results of full scale fires being suppressed autonomously to validate the suppression algorithms.

Figure 1.1. The Shipboard Autonomous Firefighting Robot (SAFFiR) onboard the ex-USS Shadwell.

In order for robots to autonomously suppress fires, this study presents an autonomous fire suppression algorithm with feedback control. The proposed system enables the robot to analyze local conditions using long wavelength IR camera images. Infrared was chosen as the primary vision sensor due to performance in imaging through low visibility environments [24]. Image processing allows the system to detect and classify fire and water sprays by characterizing regions of interest based on textural features. Feedback of the fire location and size is used in a closed-loop control scheme to manipulate a nozzle to accurately suppress the fire and adjust according to errors in spray placement.

1.2 Objectives

This work is presented in the following chapters structured in the form of papers with relevant literature review of each topic. The chapters are organized in the following manner:

- Chapter 2 – *A real-time close proximity fire suppression strategy was developed through integrating fire detection, IR stereo vision, and visual servoing for fire suppression.* The feedback control is used to manipulate a nozzle in a form of visual servoing to intelligently actuate the nozzle based on changes in the fire size and target location. Suppression algorithms proposed in previous studies on fire monitors rely on a binary fire detector indicating whether the flame is in the field of view (FOV) and do not adjust spray location based on the fire behavior.
- Chapter 3 – *A method for classifying water leaks and sprays through IR images was developed to allow for tracking of these real time.* This was primarily performed to allow for real time track of the water spray relative to the fire for suppression with feedback control. The optimal combination of features (e.g. texture, intensity, variance) in thermal images that classify water and non-water dynamic regions was analyzed using multi-objective genetic optimization. This is the first research to perform real time classification of water sprays with IR images.
- Chapter 4 – *A predicted spray trajectory was developed based on the vision system measurement of the spray location as well as a physics based model for the spray trajectory.* This allows for the robot to predict where the spray will land beyond where it may be apparent through the vision system. Stereoscopic IR images were used to map the spray trajectory in three-dimensional coordinates, and the spray location from the vision system was fit to a spray trajectory model. An estimation of the yaw and pitch angles nozzle was used to determine the error between the current spray angles and desired placement based on fire localization and model predictions. Previous research in other studies assume straight line trajectories, which becomes inaccurate at longer distances and does not account for external effects on the spray or errors in the nozzle pitch-yaw angle.
- Chapter 5 – *A real-time autonomous suppression algorithm was developed with feedback control and visual servoing through integrating the research in Chapters 2-4.* The water classification and error estimation technique in Chapter 4 was implemented for real-time processing. A decision tree control scheme was used to determine the best approach to

suppressing a wood-crib fire based on IR image feedback. A PI controller with Kalman filtering was implemented to reduce the error between desired spray angles and estimated angles. Previous work in autonomous suppression research has not included the feedback control and visual servoing that accounts for the fire behavior. For the algorithm developed in this work, the performance and response of algorithm integrated with a water spray hardware system was shown through full scale experiments in indoor and outdoor environments. The tests performed included forced offsets to intentionally place the suppressant off-target of the fire.

2 Autonomous Fire Suppression for Use in High and Low Visibility Environments by Visual Servoing

2.1 Abstract

An autonomous fire suppression system was developed for localized fire suppression in high and low visibility environments. The system contains a multispectral sensor suite, including UV sensors and infrared stereo vision, to detect and target a fire for suppression. The UV sensor provides an alert to the system to begin fire detection. IR imagery is used to segment fire from the field of view and target the base of the fire and IR stereo vision to determine the 3D coordinates of the fire. IR tracking provides continuously updated information on the size and intensity of the fire before and during suppression and alerts the system when to cease suppression activity. Visual servoing is used to correctly position a nozzle based on feedback of changes in the fire location and size. The autonomous system was used to suppress wood crib fires (40-50 kW) in high and low visibility environments and at varying distances (2.8-5.5 m) and elevations (0.4-1.3 m). The suppression time in clear conditions was 3.72 s ± 1.51 s and 4.49 s ± 1.62 s in low visibility conditions. To simulate wind effects and inaccurate initial target coordinates, forced offsets were input to the system to show effectiveness of the feedback control algorithm when an initial estimate of spray trajectory does not accurately spray the center base of the fire. System performance with a forced offset resulted in suppression times of 4.11 s ± 0.84 s.

2.2 Introduction

Firefighting operations can be very dangerous due to low visibility, high temperature, smoke filled environments. In 2013, an estimated 65,880 firefighters in the U.S. were injured while fighting fires resulting in 97 deaths [2, 3]. The leading causes of injury were overexertion or strain. A shipboard autonomous firefighting robot program was recently initiated to locate and suppress fires onboard ships as well as support firefighters by reducing exposure and helping to effectively suppress fires in low visibility conditions. Advancements through the program have been on perception systems [21-25] and autonomous suppression strategy [26] that can be integrated onto a mobile humanoid robot. A robust suppression strategy can target and attack a fire in low visibility

environments where a firefighter might rely on instinct or a handheld thermal infrared camera (TIC) to help apply the suppressant and determine when the fire is fully suppressed.

An autonomous robotic fire suppression strategy requires use of a multi-spectral sensor suite that can provide useful information to make decisions on when to activate a suppressing agent, manipulation of the nozzle, adjustment of the spray location, and when to stop agent application. Various firefighting robots have been developed for indoor and outdoor purposes [10, 17, 27-31], but they rely on remote control by an operator. Attempts at autonomous fire detection and suppression systems have been pursued on a small conceptual scale [31]. A fire monitor system was developed for use with a single RGB camera for fire localization [19]; however, the system performance was not shown in low visibility environments nor did it implement feedback control to adjust the spray to more effectively reach the fire. Another system integrates fire detection with a suppression system based on video surveillance [32]. This relies on visual cameras to accumulate motion features for fire and smoke detection, which is not applicable to fire smoke environments. The system described uses a fire detector that is able to automatically adjust the nozzle but detailed information on how this is done is not provided. Work has been reported on a robotic nozzle for tunnel applications [33] to plan a spray trajectory and keep the system at a safe distance from a fire, but the system was only developed on a conceptual level.

Forms of automatic fire monitor systems have been evaluated [34] and there exists national standards in China (GB25204-2010) for fire monitor suppression systems. Fire monitors are typically used in high storage facilities and use a wide FOV fire detector to alert the monitor to begin a search of the coverage area. A smaller flame detector is mounted on top of a water cannon and searches the space until flames are present at which time the water cannon begins spraying until fully suppressed. These systems do not implement feedback control systems to adjust the nozzle direction if the spray does not reach the fire or only a portion of the fire is reached by the suppressant. The performance of these systems in low visibility environments where the detector and vision system can be obstructed due to smoke has not been presented. The advantage of a robotic firefighter over these systems is in compact spaces and compartments where ceiling mounted systems are not effective due to blockage of a fire detector due to obstacles or fires located in areas out of the coverage area of searching fire monitors.

Many of the early fire or smoke detection systems and integrated suppression systems use RGB cameras due to their low weight and power consumption as well as the color, shape, motion, and texture information obtained. Online image databases are used to support algorithm development, which often use empirical parameters to define when a pixel is associated with a fire object [34-38]. The inherent performance of such algorithms often depends on lighting conditions that highly vary based on shadows or darkness. In addition, these cameras operate in the visible or near IR wavelength range making them often unusable in smoke-filled environments.

For suppression activities conducted in indoor environments and enclosures, the resulting water vapor and smoke mixture that builds up once suppression begins can block a firefighter's view of the fire. Figure 2.1 shows a wood crib fire burning onboard a naval ship and the resulting mixture of steam once the fire suppression has begun. The firefighter is no longer able to locate the fire in order to accurately position the firefighting nozzle.

Figure 2.1. Fully developed wood crib fire and water vapor/smoke mixture during suppression

Firefighters often use TICs [39-42] and IR cameras operating in the long wavelength range (7-14 μm), which have been shown to be effective in a wide variety of areas because they are able to image through high concentrations of obscurant and highlight high temperature features. This includes forest fire monitoring from satellites [43], ground installed cameras [44], tunnel fire detection [45], and surveillance of cargo holds in aircraft [46]. They also have been shown to locate a fire through zero visibility conditions produced by the interaction of sprinkler systems and fires. While these applications provide a 2D view of the environment, localization of a fire target needs to be performed with a system that provides 3D information such as a stereo vision system. Far infrared (IR) stereo vision systems have been shown to track people in normal atmospheric

conditions [47] and provide depth maps in clean conditions [48]. The benefits of IR cameras make them an ideal sensor for use in a suppression system where dense smoke and significant water vapor is commonly present.

This paper presents an autonomous suppression strategy for use in clear and low visibility environments that implements visual servoing and feedback control for localized fire suppression. The system includes a UV sensor for redundancy in fire detection and dual IR thermal cameras in a stereoscopic setup for localizing a fire. IR images were also used to segment the fire from the scene, calculate the size of the fire, and target the fire location throughout the suppression process in a feedback control decision tree. The fire is localized using an IR stereo vision system that provides distance information for objects that have been matched in a pair of images. Data from the thermal cameras was used to effectively position a water nozzle spray onto a single wood crib fire. Results from fire suppression tests are presented to demonstrate the efficacy of the system in clear and low visibility environments with fires placed at various positions relative to the system. Experiments were also conducted to compare the autonomous system performance with manual suppression tests in a smoke filled environment as well as performance of the system when the initial fire coordinates are intentionally offset to test the feedback control process.

2.3 System Development

The autonomous system uses multispectral sensors to carry out all tasks involved in suppressing a fire. The sensors used in the system setup are shown in Figure 2.2. A UV sensor was placed between two FLIR A35 IR cameras. A visual camera was mounted along the same plane and to the right of the IR cameras, and a nozzle was mounted on a yaw-pitch servo motor mechanism below the sensor suite. The yaw-pitch controller used two Robotis Dynamixel MX-106T motors with resolution of 0.088 degrees per step. A secondary visual camera was placed behind the nozzle to record the suppression process and nozzle movement during testing. A solenoid valve was placed inline 1.5 m behind the nozzle and was automatically opened and closed with on and off commands within the algorithm. The suppression system was operated at 50-60 psi with a flow rate of 10-12 GPM. The nozzle setting used will cover over 3 m^2 at the base of the target. For various pressures and angles the mass flux rate is over 2.75 kg/m^2-s. This mass flux rate along with the droplet diameter size is over the 0.37 to 1.15 kg/m^2-s minimum mass flux proven

to be effective in suppressing Class A material fires for light hazard occupancy (<500 kW) [49-50].

All sensors were used with National Instruments LabVIEW for data collection, processing and control. Once the UV sensor and IR cameras indicate a fire has been detected, the system uses the process shown in Figure 2.3. The fire is localized and nozzle positioned in an initial attack position to begin suppression. Information about the fire position and size throughout the process is used to effectively move the nozzle using a visual servoing method. The processes involved in the total autonomous system include a fire indicator, fire identification, localization, and feedback control.

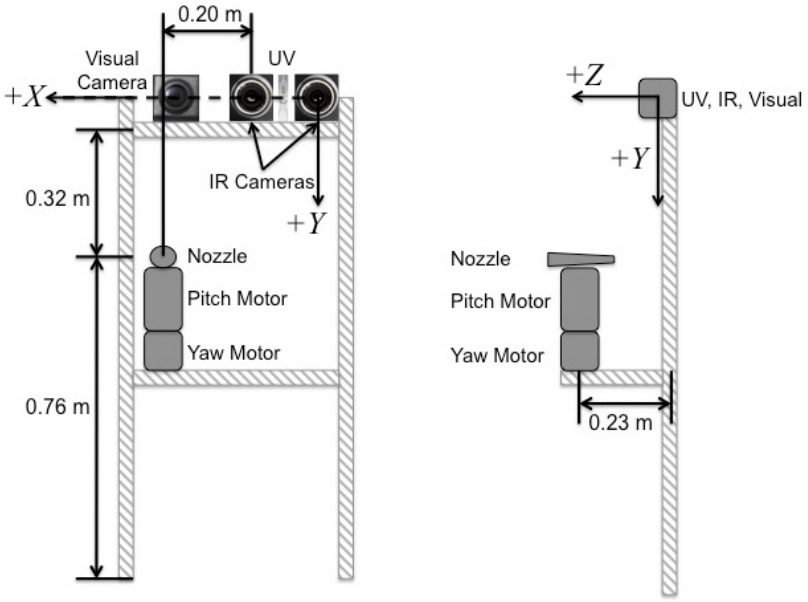

Figure 2.2. Sensors and dimensions of autonomous suppression system

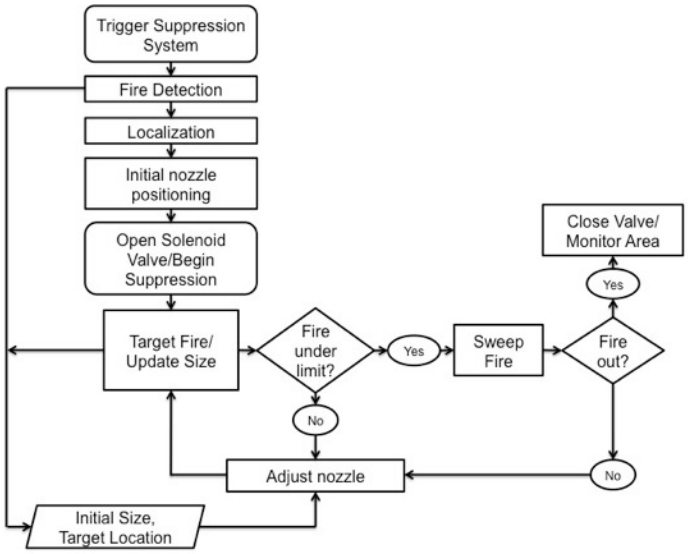

Figure 2.3. Autonomous suppression algorithm flow chart

2.3.1 UV Fire Detection

Previous work has shown UV detectors [51], and UV light emitting diodes [52, 53] are successful in many applications e.g. flame detection, UV imaging, and solar UV detection. There are many commercial UV detection sensors available that can detect UV radiation emitted from long ranges but cannot determine the position due to the large field of view of the sensors. Their sensitivity to UV allows them to be used as an early fire detection sensor.

A Hamamatsu UVTron sensor [54] was selected to identify the presence of a fire. It has a peak spectral response in a narrow band of ultraviolet radiation from 185 nm to 260 nm. This makes it insensitive to visible light along with sunlight and ideal for indoor flame detection in the presence of indoor light. The UVTron has a viewing range of 60 degrees and is capable of detecting a flame from a match or lighter up to 5 m away. The sensor is housed to limit the horizontal field of view to that of the IR stereo vision system. This ensures the fire detected by the sensor is within the field of view of the IR cameras. When UV light is emitted from a flame and collected by the sensor, 10 μs signal pulses are generated from the cathode. The frequency of these pulses indicates the quantity of incident UV light as shown in Figure 2.4. Through experiments carried out with the sensors, 5 or more signal pulses in a one second interval is a strong indicator of flames present and alerts the system to identify the fire using IR.

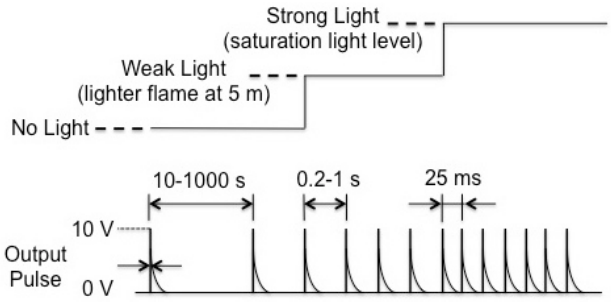

Figure 2.4. UV sensor output response to ultraviolet radiation

2.3.2 IR Fire Detection and Segmentation

The fire was also identified using the IR images. In smoke conditions where UV may not detect a fire present, the system uses IR to identify the fire in the field of view. In many firefighting applications, the base of the fire is targeted for suppressing in order to wet the fuel source. FLIR A35 long wavelength (7-14 μm) IR cameras are used in the testing reported herein. The cameras use an uncooled VOX microbolometer outputting 14-bit data with a 320 x 256-pixel focal plane array and a frame rate of 10 Hz. It has been shown that adaptive background subtraction and classification is a more accurate approach in segmenting fire from an IR image and classifying fire, fire reflections, smoke, and smoke reflections [55]. The method uses second order texture features to probabilistically classify fire, smoke, fire reflections, smoke reflections, and hot objects. If a fire has been identified in the FOV, it can be used as the area to target initially. If reflections, hot objects, or smoke exists, a heading direction can be provided to the robot to lead the system towards a potential fire. Once the fire has been identified in the IR vision system, autonomous suppression will begin.

Fire is higher in temperature (and image intensity) than the background, making intensity thresholding a useful characteristic in segmenting the fire from a thermal image. For increased processing speeds, an intensity threshold was used in this study for segmenting out fire from the IR images. The assumption was made that the largest segmented object in the IR image was the fire. Fire reflections and hot objects were smaller in size to the fire but can also be cooled after fire suppression if they are still at a high intensity above the threshold value. Potential fire pixels can be segmented using Eq. (1)

$$I_R(x_i,\ y_i) \geq K \quad (1)$$

where $\boldsymbol{I_R(x_i,\ y_i)}$ is the IR intensity value located at image location x, y and K is a threshold value. Intensities above K are defined as fire and values below K are set to zero to create a masked image. The temperature range of the cameras when used in a low gain setting is -40°C to +550°C resulting in an intensity range from -16,384 to -1. A threshold of value (K) of 300°C was used to classify fire pixels within view of the camera based on prior experiments performed in the low visibility and clear conditions used in the suppression tests. The intensity threshold resulted in little to no reflections from the fire and provided a clear segmentation of the fire in the IR image.

Processing is performed to optimize image contrast and brightness based on the minimum and maximum pixel intensity values as well as highlight segmented pixels associated with the fire as red for display. In the suppression experiments performed, the fire is the largest object in the scene and small reflections are ignored using an object size threshold. The base of the identified fire is located by using a histogram map of the IR image after the threshold as been applied. Histogram maps are made across the rows of the image as well as the columns. For a single fire scenario, the last or bottom row associated with the fire object is chosen as the targeted image row location $I_R(x_i)$ and the left and right edges of the object are averaged to identify the center column of the fire $I_R(y_i)$. An example of the display resulting from the image processing to show real-time fire detection is provided in Figure 2.5.

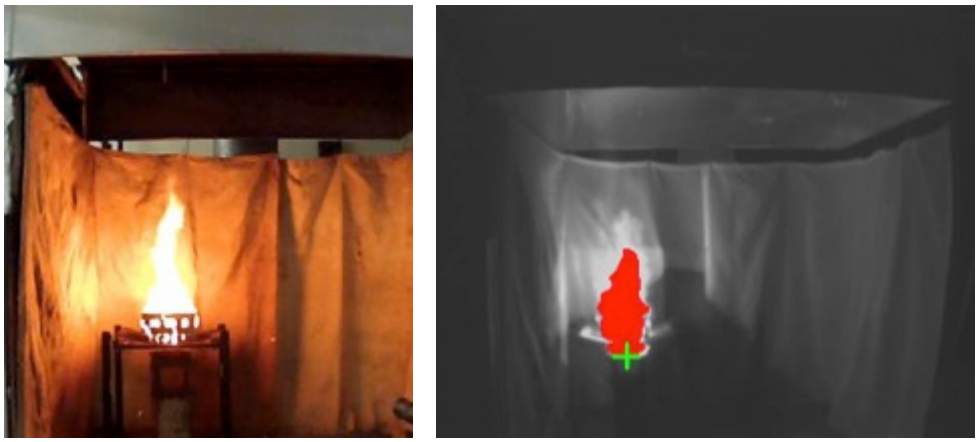

(a) (b)

Figure 2.5. Fire segmentation and targeting using IR image. (a) Visual camera (b) Green marker indicates the targeted fire location in the IR

2.3.3 Target Localization

The three-dimensional coordinates of the base of the fire must be used to plan for the application of suppressant onto the fire. Some autonomous systems rely on a single camera and nozzle being rigidly mounted together [19]. The system then attempts to estimate a distance for the fire based on the amount the target of the fire moves in consecutive images for a small change in the camera angle. For the system developed in this paper, the imaging is separate from the nozzle manipulator to show the potential application for robotic firefighting. IR cameras were selected over visual cameras to ensure a fire can be imaged in low visibility conditions produced by steam or smoke where visual camera systems fail.

The IR stereo vision system consists of two FLIR A35 thermal cameras with 9 mm lenses to provide a large field of view (FOV). The output data is down-sampled to 320x256 resolution, calibrated and rectified before using the IR images to obtain a disparity map using a bidirectional Sum of Absolute Differences (SAD) algorithm. The system has been shown to predict distances to within 9.3% in clear conditions as well as in smoke filled conditions when the visibility is less than 1 m [24, 25]. The accuracy of the system decreases the further away objects are located. The system was tested using a 0.20 m baseline to provide better accuracy for targets in the 2 m to 5 m range.

The targeted row and column image location is used along with the disparity map provided by the stereo vision system to provide the initial 3D coordinates of the fire using Eqs. (2-6)

$$Z_O = f\frac{B}{d} \tag{2}$$

$$u = x_i - x_c \tag{3}$$

$$v = y_i - y_c \tag{4}$$

$$X_O = u\frac{Z_O}{f} \tag{5}$$

$$Y_O = v\frac{Z_O}{f} \tag{6}$$

where f is the focal length of the lens measured in pixels, B is the baseline of the stereo pair in meters, d is the disparity value provide by the stereo processing, x_c and y_c represent the center pixel location of the focal plane array, x_i and y_i are the fire location row and column respectively in the image, and X_O, Y_O, Z_O represent the fire location relative to the left camera frame. The disparity, d, is the mode of the histogram of the disparities associated with the fire object. The 2-D image variables used along with the axis orientation are shown in Figure 2.6.

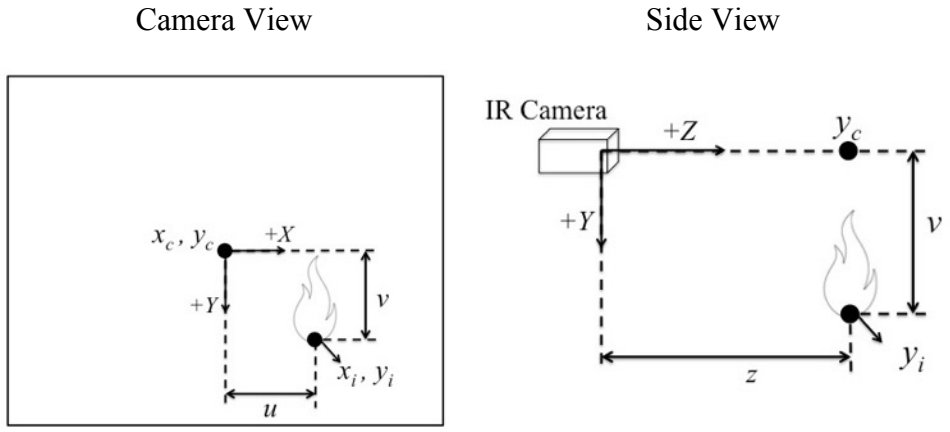

Figure 2.6. Targeted fire coordinates used in converting disparity to depth. (a) 2-D view from the camera of fire (b) side view showing fire relative to IR camera location

The 3D coordinates relative to the camera frame are then transformed to the origin of rotation for the nozzle. Previously a deterministic trajectory model was used to predict the path of the suppressant [26] to provide better initial attack angles but relies on prior knowledge of the pressure

in the water line and the spray pattern as well as experimental data to validate the trajectory model. For the approach described in this paper, the initial attack position is calculated by assuming a linear projection of water from the nozzle to the targeted coordinates. For indoor firefighting operations and closer targets, the linear projection is a reasonable prediction without accounting for spray trajectory. After the yaw and pitch angles are determined the nozzle is adjusted and a solenoid valve is opened automatically to begin suppression. In any system using two cameras in a binocular setup for determining depth, uncertainty exists for the distance of an object. The uncertainty in depth with the IR stereo vision system increases exponentially with distance. For a fire located 3.65 m from the vision system, the uncertainty is 0.43 m in either direction. The error in either direction will cause an over or under-estimation in the initial pitch angle of the nozzle using the linear assumption but is not significant enough to affect the system performance.

2.3.4 Fire Feedback Control

Many current autonomous firefighting systems use large spray patterns that can effectively cover the entire base of a detected fire given a general direction. These systems are mounted at the top of open spaces such as warehouses for early fire protection. For indoor firefighting operations, a more localized approach can be used to reduce water usage and water damage that would occur with total flooding type systems. A feedback control algorithm was developed to use changes in the fire size and targeted position to accurately aim the nozzle. If there is an error between the center base of the fire and the initial nozzle attack angle, only a portion of the fire may be suppressed. The feedback control provides information on how to manipulate the nozzle to fully suppress the fire by stepping in the direction of the remaining portions of the fire still burning. Many current systems use large sweep angles to fully cover a detected fire but if the sweep angle does not fully cover the fire the fire can propagate resulting in longer suppression times. Other systems also use cameras mounted above the nozzle whereas the system presented moves the nozzle independent of the vision system given its application for a robotic firefighter operating on the ground where a fire nozzle will be grasped and manipulated in the right hand or left hand.

The feedback loop for adjusting the nozzle with visual servoing is shown in the decision tree, Figure 2.7. The decision process was formed using a heuristic approach during prior suppression tests. When the system has been alerted and identified the fire in the FOV, the initial number of

pixels associated with the fire is used as the initial fire size. The real approximate width of the fire was calculated using the distance provided by stereo vision along with the fire width in pixels and trigonometric functions.

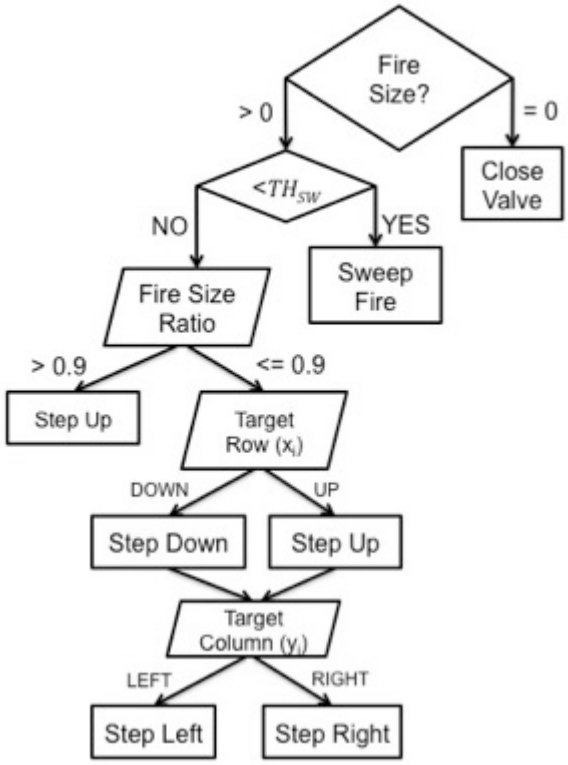

Figure 2.7. Decision tree used in feedback control for nozzle adjustments

The first decision is based on the fire size from the most recently acquired IR image. If there are no more remaining “fire pixels”, the valve is closed and the system can be used to monitor the area for possible flare-ups. If a fire is still detected, then the nozzle needs to be adjusted. Through experimentation, a sweep threshold value 10% of the initial fire size was used. This threshold indicates most of the fire has been suppressed and the nozzle is yawed back-and-forth based on an estimate of the fire width to fully suppress the fire.

If the fire size remains above the nozzle sweep threshold (10% of the initial fire size) then a fire size ratio is used to determine how to properly adjust the nozzle position. Fire size ratio compares the fire size in the current IR image frame to the initial fire size taken. Both values use

the number of pixels as segmented as the sizing variable. The fire size ratio is used to make a decision of how to position the nozzle at the next step and has two possible approaches.

If the fire size ratio is above 0.9 this indicates that the suppressant has not reached the fire to significantly reduce the size. With the linear assumption of the trajectory in place, it is a reasonable assumption that the fire is being under-sprayed and the nozzle is pitched upward 0.5°. This step size results in less than a 5 cm change in direction for an object at more than 4 meters away.

A fire size ratio below 0.9 indicates that the fire has been reduced significantly enough that the nozzle is then adjusted according to how the fire target changes during suppression. The calculated target row is used to adjust the tilt angle of the nozzle and the target column is used to adjust the nozzle yaw angle. The nozzle is moved in 0.5° steps in the direction the target moves from frame to frame. So if the fire target moves from the left to right in two frames the nozzle is moved from left to right one step. This process continues until the fire size falls below the sweep threshold and eventually no longer detected and the water valve closed. For propagating fires, visual servoing will function to adjust the nozzle based on changes in the fire target location. If the initial base position of the fire has been suppressed but the top of the fire is now burning, an adjustment will be made to increase the pitch angle to reach the top portion. This technique is similar to tracking systems that will move a pan-tilt mechanism to keep a target centered in an image.

2.4 Experiments

The autonomous suppression system was evaluated in a large-scale test facility in clear and low visibility fire smoke conditions. Tests in clear conditions were used to examine the effectiveness and response of the system with varying fire locations and compared to results from low visibility tests.

2.4.1 Experimental Setup

The experimental setup consists of wood crib fires placed at varying positions and heights within the field of view of the suppression system, Figure 2.8. Wood crib fires were placed at distances ranging from 2 m to 4 m and at varying heights above and below the camera plane. The

same size wood cribs were used to show repeatability of the system. The wood crib consisted of 24 sticks, measuring 50 mm in diameter, arranged in 6 layers of 4 sticks. The overall dimensions of the array were 300 mm × 300 m × 200 mm. The wood cribs were ignited using a liquid fuel source placed underneath and were allowed to fully develop before suppression. This setup was used in clear condition tests with the autonomous system as well as in clear condition tests with a forced offset introduced into the system to show the robustness of the approach to a poor initial guess or external disturbances such as air currents.

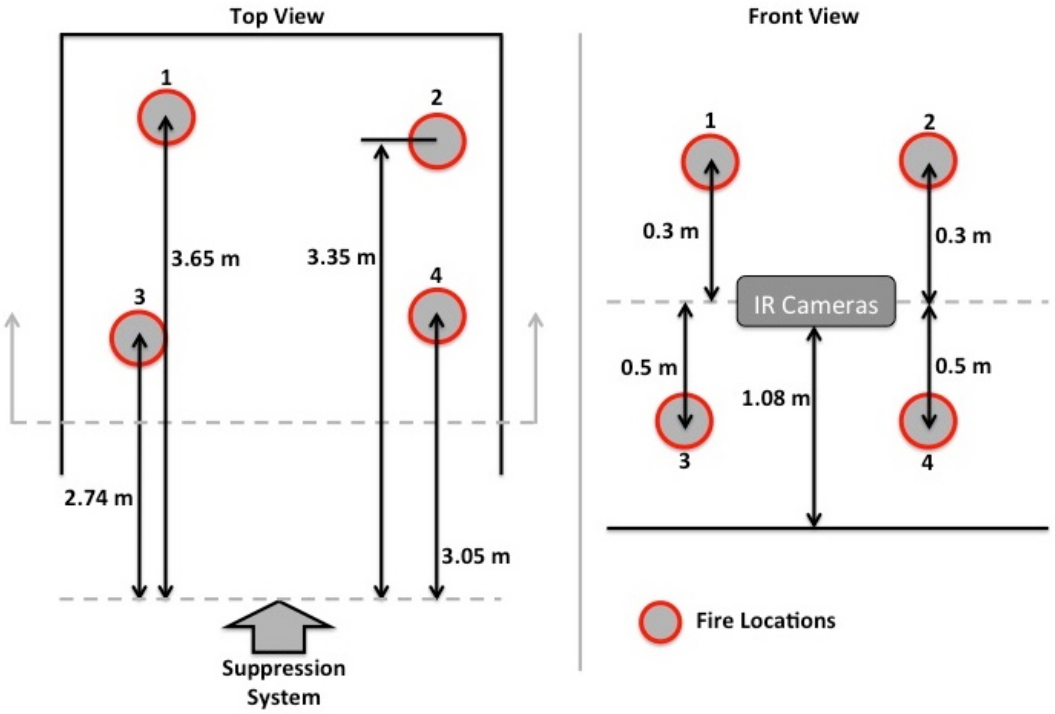

Figure 2.8. Clear conditions experimental setup showing fire locations relative to the IR cameras in a) top view b) front view

A large-scale test facility, Figure 2.9, was used to evaluate system performance in low visibility fire smoke conditions. The test facility consisted of a 6.1 m long, 2.1 m high hallway with an adjoining room on the end. To produce low visibility conditions, a latex foam block, 150 mm × 150 mm × 150 mm, was burned in the adjacent room at the end of the hallway along with the wood crib fire located at the end of the hallway. A blockage was placed at the opening of the hallway under an exhaust hood. This produced an approximately 1.2 m deep smoke layer within the test area. The smoke produced as a result of burning latex foam was dark, thick and low

temperature. The visibility through the smoke was measured during the test by two laser extinction systems located 0.9 m below the ceiling. The sensor suite containing the IR cameras, visual camera and UV sensor were elevated 1.08 m so they were immersed within the developed smoke layer. The wood cribs were elevated to 1.02 m at the end of the hallway to be within the smoke layer. The nozzle was 0.76 m off the ground and below the sensor suite as it would be in a robotic firefighter. The system was placed inside the 1.5 m wide hallway at a distance of 5.5 meters from the fire.

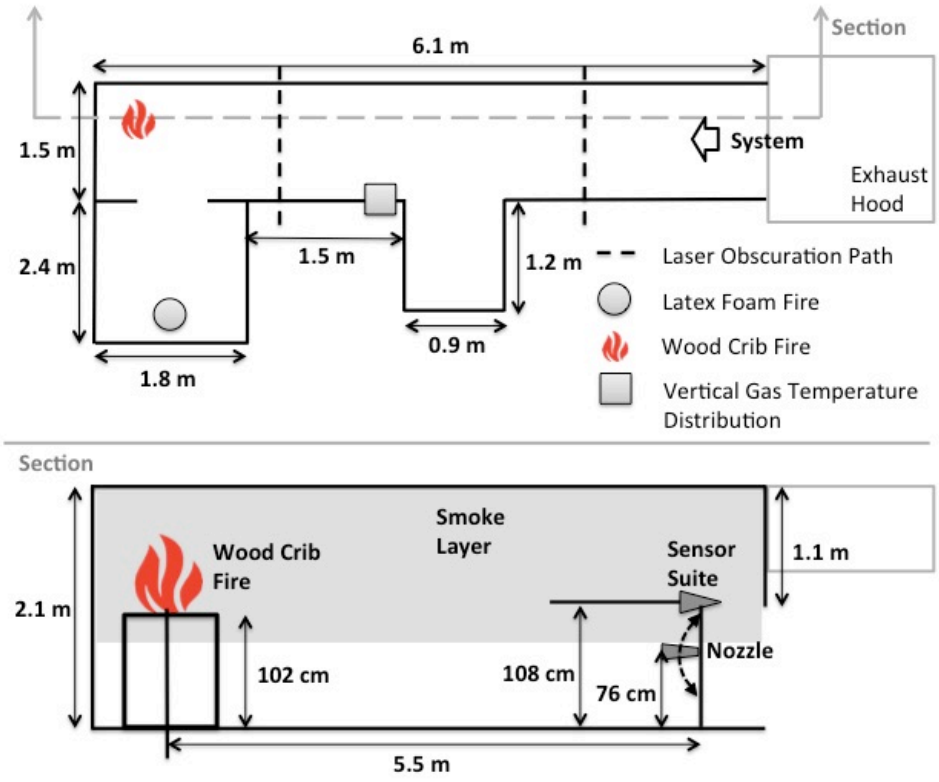

Figure 2.9. Low visibility environment test setup and system

2.4.2 Experimental Scenarios

A total of 44 suppression tests were performed in the study to evaluate the performance of the autonomous system in clear conditions, low visibility smoke conditions, and with a target offset to demonstrate the robustness of the control approach. Sixteen (16) tests were performed in the clear conditions shown in Figure 2.10(a). The environment for 12 of the suppression tests in low visibility conditions are shown in Figure 2.10(b) and Figure 2.10(c). This included manual

suppression tests in low visibility conditions to compare results against the autonomous system. Figure 2.10(b) shows the IR camera pair looking forward to a wood crib fire that is fully developed before the smoke layer has dropped below the sightline of the cameras in the test hallway. Figure 2.10(c) includes a view of the smoke in the hallway with increased development of the smoke layer resulting in visibilities less than 1 m, blocking view of the wood crib fire using traditional RGB cameras. 8 additional tests were performed with the forced offset in clear conditions as shown in Figure 2.10(a) and 8 tests with the forces offset in low visibility conditions, Figure 2.10(c).

(a) (b) (c)

Figure 2.10. Test conditions (a) Forward facing system in clear conditions (b) Wood crib fire before smoke layer development (c) Smoke layer developed in hallway, obstructing view of visual camera

Manual suppression tests were conducted by moving the nozzle while looking at the IR image of the screen to aim the water stream at the fire. Firefighters often make use of thermal imaging cameras (TICs) when fighting fires so the human was given an IR image of the fire scene without any of the target information or image segmentation performed to better highlight the fire. The person uses the raw IR image of the environment to assist in suppressing the fire similar to what might be done using a handheld thermal imager. The valve is opened and the spray is directed based on the IR video being streamed. When the fire is perceived to be fully suppressed the user closes the firefighting nozzle.

A scenario performed to evaluate the robustness of the system consisted of erroneous target information being provided during the fire localization process. This was to simulate possible wind effects on the spray if used outdoors or targeting errors that can result in the system obtaining a

target location not associated with the center base of the fire. The target offsets used were 0.9 m and applied during the fire localization process to alter the initial attack angle of the nozzle. The control algorithm was then evaluated to determine if overall suppression times increase and to test for possible logic errors in the tracking control scheme where the fire was not suppressed.

2.4.3 Experimental Procedure

Each experiment with the autonomous system followed the same test procedure. The test was initiated by igniting a liquid fuel source beneath a wood crib fire. Once the fuel source had burned off and the wood crib had become fully developed in approximately 3 minutes, the system started the suppression process. There was no time recorded for fire growth since the system initiated suppression with a fully developed wood crib fire in the field of view. The algorithm detected the fire, positioned the nozzle and automatically opened a solenoid valve upon detection in under 0.2 seconds. The image feedback control algorithm tracked the fire size and continued spraying until the system was alerted to shut the water off, when the UV and IR sensors no longer detected a fire. Additional data was collected for 2 minutes and the system continued to monitor the area in case of flare-ups. If this occurred, the suppression algorithm starts from the beginning, indicating a fire is present. All suppression times presented include two standard deviations above and below the mean to show the range of suppression times in each scenario.

2.5 Results

2.5.1 High Visibility Results

The measured suppression times and target information for 16 wood crib suppression tests are provided in Table 2.1. Fires were placed at four different locations and four tests were conducted for each position. The 3D coordinates of the fire were calculated with IR stereo vision. Z is the distance from the camera plane to where the fire is located and Y is elevation with negative values indicating the target is above the camera plane and positive values indicating the target is below the system. Negative X-coordinates indicate the fire is to the left of the camera plane and positive values for fire targets to the right. Four different times were recorded for suppression. Spray time is the total time the water was being applied from the valve opening to closing. UV and IR times are the times a fire was detected in the scene from the

beginning of suppression until each sensor no longer detected the fire in the scene and sent back a zero signal indicating the fire is out. For this, the UV sensor no longer generated pulses and the IR cameras no longer detected "fire pixels" as determined by the targeting algorithm, which uses an intensity or temperature threshold. Human perception was taken from the visual recording from behind the nozzle during testing.

Table 2.1. System suppression times for clear condition test environment, single wood crib fire

Relative Location	Fire Coordinates				Suppression Times			
	#	Z [m]	X [m]	Y [m]	UV [s]	IR [s]	Operator Observed [s]	Average Time [s]
Above-Left	1	3.65	-0.90	-0.30	3.25	3.40	3.50	3.38
	2	3.65	-0.90	-0.30	4.75	4.80	5.25	4.93
	3	3.65	-0.90	-0.30	4.50	4.80	4.75	4.68
	4	3.65	-0.90	-0.30	4.00	4.20	4.50	4.23
					Location 1 Average Suppression Time [s]:			4.31 ± 1.36
Above-Right	5	3.35	1.10	-0.30	2.75	3.00	3.25	3.00
	6	3.35	1.10	-0.30	4.25	4.20	5.25	4.57
	7	3.35	1.10	-0.30	2.00	2.00	3.00	2.33
	8	3.35	1.10	-0.30	2.50	2.60	3.25	2.78
					Location 2 Average Suppression Time [s]:			3.17 ± 1.95
Below-Left	9	2.74	-1.20	0.50	3.25	3.40	4.25	3.63
	10	2.74	-1.20	0.50	3.75	3.80	5.25	4.27
	11	2.74	-1.20	0.50	3.25	3.40	4.75	3.80
	12	2.74	-1.20	0.50	2.50	2.60	3.25	2.78
					Location 3 Average Suppression Time [s]:			3.62 ± 1.24
Below-Right	13	3.05	0.90	0.50	4.00	4.20	5.00	4.40
	14	3.05	0.90	0.50	3.50	3.60	3.75	3.62
	15	3.05	0.90	0.50	3.00	3.20	4.00	3.40
	16	3.05	0.90	0.50	3.25	3.40	4.50	3.72
					Location 4 Average Suppression Time [s]:			3.79 ± 0.86
					Total Average Time to Suppression [s]:			3.72 ± 1.51

In Figure 2.11(a) is a fully developed wood crib fire ready to be targeted. The system accurately sprays the base of the fire, Figure 2.11(b), and closes the valve once the fire is no longer detected, Figure 2.11(c).

(a) (b) (c)

Figure 2.11. Fire suppression test shown a) before, b) during, and c) after the fire is fully suppressed

An additional view of the suppression process is shown in Figure 2.12 with detailed progression of visual servoing feedback control. As the fire becomes fully developed, Figure 2.12(a), it is detected and targeted with the IR stereovision. The nozzle moves into position assuming the linear projection from the nozzle to the base and the valve is opened, Figure 2.12(b). The algorithm increases the nozzle pitch, Figure 2.12(c,d), until the fire size decreases below 90% of the original size, Figure 2.12(d). The system then adjusts slightly to the left due to the fire target moving left, Figure 2.12(e). The nozzle then sweeps back and forth, Figure 2.12(f,g), until the fire is no longer detected and the valve closed, Figure 2.12(h).

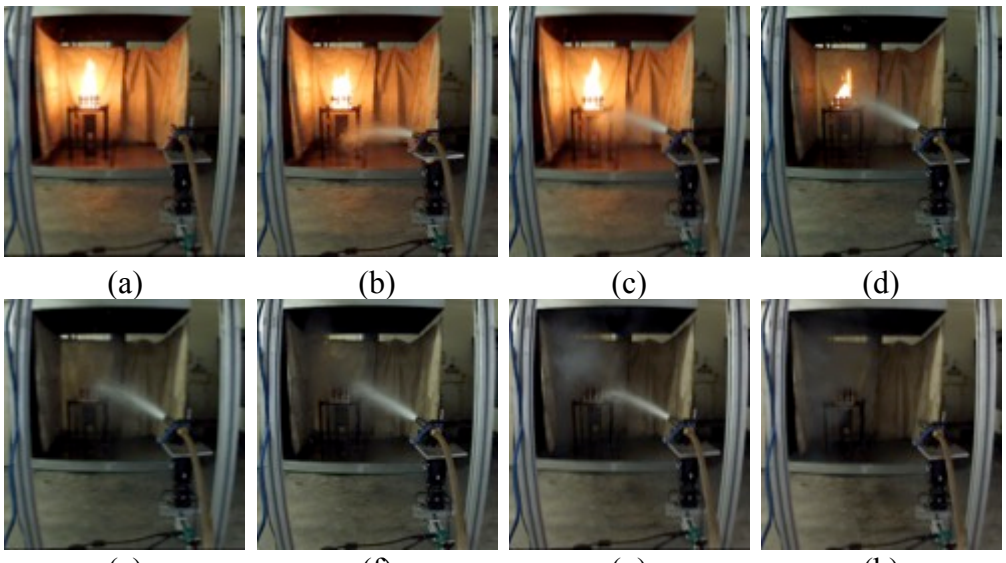

(a) (b) (c) (d)

(e) (f) (g) (h)

Figure 2.12. Fire suppression test before alerted to fully suppressed fire

The average suppression time for the test is an average of the UV, IR, and human perception times. Spray time was not a reasonable determination of suppression because of a delay in the response between the system closing the valve and the spray actually ceasing. Table 1 shows water spray time is longer than the detection time from the UV sensor or IR system for every test. The total average suppression time for 16 tests was 3.72 s ± 1.51 s Suppression times for the single wood crib fire ranged from 2.78 seconds to 4.93 seconds. The system was able to detect and target the base of the fire in every test in under 0.2 s. The only nozzle movements in the tests were an upward pitch to account for the trajectory of the water stream and a small sweeping motion to fully suppress the fire. The valve was closed and spray was stopped when the UV and the IR sensors no longer detected a fire in view.

2.5.2 Low Visibility Results

The same system used in high visibility environment testing was used in the low visibility environments. A laser extinction system (using HeNe lasers operating at 632 nm) was used to monitor the visibility through the smoke at 0.9 m below the ceiling at the location shown in Fig. 9. During low visibility experiments, the visibility dropped below 1.0 m as shown in Figure 2.13(a). The temperature distribution during low visibility testing at the vertical gas temperature distribution location is shown in Figure 2.13(b).

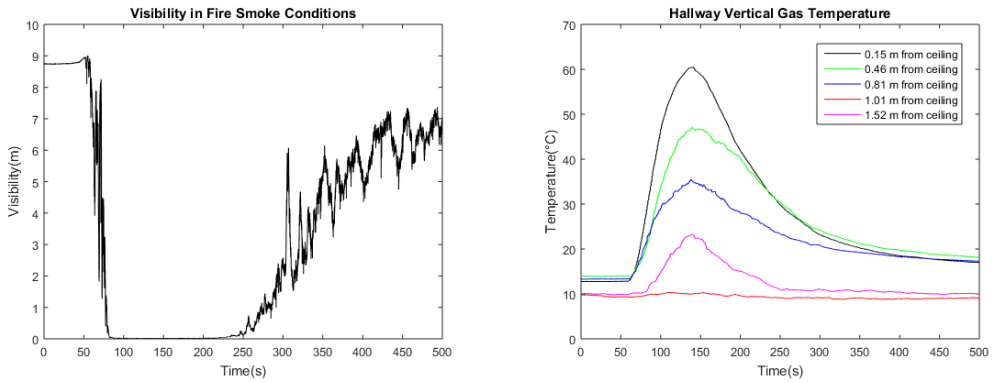

(a) (b)

Figure 2.13. (a) Visibility data from laser obscuration system (b) Vertical gas temperature distribution at wall during low visibility suppression test

Images from three different views of a low visibility test are shown in

Figure 2.14. Fire suppression test in low visibility environment (a) startup of suppression (b) fire knocked down during suppression (c) end of test

. Included are images from the IR with the fire segmented and highlighted red with a green target placed at the target location at the base of the fire. The visual images are taken from the same image plane as IR and show how the smoke obstructs the view of the fire. An additional camera placed behind the system and below the IR and visual cameras was used to capture the nozzle movements and water spray.

Figure 2.14. Fire suppression test in low visibility environment (a) startup of suppression (b) fire knocked down during suppression (c) end of test

(a) is the initial startup of the system when the fire is targeted and water is turned on. Initially the back view camera shows the fire in view but as the water vapor and smoke mix, the smoke layer drops obstructing view of the fire in the visual spectrum. The fire has begun to be suppressed in

Figure 2.14. Fire suppression test in low visibility environment (a) startup of suppression (b) fire knocked down during suppression (c) end of test

(b) and is fully suppressed in

Figure 2.14. Fire suppression test in low visibility environment (a) startup of suppression (b) fire knocked down during suppression (c) end of test

(c). Using the IR stereo vision, the system autonomously detected, targeted and directed the water spray to successfully suppress a single wood crib fire, despite the degraded conditions

produced due to the suppression process. Manual suppression was also measured within the same test setup.

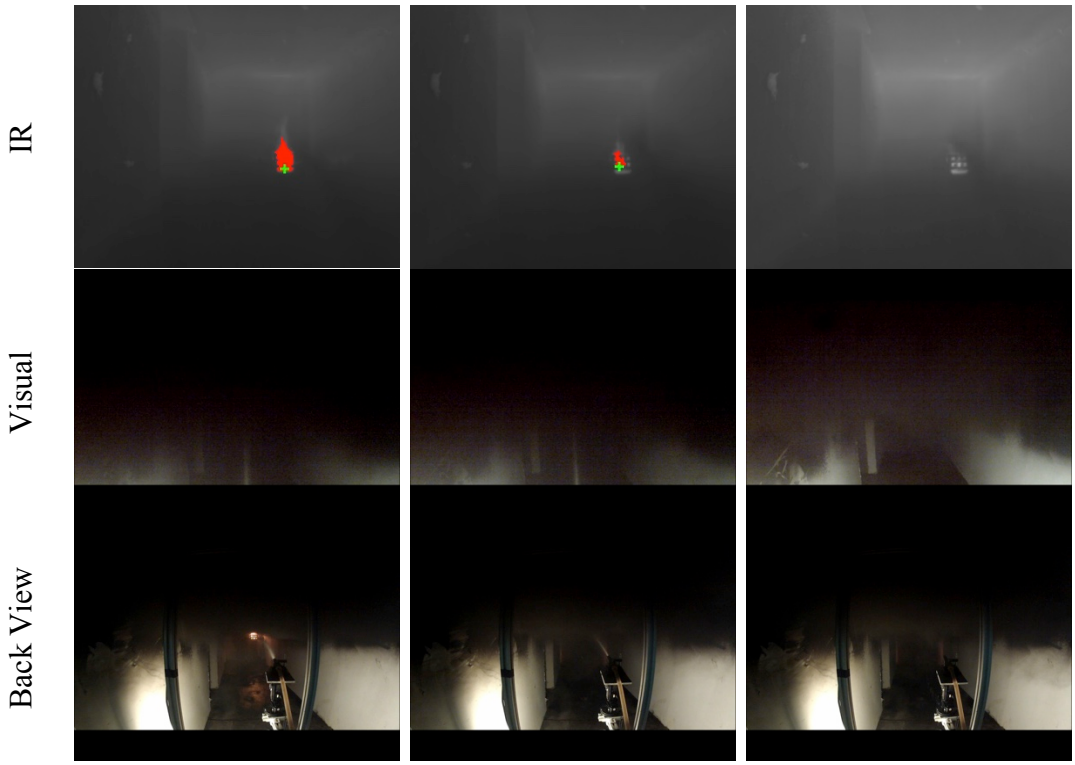

Figure 2.14. Fire suppression test in low visibility environment (a) startup of suppression (b) fire knocked down during suppression (c) end of test

Table 2.2 includes the suppression times and target coordinate information for low visibility tests done with the autonomous system and manual suppression. The system was able to suppress the wood crib fire in 4.49 s ± 1.62 s in the low visibility testing environment. The suppression times for the autonomous system ranged from 3.4 s to 5.9 s. The control algorithm was able to adjust for the parabolic spray trajectory caused by the increased distance of the fire from the system through an increase in pitch angle. The average time for manual suppression in the same scenario is 14.75 s ± 4.51 s for four wood crib suppression tests. This average time was over 10 seconds longer than with autonomous system performance in the same environment and positioned. The

operator view of the fire and water spray is occluded in the low visibility test environments leading to longer suppression times where the system is able to visualize the fire in the same environment.

Table 2.2. System suppression times for low visibility test environment, autonomous system and manual suppression

Test	Fire Coordinates				Suppression Times			
	#	Z [m]	X [m]	Y [m]	UV [s]	IR [s]	Operator Observed [s]	Average Time [s]
Low-Vis Hallway	17	5.49	0.91	-0.30	3.00	3.00	4.25	3.42
	18	5.49	0.91	-0.30	5.00	5.00	7.75	5.92
	19	5.49	0.91	-0.30	3.25	3.25	4.50	3.67
	20	5.49	0.91	-0.30	4.25	4.25	6.25	4.92
					Location 1 Average Suppression Time [s]:			4.48 ± 2.32
Low-Vis Hallway	21	5.49	-0.91	-0.30	4.50	4.50	6.25	5.08
	22	5.49	-0.91	-0.30	3.75	3.75	5.75	4.42
	23	5.49	-0.91	-0.30	4.00	4.00	5.25	4.42
	24	5.49	-0.91	-0.30	3.50	3.50	5.25	4.08
					Location 2 Average Suppression Time [s]:			4.50 ± 0.84
					Total Average Time to Suppression [s]:			4.49 ± 1.62
Manual Low-Vis Hallway	25	5.49	0.91	-0.30	14.00	14.00	22.00	16.67
	26	5.49	0.91	-0.30	11.00	11.00	18.00	13.33
	27	5.49	0.91	-0.30	10.00	10.00	17.00	12.33
	28	5.49	0.91	-0.30	13.00	13.00	24.00	16.67
					Total Average Time to Suppression [s]:			14.75 ± 4.51

2.5.3 Target Error Effects

To further test the autonomous system forced offsets were introduced into the control algorithm. Once the target coordinates were determined, an offset was applied by adding or subtracting 0.9 m from the X-coordinate of the fire. This forces the nozzle to initially spray towards the left or right of the initial fire target. The nozzle must adjust left or right accordingly to cover the fuel bed. Tests 29-36 were conducted in the high visibility environment while Tests 37-44 were performed with a smoke layer. For high visibility tests, the total average suppression time is 4.11 s ± 0.84 s. For low visibility scenarios, the total suppression time is 4.80 s ± 0.79 s. Table 2.3 contains the suppression times as well as the coordinate information from the system along with the offset distance when the forced offset was applied targeting left or right of the fire. The XYZ-

coordinates in the table are provided by the IR stereo vision and the offset distance is the X-coordinate with a 0.9 m offset added or subtracted from the initial coordinate values.

Table 2.3. System suppression times for forced offset tests in high and low visibility environments

Visibility	Fire Coordinates					Suppression Times			
	Test	Z [m]	X [m]	Y [m]	X with offset [m]	Operator Observed [s]	UV [s]	IR [s]	Average Time [s]
Clear	29	3.65	1.10	-0.30	2.00	5.75	4.25	4.50	4.83
	30	3.65	1.10	-0.30	2.00	5.50	3.00	3.25	3.92
	31	3.65	1.10	-0.30	0.20	5.25	3.00	3.25	3.83
	32	3.65	1.10	-0.30	0.20	5.50	3.25	3.25	4.00
						Location 1 Average Suppression Time [s]:			4.15 ± 0.92
Clear	33	3.65	-1.10	-0.30	-2.00	4.50	3.50	3.75	3.92
	34	3.65	-1.10	-0.30	-2.00	4.50	3.50	3.50	3.83
	35	3.65	-1.10	-0.30	-0.20	4.75	3.25	3.50	3.83
	36	3.65	-1.10	-0.30	-0.20	4.00	5.00	5.25	4.75
						Location 2 Average Suppression Time [s]:			4.08 ± 0.89
						Clear Environment Total Time to Suppression [s]:			4.11 ± 0.84
Low	37	5.49	0.91	-0.30	1.80	6.25	4.50	4.50	5.08
	38	5.49	0.91	-0.30	1.80	5.50	4.25	4.75	4.83
	39	5.49	0.91	-0.30	0.00	5.75	4.00	4.50	4.75
	40	5.49	0.91	-0.30	0.00	6.00	3.75	4.25	4.67
						Location 1 Average Suppression Time [s]:			4.83 ± 0.35
Low	41	5.49	-0.91	-0.30	-1.80	5.50	3.75	4.25	4.50
	42	5.49	-0.91	-0.30	-1.80	5.25	3.50	4.00	4.25
	43	5.49	-0.91	-0.30	0.00	6.00	4.00	4.25	4.75
	44	5.49	-0.91	-0.30	0.00	6.25	5.00	5.50	5.58
						Location 2 Average Suppression Time [s]:			4.77 ± 1.15
						Low Visibility Environment Total Time to Suppression [s]:			4.80 ± 0.79
						Total Suppression Time with Forced Offset Positioning [s]:			4.45 ± 1.06

Another scenario for testing the system included two wood-crib fires placed adjacently. The overall dimensions of the array were 600 mm × 300 m × 200 mm. The center of the total fire base was used as the initial target location. Figure 15 includes images from the visual camera and the IR with the fire displayed as the red object. In Figure 2.15(b), the base of the entire wood-crib fire is knocked down but the spray is angled toward the left side of the fire resulting in the right side to continue burning. Due to the aiming target moving toward the right, the nozzle is correctly adjusted in that direction to continue suppression. A total of 4 tests were performed with the wider wood-crib fires and the suppression times are included in Table 4. For these tests, the total average suppression time is 6.65 s ± 0.90 s.

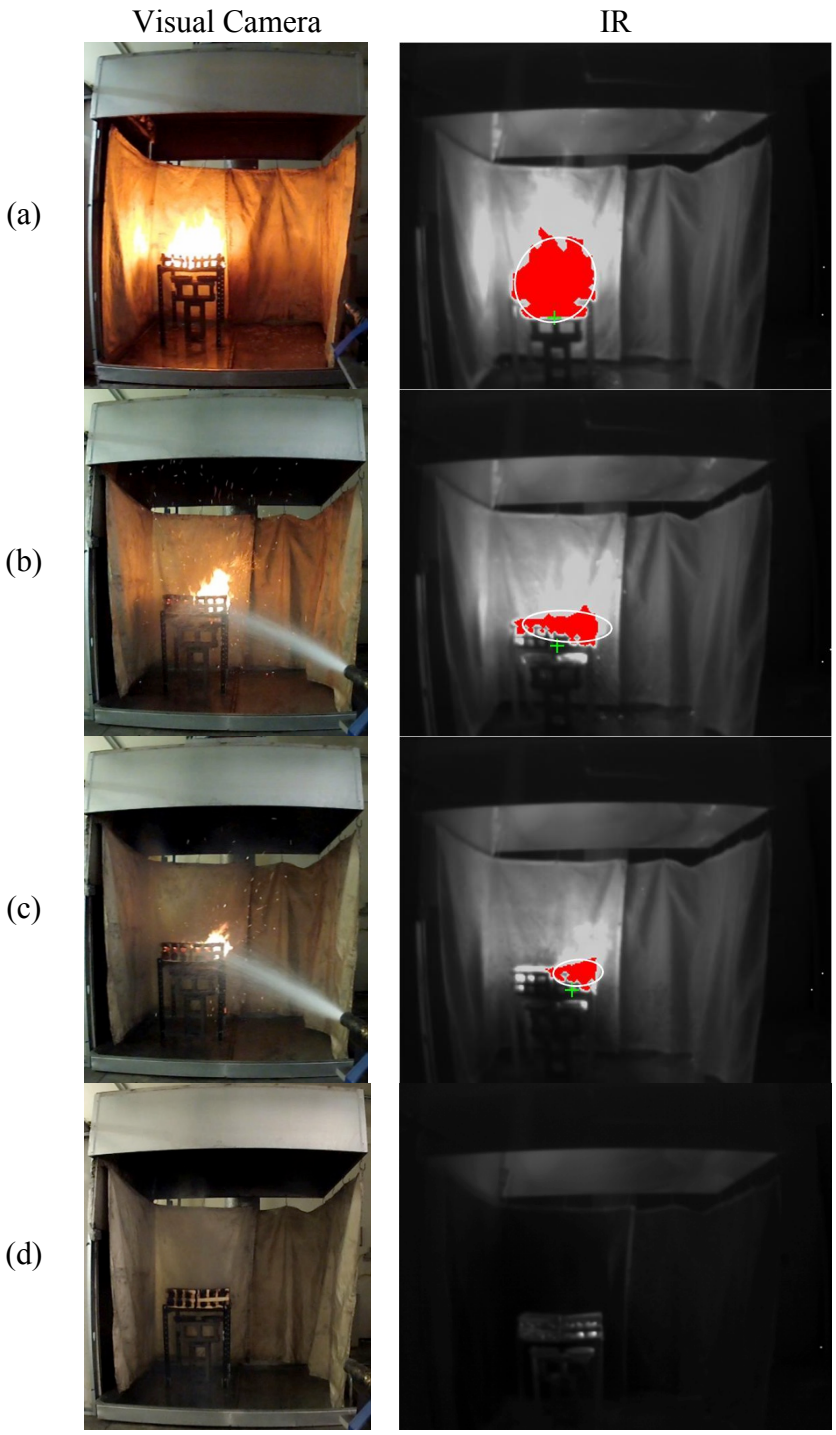

Figure 2.15. Fire suppression test with two wood crib fires a) startup of suppression b) left side of fire knocked down during suppression c) left side of fire suppressed d) end of test.

Table 2.4. System suppression times for wide fires in high visibility environments

Relative Location	Fire Coordinates				Suppression Times			
	#	Z [m]	X [m]	Y [m]	UV [s]	IR [s]	Operator Observed [s]	Average Time [s]
Above-Left	1	3.65	-1.10	-0.30	5.75	6.00	6.25	6.00
	2	3.65	-1.10	-0.30	6.75	7.20	7.00	6.98
	3	3.65	-1.10	-0.30	6.50	7.00	7.25	6.92
	4	3.65	-1.10	-0.30	6.00	6.80	7.25	6.68
							Total Average Time to Suppression [s]:	6.65 ± 0.9

2.6 Discussion

Results from tests with clear environments demonstrate the effectiveness and response of the autonomous fire suppression system. The fire was immediately detected with the UV and IR sensors upon activation of the system after the wood crib fire was fully developed. The system was able to effectively suppress the fire based on feedback from the IR cameras showing how much of the fire is suppressed at each IR image captured.

The linear assumption of the spray was a reasonable estimation of the spray trajectory for close proximity firefighting. A model of the trajectory [56-57] can be used to deterministically predict the correct pitch angle to reach the target and uses pressure, flow rate, droplet diameter, and spray breakup characteristics. For the fire locations from the spray nozzle and pressure of the system, the spray often had a slight parabolic trajectory resulting in the spray being just below the fire target estimated with the IR stereo vision. The system accounts for this occurrence by pitching the nozzle up if the fire size does not decrease sufficiently (<90% of the initial size).

Figure 2.16 shows 3 fire targets at 2.5, 4.0, and 7.0 m from the system located 0.76 m above the ground. The linear assumption is used to calculate a pitch angle from the nozzle to the base of the fire. The trajectory is that of the system used with known pressure, flow rate, and the calculated tilt angle. The linear assumption becomes less effective as the distance to the fire increases due to droplet breakup behavior and the fire is under-sprayed. For fires less than 4.0 m from the system the linear assumption is effective. As distances increase, different approaches to modeling the spray will be needed to account for the parabolic shape.

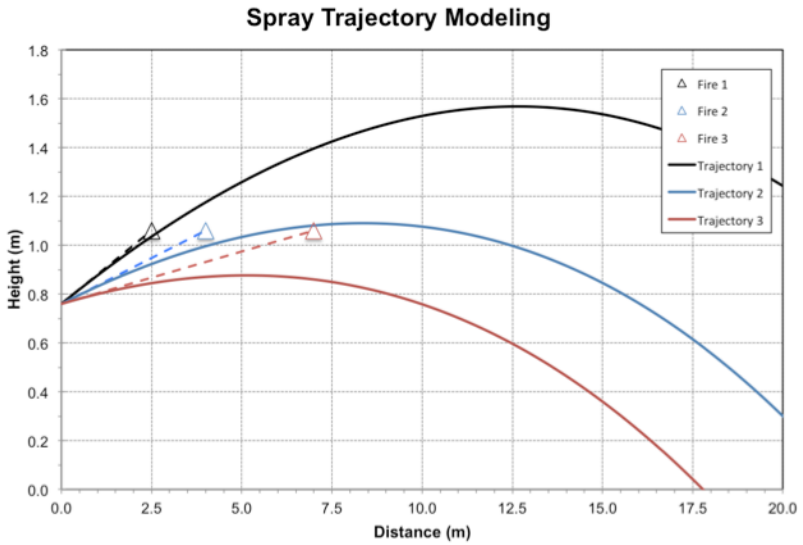

Figure 2.16. Water spray trajectory at calculated targeted tilt angles given linear assumption

Suppression times from low visibility tests in the hallway setup were 0.77 seconds longer than those in the clear environment. The increase in time was most likely due to the increase in pitch correction with the fire being further away from the nozzle. Despite the dense smoke and steam generated during the suppression process, the system is still able to accurately segment the fire from the thermal images and determine an accurate fire location relative to the nozzle origin. The performance in low visibility environments in the fire feedback control process was similar to that in clear conditions and was an improvement over manual suppression tests. It is difficult for firefighters to judge the distance of the fire given a 2-D image or when the fire has been fully suppressed due to smoke and water vapor buildup. As a result, manual suppression required 10 seconds longer of spray time to put out the fire.

The tests with forced offsets were conducted to simulate possible effects from wind if the system was outdoors or errors in targeting that force the initial estimate of the fire location to be left or right of the real physical coordinates. The system was able to suppress a single wood crib fire in an average of 4.11 s in high visibility, 0.39 s longer than the system with no forced offsets. In low visibility, the system had an average suppression time of 4.80 s, 1.08 s longer than with no forced offset. This showed the capability of the system to adjust for errors by tracking the fire target and fire size continuously using a decision tree with feedback control to provide directions for visual servoing of the nozzle. If only a portion of the crib was sprayed, the feedback corrected the nozzle to accurately target the other portions of the fire. In tests performed with wider fires,

the system initially sprayed one side and adjusted horizontally based on the target shifting. Overall, it was shown that an indoor autonomous suppression system is feasible for localized suppression of fires and can be implemented onto a robotic firefighter that will have to suppress fires in clear environments, low visibility environments, and offsets that simulate wind or other air currents.

Future work will use a probabilistic fire classification method that has been developed [55] for use in fire detection. Hot spots and fire reflections in the environment can be classified and ignored for the purposes of only targeting the fire detected in the FOV or for other fire tactics such as cooling hot areas in the compartment. This method can also provide multiple fires to be classified simultaneously and allow the system to determine which fire to initially target based on distance or fire size. The classification method also functions to provide the robot a heading angle to navigate towards a fire given the presence of smoke or smoke reflections in the surroundings. Other possible approaches for navigation are the use of fire detectors in individual compartments for early detection and the robot being provided with preprocessed maps of a designated area. Once the robot has navigated toward the fire compartment and the fire is in view, the suppression algorithm is used to fully suppress the fire using the visual servoing technique presented in this paper.

2.7 Conclusion

An autonomous fire suppression system including a multispectral sensor suite was developed and demonstrated to suppress wood crib fires in indoor environments with clear and low visibility environments. The fire was detected by the UV and IR sensors, targeted through a segmentation process, localized through use of IR stereo vision, and suppressed through visual servoing with feedback control through a nozzle mounted on a yaw-pitch mechanism for manipulation. The system uses a decision tree model for feedback control over the nozzle movements to adjust where the suppressant is applied.

Tests were performed in a large-scale test facility in both clear and low visibility conditions. The system was able to suppress a 40-50 kW wood crib fire in a total average time of 3.72 s in clear conditions. The system average suppression time in low visibility environments was 4.49 s. The same test scenario with manual suppression of the fire only using the raw thermal images of the scene was 14.75 s. To simulate the effects of wind, a forced offset was

applied to the initial fire target coordinates to initially position nozzle off-center of the fire. In the clear environment, the average suppression time was 4.11 s while in low visibility the time was 4.80 s. The system was able to effectively adjust the nozzle to fully suppress the fires based on IR feedback of the fire size and position. Overall, it was shown that an autonomous suppression system is feasible for localized suppression of fires and can be applied to a robotic firefighter for indoor firefighting operations.

3 Probabilistic Classification of Water Spray and Leaks using Infrared Cameras

3.1 Abstract

A probabilistic classification technique was developed for identifying water leaks and sprays in infrared (IR) images. Water classification can be used on a robot for indoor firefighting operations and inspection tasks or with a fixed autonomous fire suppression system. The method was designed for use in an autonomous fire suppression system that identifies fire and water spray within a 2D image and is able to adjust the spray direction based on feedback between the two objects. IR cameras were used due to the fact that long wavelength infrared can image through low visibility environments encountered in indoor fire suppression activities. The performance of visible cameras in such scenes is subpar due to smoke and particulate obstructing view of the surroundings. In outdoor and clear conditions, the varying appearance of water due to environmental conditions such as wind, lighting, and background clutter make water classification difficult. Motion characteristics were used to segment potential water objects in a scene and first and second-order statistical features were extracted to distinguish water objects from other candidate regions with high motion characteristics. The algorithm used four distinct texture features identified through a Bayesian classification method to characterize and classify the candidates. Based on classification of candidates from large-scale test data with varying water temperatures, visibility conditions, and spray patterns, the classification performance error was measured to be 16.4% based on validation using the test dataset. The precision, recall, F-Measure, and G-Measure were 86.1 – 97.4% for classifying water and non-water candidates using the test dataset.

3.2 Introduction

To limit the exposure and risk of firefighters and to improve effectiveness of indoor firefighting operations, robots have been proposed as a support tool. One aspect of robotic firefighting is a fire suppression system that autonomously detects and extinguishes fires effectively and efficiently. Many versions of firefighting robots [10, 17, 27-30] have been developed; however, most use an operator to remotely control them or have not been tested in realistic fire scenarios. In the shipboard autonomous firefighting robot (SAFFiR) program, a

humanoid robot was developed to autonomously locate and suppress fires located onboard naval ships in indoor structures. Advancements including artificial intelligent algorithms and perception systems [21-25] along with autonomous fire suppression approaches [26] were developed through the program to further advance firefighting robots. In addition, a probabilistic classification technique was proposed to distinguish fire and smoke from reflections or hot objects [55] for use in determining a heading direction for the robot to locate a fire. Due to the smoke-filled environments that are encountered in firefighting, IR cameras were selected over visual RGB cameras. Handheld thermal infrared cameras (TIC) are typically used to aid in firefighting tasks within smoke-filled environment [39-42]. For TICs and IR cameras that absorb IR radiation in the long wavelength IR (LWIR, 7-14 micron range), they are able to image surfaces even in dense smoke and zero visibility environments [24]. Classification of objects with thermal imagers is needed to provide the robotic system with the information required to efficiently perform firefighting tasks even in clear and low visibility environments.

Water is an unstructured, moving object that makes its segmentation and classification complex. There are many different approaches to segmenting and classifying moving objects in video sequences but active water segmentation with classification techniques in IR have not been widely studied. Some spray segmentation approaches include edge detection [58-59], which relies on high contrast between warm temperature diesel spray and a static blank background. Water spray or leaks in IR images contain a high level of noise and can be very low contrast making traditional edge-based detection algorithms unreliable [60]. Water does not have a distinct structure so classification techniques relying on shape cannot be used in low contrast scenarios. Image segmentation based on Otsu's method, a cluster-based image thresholding technique, has been used when the object or spray has high contrast with the background [61-63] and can be separated as foreground. In the suppression system, the water object is often low intensity (low temperature) and merges with parts of the background. Background subtraction techniques such as Gaussian Mixture Models (GMM) [64] and adaptive background subtraction are unreliable in IR video due to the low signal-to-noise ratio [65]. A reliable background model cannot be used in dynamic firefighting scenes involving fire, water, smoke, and reflections due to the large differences between an image and a background model that are produced as the scene changes or the system moves due to robot motion or from scanning the area.

One area of research for water detection is in obstacle avoidance for unmanned ground vehicles. Passive sensors (visible, short-wave IR, thermal infrared, polarization [66-71]) and active sensors (lasers [72-73]) have been explored for use in water detection. Due to many external factors including color of the sky, time of day, wind, terrain reflections, surface vegetation, and shadows, the appearance of water can vary greatly and a single cue for water is unreliable. Spatio-temporal variations are useful in moving water detection but not for water that is still [74]. While some RGB models have been introduced for use in water detection [75] they are not applicable in firefighting scenarios due to low visibility and dark environments. More recent models introduced the dynamic nature of water as an addition to segmenting water from RGB videos [76, 78]. They use optical flow vectors and spatial descriptors to illustrate the ripple effect of water waves but the method was not demonstrated in a real-time system. A similar multi-feature approach is applicable to water classification in IR but optical flow in dynamic scenes is difficult to implement as a feature vector for water classification in IR due to noisy images and fire and smoke in the scene. The use of the periodic frequency of water ripples is not applicable to sprays and droplets for a firefighting system. It is proposed that motion characteristics be used to determine areas within the IR image that have a high rate of change between consecutive images, which can then be further filtered and classified using supervised machine learning to segment water from a scene. Since the vision system onboard a robot may contain slight motion of the cameras due to the robot dynamics and high varying environments in IR, faster motion detection techniques are used for extracting candidate regions [79].

This chapter presents a probabilistic classification method for water spray and leaks and non-water objects. The method uses images from a single IR camera to acquire textural features of high-motion regions calculated with a three-frame differencing approach. Bayes' theorem was used to compute the posterior probabilities of water and non-water objects, which can be used in leak inspections and in determining the water location for use in an autonomous fire suppression system. A Bayesian classifier was trained using a variety of large-scale training data with varying water temperatures, spray patterns, environmental conditions, and dynamic backgrounds. The algorithm was then tested using a separate series of tests to validate the ability of the method to accurately distinguish water from other non-water high-motion objects in the same scene and apply a probability representing a level of confidence in the classification.

3.3 System Description

Water and other objects (e.g., reflections, moving objects, background) are probabilistically classified to provide information to determine where in an IR image water is located for use in fire suppression systems and for inspection tasks. Images were captured using a FLIR A35 long wavelength (7-14 μm) IR camera with a 320×256-pixel focal plane array, and 60 Hz frame rate. The camera produces 14-bit resolution images with intensity values ranging from -16384 for -40℃ to -1 for 160℃. The FLIR A35 camera was used since it is lightweight and can be used on a robotic platform as well as the ability to image in clear to zero visibility fire smoke conditions. For collecting the training and test datasets, the IR camera was mounted above a spray nozzle. The nozzle was manipulated using a yaw-pitch servo motor system.

Figure 3.1 contains a diagram of the proposed method for extraction of candidate regions through the pre-processing and classification stages. The regions highlighted in blue in the IR images denote segmented candidate regions. Candidates were extracted using a three-frame differencing method with adaptive intensity and motion thresholding and morphological filtering. A red ellipse outlines each candidate ROI and if the object has been classified as water, the probability is displayed in yellow text on the image object. Objects not classified as water are not labeled in the display. Without proper classification of the extracted candidates, an erroneous water region may be used within the suppression algorithm leading to an error in directing the water spray towards the targeted fire location. A Bayesian classification method was implemented to probabilistically classify water from other high motion objects by analyzing multiple texture features extracted from the candidate regions through use of a Gray Level Co-Occurrence Matrix (GLCM). Analysis was performed to select the optimal combination of features resulting in the lowest error percentage in classifying water objects.

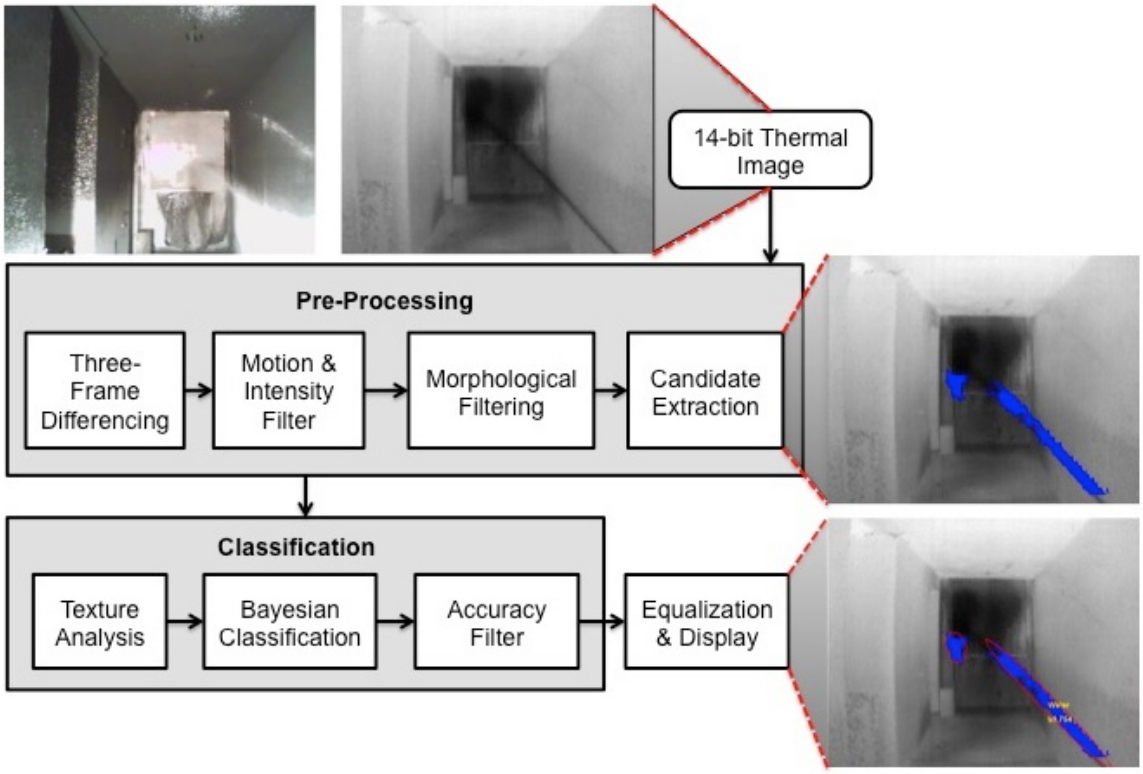

Figure 3.1. Block diagram of proposed system with IR images after pre-processing and display

3.4 Pre-Processing

3.4.1 Motion Segmentation

Image segmentation is the process of partitioning an image domain into several disjointed subregions such that each region directly corresponds to a single object. Given an image I: $\Omega \rightarrow R$, where $\Omega \subset R^D$ is a closed, bounded region that represents the domain of I, segmentation aims to partition the domain Ω into several regions that delineate an image pattern from other regions. The problem of image segmentation has been challenging and fundamental in the area of computer vision with a wide range of applications. The approaches are classified into edge-based models and region-based models. Edge-based models rely on distinct edge information being able to provide the boundaries of regions. Region based models partition the image into regions that contain distinct statistical properties from other regions.

There are a number of motion-based background subtraction methods as well, that are used to detect the foreground of a scene or motion within an image. These techniques are not compatible with this research given the use of IR and the image properties of water in varying environments. Color information is not useful due to changing lighting conditions, brightness of the environment, or obstruction of the scene due to low visibility conditions caused by firefighting operations indoors. The scene will continually change due to possible robot motion, fire and fire reflections in the scene, and the low signal-to-noise ratio of IR continually changing a pixel intensity value. Figure 3.2 includes an IR image of water spray with a fire in view. Due to the high intensity values associated with the fire, the image when converted to grayscale masks the water location with the background making many conventional motion segmentation techniques (e.g. Otsu's method) or edge-based segmentation methods fail. Due to the need for a real-time processing technique, processing cannot be performed on a large number of image frames for improved segmentation performance.

Figure 3.2. IR and visual images of outdoor water spray with wood-crib fire.

Motion detection through the use of frame differencing is very sensitive to the threshold value applied to segment the scene into foreground and background but can operate in real-time processing algorithms. Frame differencing is a non-recursive technique in that it does not depend on the history beyond a few frames stored in a buffer and is highly adaptive. The high frame rate of the IR cameras used (60 Hz) makes frame-differencing a reasonable approach to motion segmentation. A three-frame differencing approach is used to further eliminate regions that may have a large difference between only two frames and makes use of the dynamics of a water spray with high rates of change at the edges of the spray and internal to the spray. A larger amount of

frames (>5) will result in more ROIs due to larger pixel intensity changes between more consecutive frames. Since water does not appear as a solid object, pixel intensity values of the droplets breakup behavior is highlighted between image frames. IR images of a water spray were collected using a stationary system in an outdoor environment at 20 frames per second. Ten pixel locations in the image set are denoted in Figure 3.3 including 5 pixels along the spray trajectory, 2 pixels at the back end of the spray, and 3 pixels in background regions. The intensity values of these points as a function of time are plotted in Figure 3.4.

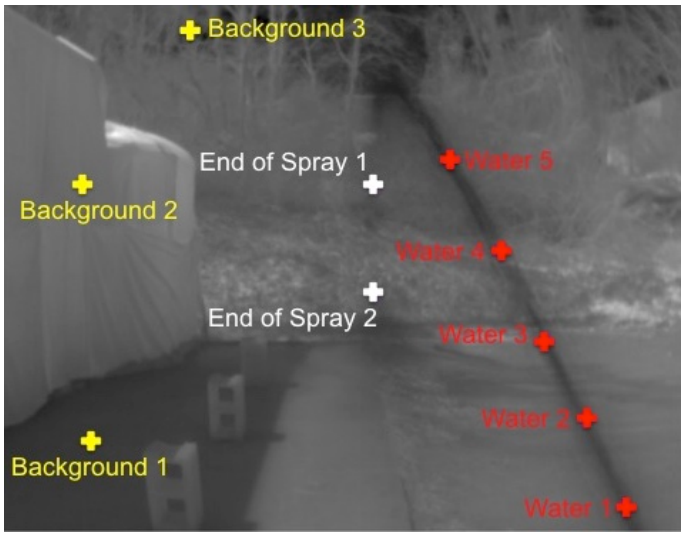

Figure 3.3. Point selection in IR image for plotting intensity vs. time.

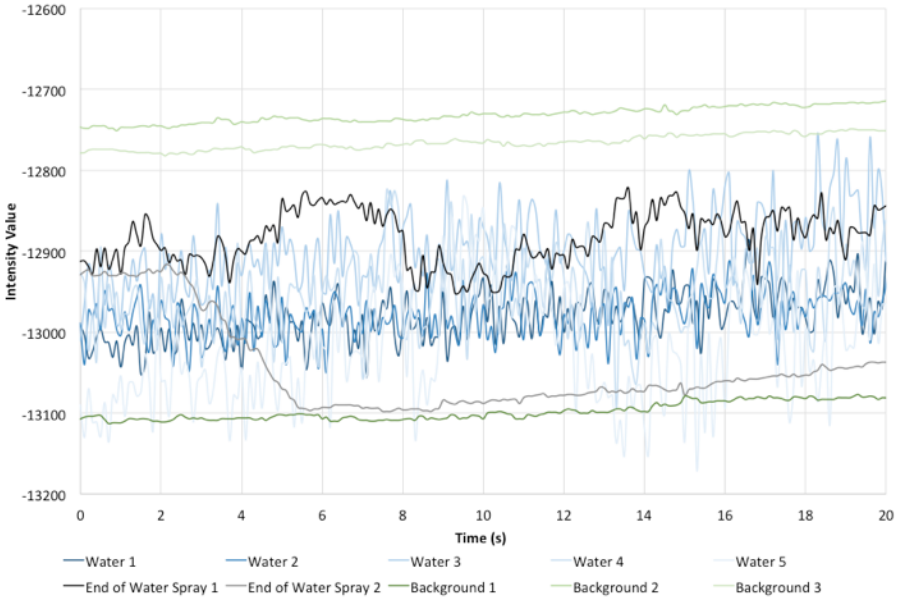

Figure 3.4. Intensity value of points selected in Fig. 3 versus time.

In Figure 3.4 the points associated with the water spray produce a larger variance between frames than pixels associated with background regions. For the pixel locations selected representing the end of the spray, the variation between images is smaller than the pixels selected in the start of the spray. At the landing zone of the spray, the intensity variation of a single pixel is similar to that of a stationary background location such as a wall or ground pixel. This is due to droplet breakup occurring further along the spray trajectory causing acquisition of the internal water spray structure difficult. The first step in the segmentation process was to measure the difference between three consecutive frames. $\boldsymbol{M_1}$ is the difference image obtained by subtracting frame $k-1$ from frame k and taking the absolute value and $\boldsymbol{M_2}$ the difference between frame $k-1$ and frame $k-2$. A motion threshold, T_M, applied is 75% of the maximum difference value in either $\boldsymbol{M_1}$ or $\boldsymbol{M_2}$. Equations 1-3 give the two difference images and motion threshold calculation. The threshold percentage was determined heuristically and preserves the regions with large differences and eliminates regions that appear to change due to small intensity variations because of the inherent noise in IR images or slight camera motion.

$$M_1(x,y) = \left| f_k(x,y) - f_{k-1}(x,y) \right| \tag{1}$$

$$M_2(x,y) = \left| f_{k-1}(x,y) - f_{k-2}(x,y) \right| \tag{2}$$

$$T_M = 0.75 \times \left(argmax\left(M_1(i,j) \cup M_2(i,j) \right) \right) \tag{3}$$

A set of binary images $\boldsymbol{D_1}(x,y)$, Eq. 4, and $\boldsymbol{D_2}(x,y)$, Eq. 5, are created using the motion threshold to preserve the high motion regions. A third binary image $\boldsymbol{D_3}(x,y)$, Eq. 6, uses an intensity threshold that is either manually set based on knowledge about the water intensity range or automatically adjusted by determining the highest intensity value associated with a pixel that is greater than the motion threshold value in $\boldsymbol{D_1}$ and $\boldsymbol{D_2}$. The intensity threshold, T_I, can also assist in removing hot objects, fire reflections, hot smoke, and fire from the scene to further reduce the number of potential water objects and is selected based on intensity values of smoke, fire, and hot objects.

$$D_1(x,y) = \begin{cases} 1, \left| f_k(x,y) - f_{k-1}(x,y) \right| \geq T_M \\ 0, \left| f_k(x,y) - f_{k-1}(x,y) \right| < T_M \end{cases} \tag{4}$$

$$D_2(x,y) = \begin{cases} 1, |f_{k-1}(x,y) - f_{k-2}(x,y)| \geq T_M \\ 0, |f_{k-1}(x,y) - f_{k-2}(x,y)| < T_M \end{cases} \quad (5)$$

$$D_3(x,y) = \begin{cases} 1, f_k(x,y) < T_I \\ 0, f_k(x,y) \geq T_I \end{cases} \quad (6)$$

The binary image $\boldsymbol{D}(x,y)$, Eq. 7, is processed by setting the pixel value to 1 if the value is 1 in $\boldsymbol{D_1}$, $\boldsymbol{D_2}$, and $\boldsymbol{D_3}$.

$$D(x,y) = \begin{cases} 1, D_1(i,j) \cap D_2(i,j) \cap D_3(i,j) = 1 \\ 0, D_1(i,j) \cap D_2(i,j) \cap D_3(i,j) = 0 \end{cases} \quad (7)$$

Examples of the binary images using the above equations are shown in Figure 3.5 along with the raw IR image and a visual image of the water spray. Figure 3.5(c) and Figure 3.5(d) show the two difference images $\boldsymbol{M_1}$ and $\boldsymbol{M_2}$. Figure 3.5(e) is the binary image $\boldsymbol{D}(x,y)$. Figure 3.5(f) uses the binary image in Figure 3.5(e) to highlight pixels blue for display over the IR image.

(a) (b)

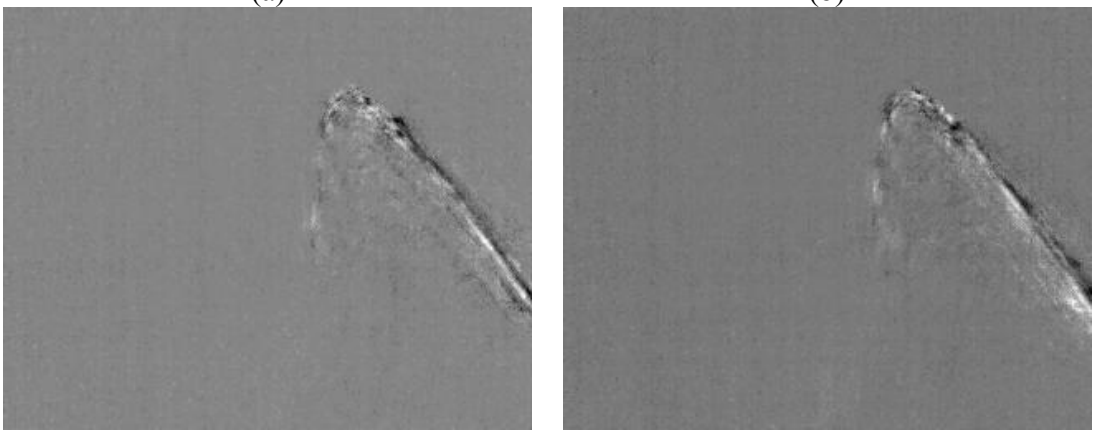

(c) (d)

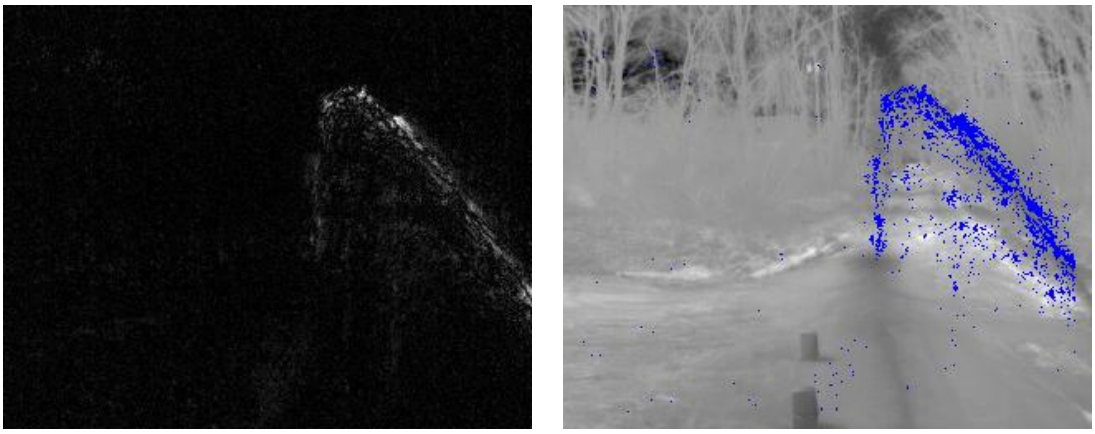

(e) (f)

Figure 3.5. (a) Visual image (b) IR image (c) M_1 (d) M_2 (e) D (f) IR image with segmented pixels in (e) highlighted in blue

3.4.2 Morphological Filtering and Candidate Extraction

The motion segmentation technique along with the intensity and motion threshold steps were used to segment pixels from the IR image that undergo a large change between three consecutive frames. A binary image $\boldsymbol{D}$ was created containing all candidate pixels represented as 1 and all other pixels 0. Typically, the resulting candidate regions using this basic filtering approach are noisy as in Figure 3.5(f). Mathematical morphology operations "opening" and "closing" were used to remove noise and extract final candidate regions for classification. Candidate pixels in close proximity were connected using a diamond structure element (3 x 3) and "holes" within a candidate ROI were filled to connect the internal regions of the candidates. The binary image was filtered to eliminate small components in the image if the size of the object is less than a specified number of pixels. It was found that a small object often contains unreliable texture features for classification. The original 14-bit image was convoluted with the filtered binary image so that a ROI contains the original 14-bit intensities at pixel locations that were segmented with all other pixels in the image set to 0. An example of the IR image before and after the morphological operations is shown in Figure 3.6. Smaller regions segmented prior are eliminated leaving two candidates in the image.

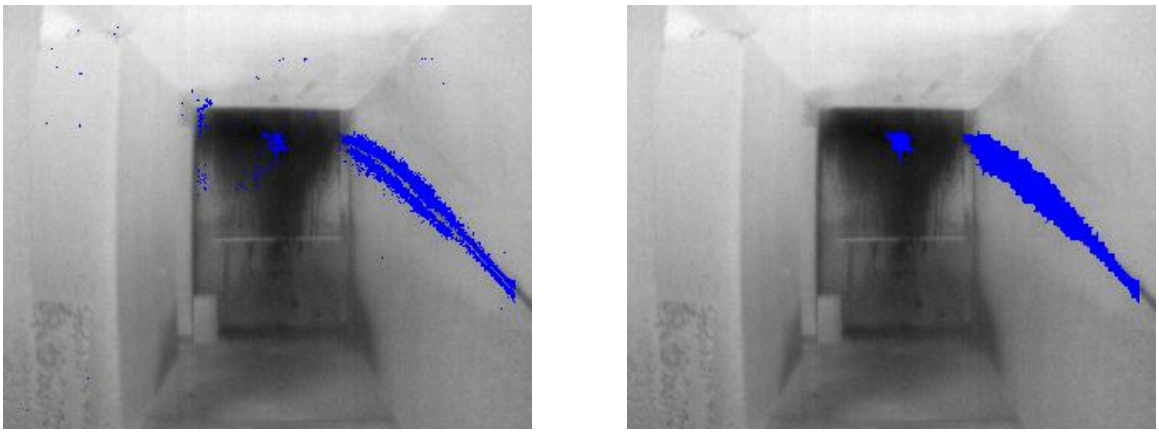

(a) (b)

Figure 3.6. (a) Processed IR image with segmented candidate regions (b) IR image with regions after morphological operations

3.4.3 Segmentation Accuracy

The performance of the segmentation process was measured by calculating the overlap between the segmented image at time, *t*, and a reference image. Since an established dataset for water spray in IR is not available, a reference image of the spray was developed for each video by averaging the binary image ***D*** in Eq. 7 over an entire dataset. An example reference spray image is provided in Figure 3.7 for an outdoor water spray. The image is a scaled version (0-1) of the mean intensity rate of change for each pixel in the image array. The middle of the water spray shows the highest mean rate of change and the edges of the spray where droplets break away from the internal region exhibit higher rates of change than background regions including trees moving back-and-forth at the top of the image.

Figure 3.7. Mean rate of change image for outdoor water spray over entire image set.

The ground truth image is calculated by applying a threshold to the mean intensity rate of change of each pixel. Two separate reference spray images are depicted in Figure 3.8 for motion thresholds, T_M, of 30 and 40. The threshold corresponds to the change in intensity at each pixel over three consecutive frames averaged over the entire image set (>1000 frames).

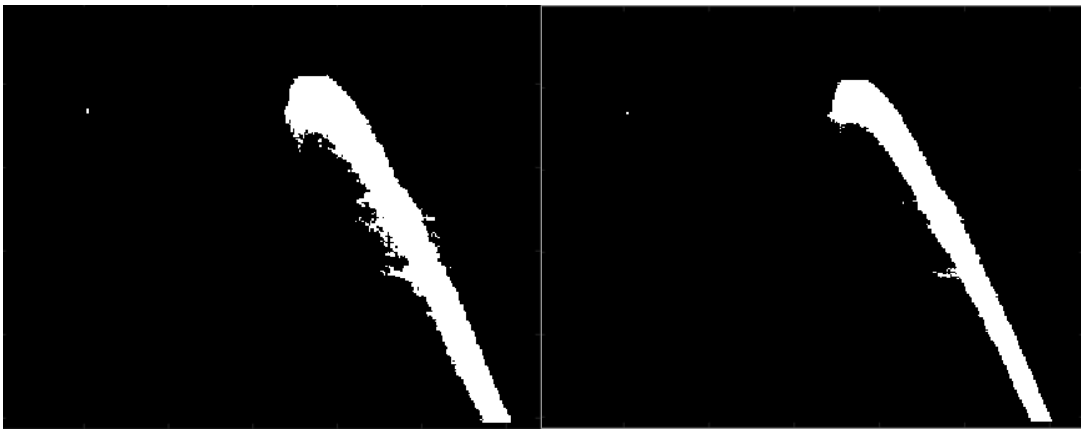

(a) (b)

Figure 3.8. Reference spray image with mean change threshold of (a) 30 (b) 40.

To index the performance of the segmentation pre-processing step, a segmented image is compared to the ground truth in Figure 3.8(b) for every frame. The four parameters: *false positives, false negatives, true positives, true negatives,* are used as entries to a confusion matrix to compare the results of segmentation. Precision and recall are plotted in Figure 3.9 for water spray in an outdoor environment without fire or smoke. The results tend to skew towards the upper-right corner indicating high performance of the segmentation process. The true positive rate is plotted against the false positive rate in a ROC curve in Figure 3.10. Again, the performance is high as the results lie in the upper-left corner indicated a high TPR and low FPR.

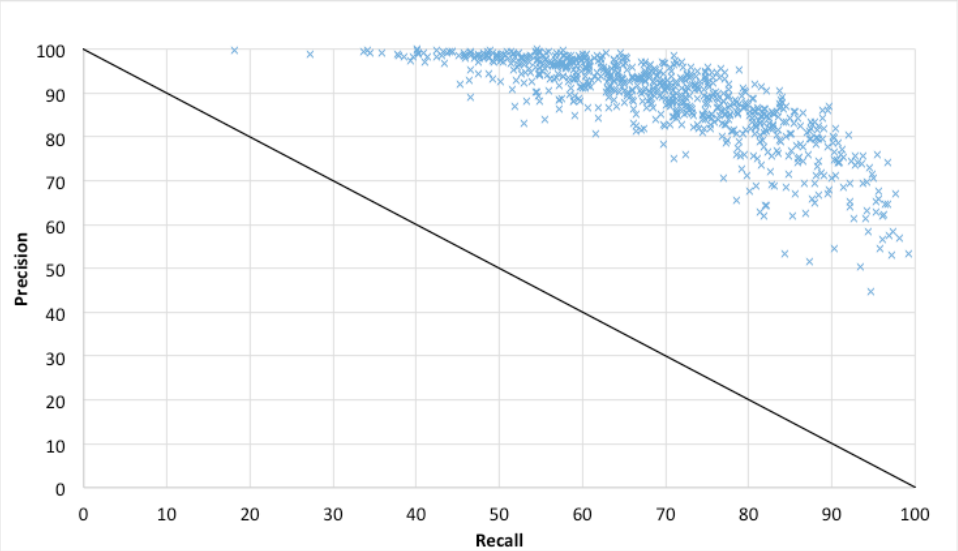

Figure 3.9. Precision vs. recall of segmentation pre-processing step.

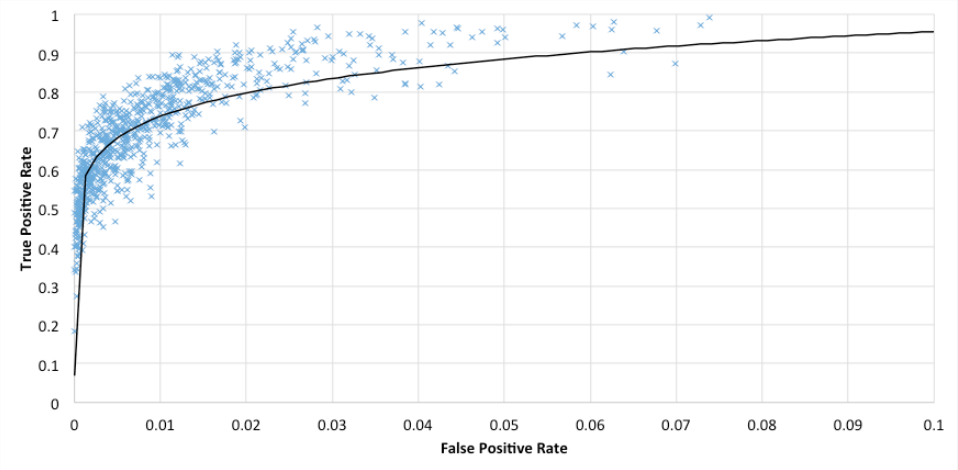

Figure 3.10. True positive rate vs. false positive rate of segmentation processing.

3.5 Image Analysis and Classification

3.5.1 Statistical Texture Features

The pre-processing stage results in a number of candidate regions that may be water or other non-water objects. Other candidates may appear due to camera motion or moving objects in the scene (e.g. tree leaves, reflections, fire, smoke). Due to the fact that texture features are less influenced by rotation/motion [80], they are used to characterize the candidate regions. Textures in the 14-bit gray level array have a high-resolution spatial distribution, which is useful in classifying patterns of water against non-water objects for classification.

First order statistical textures such as mean and variance are computed using the intensity histogram of a candidate ROI in the image. For collecting second order statistical textures, the gray-level co-occurrence matrix (GLCM) introduced by Haralick [81] has been widely used and offers a number of descriptors for classifying objects. The GLCM considers the spatial relationship of adjacent pixels in eight directions (horizontal, vertical, left and right diagonals) by quantizing the spatial co-occurrence of neighboring pixels. Figure 3.11 shows the co-occurrence matrix with distance $d = 1$ and the direction is horizontal, $\theta = 0$, so that the relationship is the nearest horizontal neighbor. A pixel pair of (0,0) is placed into the first index of the GLCM and a normalized GLCM is formed by dividing each array index by the total size of the GLCM.

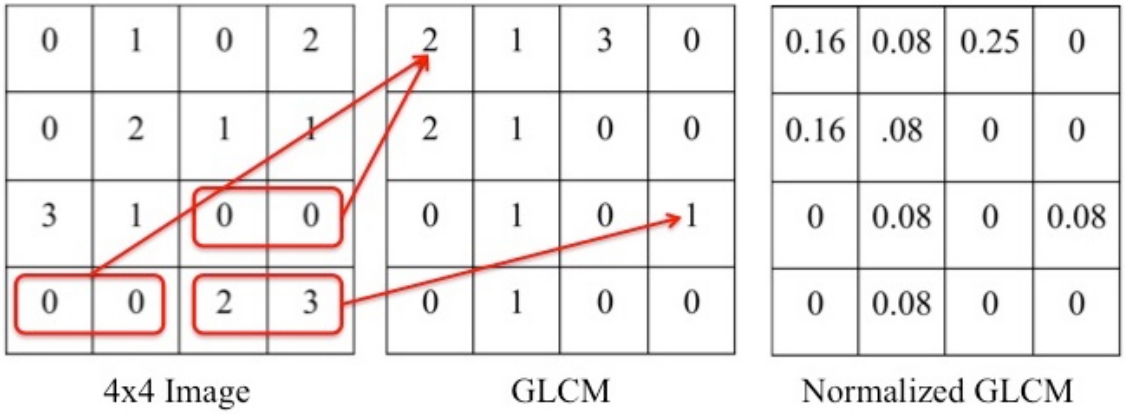

Figure 3.11. GLCM and Normalized GLCM construction from a 4x4 image block.

A total of twelve second-order statistics features were used including the following: correlation (COR), contrast (CON), entropy (ENT), dissimilarity (DIS), energy (ENG), homogeneity (HOM), autocorrelation (ACOR), information measures of correlation (INF, INF2), inverse difference normalized (INVN), inverse difference moment normalized (IDMN), and maximum likelihood (MPR). With the twelve second-order features along with spatial relationships between pixels at (0°, 45°, 90°, 135°) a feature vector is formed with 48 components. The third and higher order statistic features investigated in [82] are not considered due to the computational expense of applying these.

Second-order features were computed with a normalized co-occurrence matrix

$$C_{ij} = \frac{P_{ij}}{\sum_{i,j=1}^{N_G} P_{ij}} \tag{8}$$

where P_{ij} refers to the total number of occurrences of a pixel of gray-level *i* being adjacent to a pixel of value *j* within the four directions (0°, 45°, 90°, 135°). N_G denotes the number of grey levels in the quantized image used to scale the intensity values. A total of 32 grey levels were used to scale down the 14-bit range of intensity values. The denominator in Eq. 8 represents the total number of *i* and *j* pairs and normalizes P_{ij} so each entry is considered as a probability that a pixel with value *i* is found adjacent to a pixel of value *j*. After building the normalized co-occurrence matrix $C_{i,j}$, twelve features were extracted and are listed in Table 3.1 along with variance. Mean was not considered as a feature descriptor because the intensity of a water object will change based on the water temperature. Dissimilarity and contrast represent the degree of smoothness and entropy is a reflection of the degree of repetition among the gray-level pairs. For more details on the statistical features first designed by Haralick, see [81, 83-85].

Table 3.1. Features extracted from GLCM

Index	Feature	Index	Feature
1	Correlation	7	Autocorrelation
2	Contrast	8	Information measure of correlation (1)
3	Entropy	9	Information measure of correlation (2)
4	Dissimilarity	10	Inverse difference normalized
5	Energy	11	Inverse difference moment normalized
6	Homogeneity	12	Maximum Probability

$$COR = \sum \frac{(ij + \mu_i\mu_j - \mu_i - \mu_j)C_{ij}}{\sigma_i\sigma_j} \tag{9}$$

$$CON = \sum C_{ij}|i - j|^2 \tag{10}$$

$$ENT = \sum C_{ij} log C_{ij} \tag{11}$$

$$DIS = \sum C_{ij}|i - j| \tag{12}$$

$$ENG = \sum {C_{ij}}^2 \tag{13}$$

$$HOM = \sum \frac{C_{ij}}{1 + |i - j|} \tag{14}$$

$$ACOR = \sum (i - j) C_{ij} \tag{15}$$

$$INF = \frac{HXY - HXY1}{\max (HX, HY)} \tag{16}$$

$$INVN = \sum \frac{C_{ij}}{1 + |i - j|^2} \tag{17}$$

$$IDMN = \sum \frac{C_{ij}}{1 + (i - j)^2} \tag{18}$$

$$MPR = \max (C_{ij}) \tag{19}$$

$$INF2 = (1 - exp[-2(HXY2 - HXY)])^{1/2} \tag{20}$$

A total of 17 videos with 20,968 frames and 65,381 candidates were collected from the experiments and divided into two different datasets, a training and test set. The training database used in classification contained 11 IR video sequences with a total of 11,764 frames. Table 3.2 contains the 11 video set along with the number of frames in each set and a description of each. A variety of scenarios were included in the test set including varying temperature water streams in front of a uniform temperature background. For leaks, a water line was mounted vertically above the IR cameras. The leaks were approximately 2 cm in diameter and the water temperature was adjusted for various tests between 15° C and 35° C.

Outdoor tests were recorded with different spray patterns to vary the width of the spray and multiple pitch angles to vary the spray height. Tests were also recorded inside a large-scale test facility in clear conditions and in low-visibility conditions with a smoke layer obstructing view of a traditional RGB camera. Cluttered backgrounds and motion objects related to reflections and non-water moving objects were included for training. To collect the candidate ROI's, the motion segmentation process was applied on the IR video and each ROI was manually labeled as water or non-water. GLCM's were calculated for each candidate ROI where the segmented pixels were represented by the 14-bit intensity value while all other pixels within the image were set to 0. Adjacent pixel pairs containing a 0 value were then ignored as a pixel pair for processing each texture feature.

Table 3.2. Summary of video in training database

Video	Duration (Frames)	Description
#1	264	7° C water stream in front of white background
#2	900	35° C water stream in front of white background
#3	1,100	21° C water stream in front of white background
#4	1,000	Varying spray widths outside (outward and across camera plane)
#5	1,500	Varying spray angle outside (0-20°)
#6	1,100	Water spray in hallway
#7	900	Water spray in hallway with low visibility conditions
#8	500	Water mist nozzle in front of cluttered background
#9	1,200	Smoke in low visibility hallway
#10	1,500	Background motions and tree motion outside
#11	1,800	Cluttered background objects

3.5.2 Bayesian Classification

Supervised machine learning classification methods were considered to train and classifying the candidates from the test dataset. In *k*-nearest neighbors (*k*-NN) classification, an object is classified using a majority voting process to place the object in the class most common among *k* neighbors [86]. This method requires a large amount of memory and is computationally expensive with large amounts of data [87]. The Naïve Bayesian classification method is based on Bayes' theorem. While the accuracy of this method is typically lower than other methods, it is computationally fast, robust in the analysis of missing values and not as prone to the overfitting problem [87-88] associated with machine learning techniques. Unlike Bayesian classification, neural networks do not have strong assumptions on probability distributions. Neural networks have fast computational time and flexibility to complexities of the system but are inefficient when presented with missing or irrelevant data and are prone to overfitting [89]. Support vector machines (SVMs) are supervised learning models that find a separating hyperplane with the greatest possible margin between two sets of data. SVMs provide fast computation and the highest accuracy among classification methods [89] but the texture features used for water and non-water were often non-

separable resulting in a large number of support vectors which makes confidence in the classification low and processing time high due to the amount of support vectors to store. Bayesian classification was chosen due to its probabilistic decisions, lower chance of overfitting, and fast computation for real-time implementation on a suppression system.

For several given features $F_1, F_2, \ldots, F_q$, the probability that class C_j corresponds to a candidate k can be calculated using a conditional probability, ${}^{k}p\left(C_j \middle| F_1 F_2 \ldots F_q\right)$, also known as the posterior probability. For a dataset, the prior probability was calculated by dividing the number of candidates in each class by the total number of candidates in the dataset. The likelihood function is calculated by applying a conditional independence assumption and is written as follows:

$$f\left(F_1 F_2 \ldots F_q | C_j\right) = \prod_{i=1}^{q} f\left(F_i | C_j\right) \tag{21}$$

Gaussian (normal) distributions were assumed for the features and classes. Gaussian parameters for thirteen features with respect to water and non-water objects were estimated using the maximum likelihood estimation [90]. Bayesian classification was used to predict the class and probability of each candidate in the scene using the maximum priority decision rule, which determines which class produces the larger posterior probability.

3.5.3 Single Feature Performance

Resubstitution and k-fold cross-validation error [91] were used to measure the performance of each feature in classification. The results of each feature are shown in Table 3.3. The second order statistical texture features energy (ENG), autocorrelation (ACOR), and entropy (ENT) produced the lowest errors while the two second order features dissimilarity (DIS), and contrast (CON) showed the highest error. These results show that ENG, ACOR, and ENT are beneficial to distinguish water from non-water objects. DIS and CON are not useful in classification due in part to the small range of intensities associated with a water object ROI.

Table 3.3. Performance of a single feature in classification

Feature	Resubstitution Error (%)	Cross-Validation Error (%)
Autocorrelation (ACOR)	24.24	24.24
Contrast (CON)	45.37	45.41
Entropy (ENT)	24.44	24.45
Dissimilarity (DIS)	44.68	44.68
Energy (ENG or UNI)	23.98	23.98
Homogeneity (INV or HOM)	27.19	27.18
Correlation (COR)	33.27	33.30
Information Measure of Correlation (INF)	37.22	37.24
Inverse Difference Normalized (INVN)	35.39	35.39
Inverse Difference Moment (IDM)	38.06	38.17
Max Probability (MPR)	27.76	27.76
Variance (VAR)	31.11	31.16

3.5.4 Multiple Feature Performance

A single feature cannot accurately classify water as shown by the single feature classification performance in Table 3.3. All possible combinations of the features used were analyzed to find the optimal combination of the features to produce the lowest classification error. The total number of combinations with two or more features is

$$N_{total} = \sum_{j=2}^{m} mC_j \quad (22)$$

where m is the total number of features (m = 12) and j the number of feature combinations. A multi-objective genetic algorithm optimization in the MATLAB global optimization toolbox [92] was used to find the best combination out of all combinations (4095) with the lowest error. The objective functions resubstitution and k-fold cross-validation error [91] were used to measure the accuracy of each combination in classification.

The most promising feature combinations are shown in Figure 3.12. The behavioral region was defined to contain all feature combinations with less than 16% error for both objective functions. The behavioral set contains 0.78% of all possible feature combinations. Feature

prevalence in the behavioral region is shown in Figure 3.13. The first order statistic texture features MPR and INVN had a 100% occurrence while second-order features HOM, ENG, and ENT and first-order feature VAR had 0% occurrence.

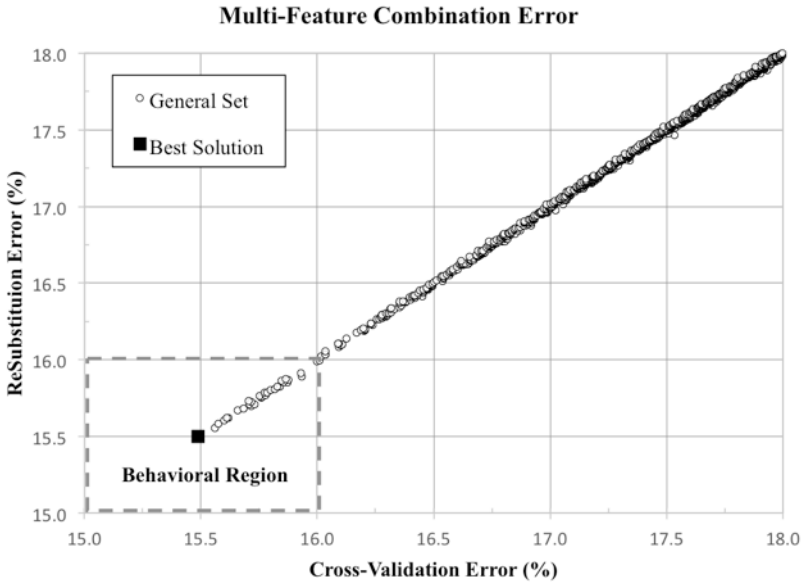

Figure 3.12. Multi-objective optimization result showing the general set, behavioral region, and the best solution.

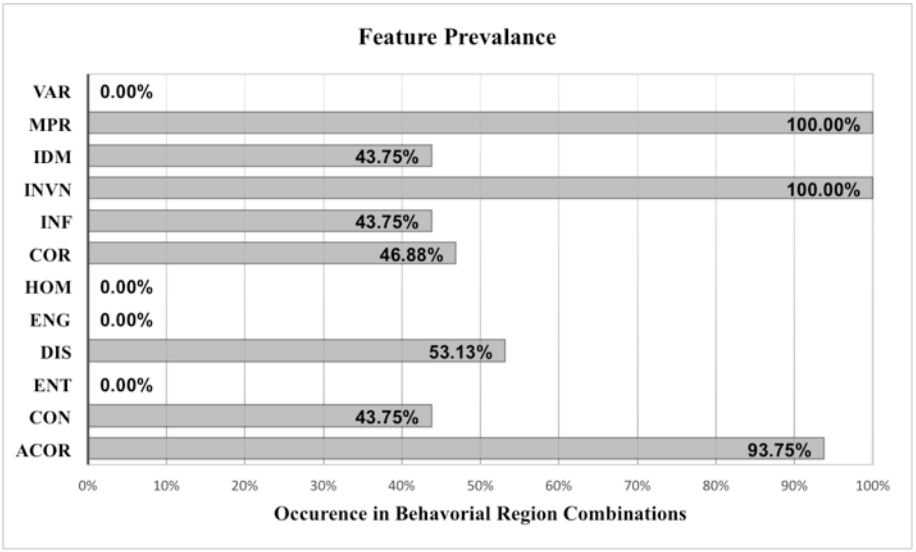

Figure 3.13. Feature prevalence of the twelve features in the behavioral region.

The top features based on the feature prevalence in the behavioral region in Figure 3.12 were MPR, INVN, and ACOR. The classification performance of the ten best combinations of features resulting in less than 16% error is shown in Table 3.4. The combination of the four most prevalent features in the behavioral region, MPR, INVN, ACOR, and DIS, was also the best solution with the lowest error of both objective functions, 15.50% and 15.49%. Normal distributions are assumed for each feature of each corresponding class in the training dataset. The Gaussian parameters mean, μ, and standard deviation, σ, assuming a normal distribution, for the four features in the best combination with respect to each class are shown in Table 3.5.

Table 3.4. Combination of features in the behavioral solution set with 10 lowest error percentages

Feature Combination	**Error (%)**	
	Resubstitution	**Cross-Validation**
ACOR, DIS, INVN, MPR	15.50	15.49
ACOR, DIS, INVN, IDM, MPR	15.56	15.56
ACOR, DIS, INF, INVN, MPR	15.57	15.57
ACOR, VAR, DIS, INVN, MPR	15.60	15.60
ACOR, DIS, INF, INVN, IDM, MPR	15.62	15.62
ACOR, DIS, COR, INF, INVN, MPR	15.61	15.62
ACOR, INVN, MPR	15.66	15.67
ACOR, CON, DIS, INF, INVN, MPR	15.68	15.68
ACOR, DIS, COR, INVN, MPR	15.72	15.70
ACOR, DIS, COR, INF, INVN, IDM, MPR	15.71	15.71

Table 3.5. Gaussian parameters for the four top texture features

Feature	Water		Non-Water	
	μ	σ	μ	σ
Autocorrelation (ACOR)	736.053	132.303	430.249	202.678
Dissimilarity (DIS)	2.948	2.530	1.941	1.333
Inverse Difference Normalized (INVN)	0.964	0.026	0.958	0.019
Max Probability (MPR)	0.668	0.151	0.127	0.248

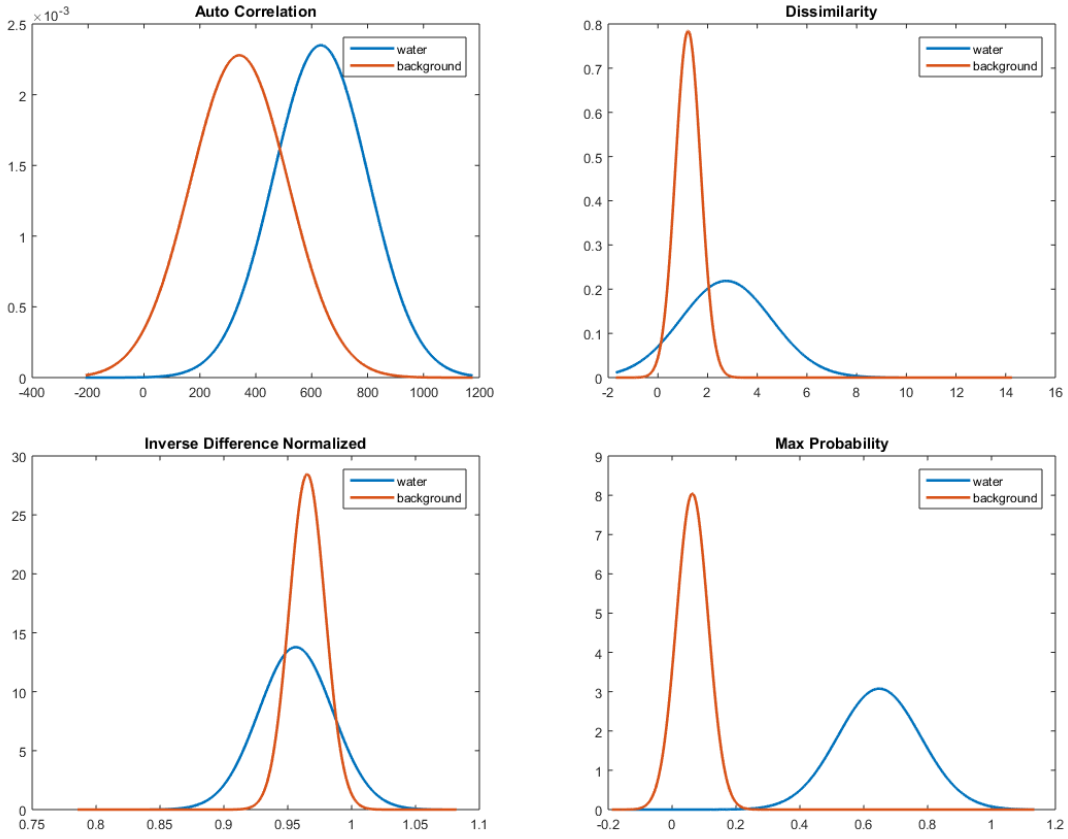

Figure 3.14. Probability density distributions of features used for water classification.

3.6 Test Dataset

The Bayesian classification method was trained and then evaluated with a separate dataset in a variety of scenarios with water. Test scenarios included water sprays and leaks in low and high visibility conditions, indoor and outdoor environments, various water temperatures, and with and without a fire in the scene. The test dataset used to evaluate the algorithm consisted of 6 videos with 9,203 frames and 20,793 candidates, approximately the remaining one third of data. Each

candidate object had five corresponding data points (four second-order features and class) for a total number of data points used of 326,905. The training dataset was used to estimate the Gaussian parameters of the classification model and the test dataset was used to validate performance. Table 3.6 contains a summary of the videos used in the test dataset along with the number of frames.

Table 3.6. Summary of videos in test database

Video	Duration (Frames)	Description
#12	3,573	Outdoor water spray with varying tilt angles
#13	5,158	Outdoor water spray with fire in field of view
#14	1,189	21° C water stream in front of white background
#15	1,425	Water spray in high visibility indoor conditions
#16	979	Water spray in low visibility indoor conditions
#17	1,400	Humanoid robot fire suppression test onboard ship

3.6.1 Experimental Scenarios

A fire source consisting of a 150 mm × 150 mm × 150 mm latex foam block was used within a hallway setup to produce low visibility conditions. Latex foam fires produce lower temperature conditions but dense, low visibility smoke. Once the hallway was filled with the smoke, water was sprayed in a tight spiral pattern and moved side-to-side and up-and-down within the hallway producing a mixture of smoke and water vapor inside the structure. The same water spray pattern was used without smoke in the hallway setup.

The outdoor tests in the training set included a fire in the field of view to test the ability of the classification and segmentation method to distinguish and eliminate fire and smoke as water objects. The shipboard fire suppression test was taken with IR cameras mounted on a humanoid robot. The robot held a firefighting nozzle and the right arm was manually operated to suppress a wood-crib fire. The dynamics of the robot balancing with the water nozzle caused the IR camera to move slightly through the duration of the test, evaluating the ability of the approach to be effective with some motion due to the robot.

3.7 Results

The proposed algorithm was developed and tested using data from a set of videos with varying water temperatures, spray patterns, and background conditions. The error in the classification is quantified for images in several environments and with the vision system on different platforms.

3.7.1 Display

Figure 3.15 contains visual and thermal images from each of the videos in the test dataset. Each row corresponds to a test set with the visual image, raw IR image, and IR image with the candidates highlighted in blue and outlined with a red ellipse. If the candidate was classified as water, the posterior probability along with a text marker is overlaid on the candidate. Fig. 3.15(a) contains results from an outdoor water spray test. Due to the higher contrast of the water spray and largely static background, the spray is easily segmented and classified as water. Some small objects representing regions of motion (i.e. trees, noisy regions) were removed with morphology. In Figure 3.15(b) a fire was placed in the field of view of the outdoor spray test. This introduced smoke into the scene and some smaller regions above the fire were extracted as ROIs but not classified as water.

Figure 3.15(c) includes images from a water leak in front of a white background Figure 3.15(c1). In the visual image, water is indistinguishable from the background and in IR, Figure 3.15(c2), blends in with the background. Some reflections occur in this environment at the locations with smooth metal objects but were removed through the morphological filtering process.

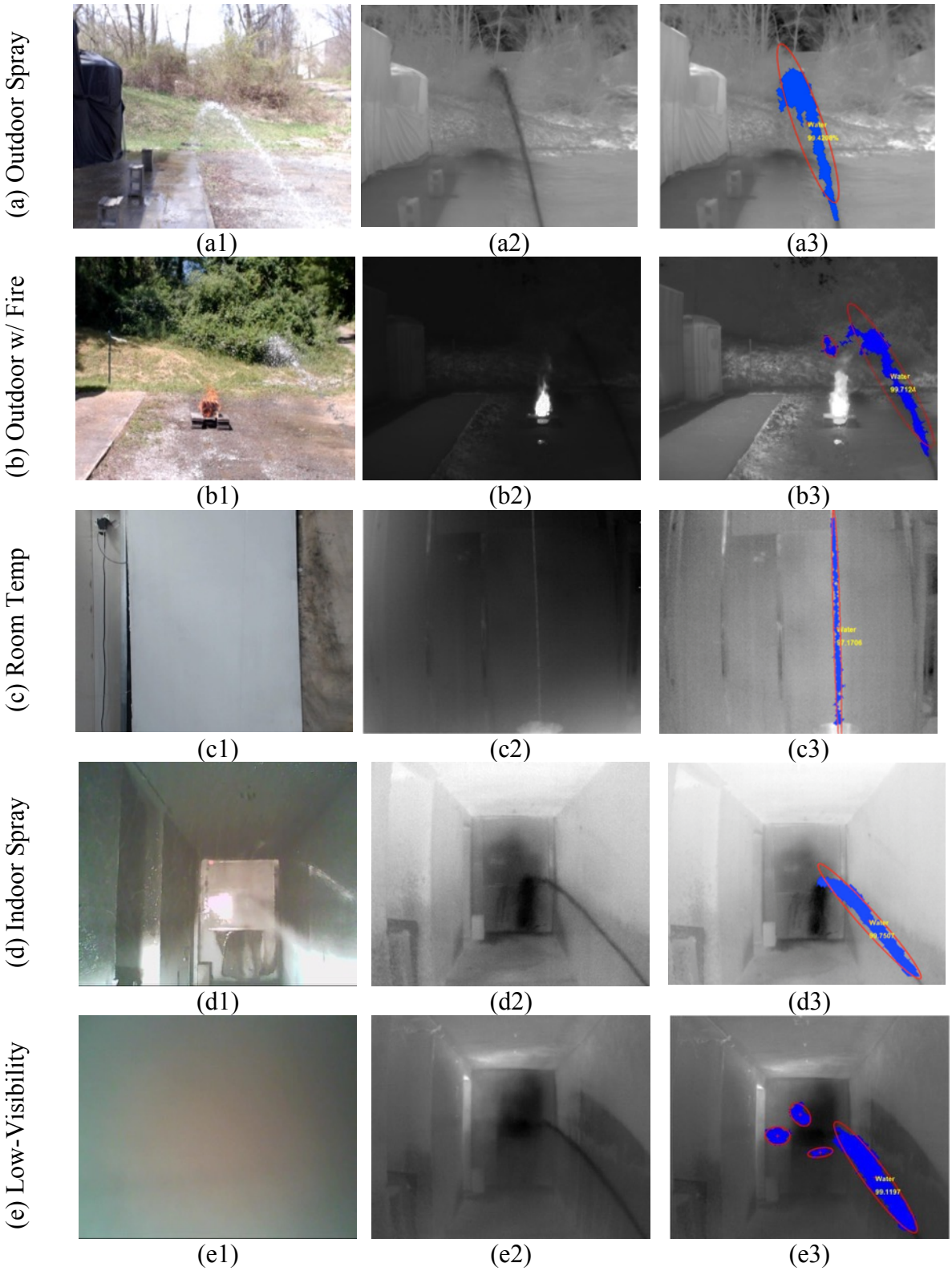
(a) Outdoor Spray
(a1)
(a2)
(a3)
(b) Outdoor w/ Fire
(b1)
(b2)
(b3)
(c) Room Temp
(c1)
(c2)
(c3)
(d) Indoor Spray
(d1)
(d2)
(d3)
(e) Low-Visibility
(e1)
(e2)
(e3)

(f1) Visual (f2) Thermal (f3) Classification

Figure 3.15. Classification results from test dataset with various water temperatures, patterns and environments.

Figure 3.15(d) contains images from an indoor water spray test. In the visual image provided in Figure 3.15(d1), some light reflections along with some visibility limitations occur due to stirring up dust in the test setup by the water spray. The water spray is segmented and classified as water in Figure 3.15(d3). Figure 3.15(e) includes images from a test where water is sprayed into the hallway shown in Figure 3.15(d) but with smoke and steam filling the hallway length. The visibility conditions completely obstruct the view of the visual image in Figure 3.15(e1), but IR provides a view of the environment in Figure 3.15(e2). This scene represents a more dynamic scene due to the smoke and steam circulating in the environment. The last row shows a fire suppression tests onboard a ship with a humanoid robot. Visually, the scene appears darker except where the fire is located, and the water has a very different appearance throughout the length of the spray. Note that the water spray nozzles in Figure 3.15(a), Figure 3.15(b), Figure 3.15(d), and Figure 3.15(e) are the same (4.76 gpm at 0.34 MPa); however, the water spray in Figure 3.15(f) is a ship firefighting nozzle operating at 10-20 gpm and 0.69 MPa.

3.7.2 Analysis

To measure the accuracy of the proposed method, resubstitution and *k*-fold cross-validation error criterions were applied to analyze classification results. The entire dataset is used by resubstitution error to compare the manually labeled class against the predicted classes by the proposed method. This error criterion used independently can result in the classification being overfit to the training data and is not a good indicator of performance on future data. Cross-validation error is often used to detect and prevent the overfitting problem. It estimates the performance by splitting the data up into *k* number of subsets of equal size. Each subset is held out

as a test set while the rest of the data is used to train the model. By averaging the metric over all *k*-folds, an estimate is given for the performance of the classification model.

Table 3.7 includes the resubstitution and cross-validation errors determined from the test dataset of six various scenarios involving water sprays provided in Figure 3.15. Although there is less than 10% error in general, Video 14 had higher error rates due to the misclassification that occurred between water and some larger reflections. The leak results in much smaller regions to classify resulting in less certainty in the classification. Video 17 has resubstitution and cross-validation errors of 6.87% and 6.78%, respectively, despite the fact that some candidates were extracted due to robot motion. In the shipboard test, a portion of the water spray nearest to the fire was not segmented due to a very low contrast between the water and background. The entire performance of the test dataset is assessed at 5.97% of the resubstitution error and 6.30% of the cross-validation error.

Table 3.7. Test dataset results

Video	Frames	Candidates	Source	Re-Substitution Error (%)	Cross-Validation Error (%)
#12	3,573	8,677	Outdoor	7.95	7.93
#13	5,158	10,018	Outdoor w/ Fire	4.73	4.76
#14	1,189	418	Room-Temp Leak	9.33	9.81
#15	1,425	1,741	High-Vis Indoor	7.64	7.69
#16	979	490	Low-Vis Indoor	7.35	6.94
#17	1,400	2,686	Shipboard Suppression	6.87	6.78
Total	13,724	24,030		5.97	6.03

A confusion matrix heat map is used to quantitatively visualize the performance of the proposed method in Figure 3.16. True predictions are located on the diagonal of the matrix and false predictions on the diagonal. The values of the heat map from the top left and in a clockwise direction represent true-positives, false-negatives, true-negatives, and false-positives.

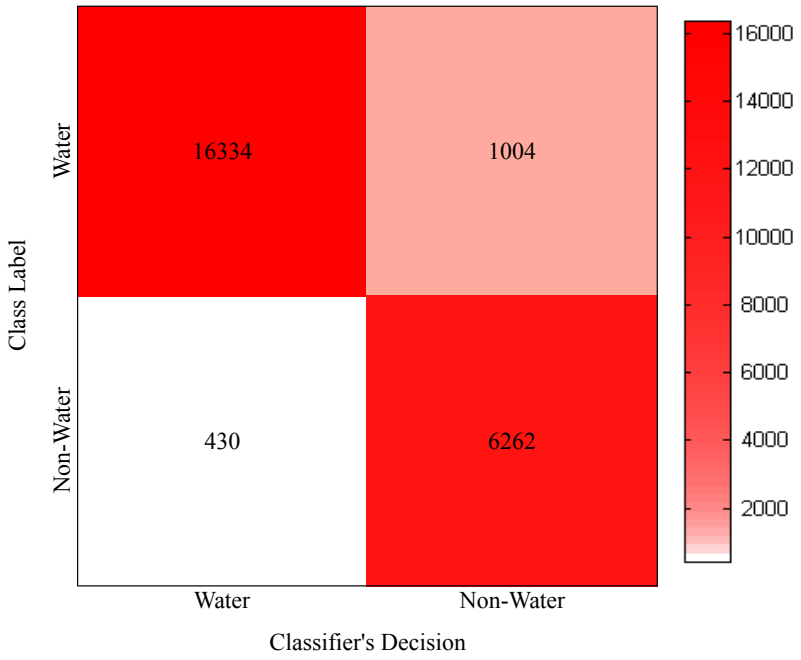

Figure 3.16. 2 × 2 confusion matrix heat map of test dataset results

As seen in Figure 3.16, the proposed method has high accuracy in predictions with the test dataset when distinguishing water from non-water objects. Water is more often classified as non-water (top-right) than non-water being classified as water (bottom-left), which may be attributed to a smaller ROI resulting in a smaller amount of adjacent pixel relationships. Smaller regions may refer to the total number of pixels in an object or a very narrow ROI with a limited amount of pixels left or right of the middle pixel used to form the GLCM. Performance was also measured through analysis of the relevance between classes by using the confusion matrix in Figure 3.16 to assess four types of measurements; recall, precision, F-measure (F-score) and G-measure (G-score). Recall is a measure of the percentage of positive examples from the positive group of the actual class and precision measures the fraction of positive instances (true positives) from the group that the classifier predicted to be positive. F-measure, Eq. 23, is the harmonic mean of precision and recall and G-measure, Eq. 24, is the geometric mean of recall and precision.

$$F - Measure = \frac{2 \cdot (recall \cdot precision)}{recall + precision} \tag{23}$$

$$G - Measure = \sqrt{recall \cdot precision} \tag{24}$$

Table 3.8 contains the quantitative analysis of the two classes versus each other for the test dataset. The non-water classes are classified with 86.1-93.6% accuracy and water is classified with

94.2-97.4% accuracy. The high accuracy in classifying water demonstrates the proposed method can be used to accurately identify the water candidates. The classified water location can then be used within the autonomous fire suppression algorithm or as part of the inspection task process identifying water as a hazard for the robot to avoid or alerting crew of the leak location.

Table 3.8. Quantitative analysis of classification results

Index	Water	Non-Water
Recall	94.2	93.6
Precision	97.4	86.1
F-Measure	95.7	89.7
G-Measure	95.7	89.7

3.8 Conclusion

A real-time probabilistic classification method was presented for identifying water in IR video. The algorithm was developed for use in an autonomous fire suppression system to identify water spray location in real-time to assist a robot in adjusting a firefighting water nozzle so the spray reaches a fire target. The system can be implemented onto a humanoid robot to assist in firefighting activities onboard ships or to identify water leaks as part of inspection tasks. IR cameras were used to collect data due to their ability to effectively image through low to zero visibility environments.

To build a set of training data for classification, candidates were extracted using a three-frame differencing method and morphological operations to eliminate noise and small objects. GLCM was used on extracted candidates to build a feature vector using 12 second-order statistics along with variance for a total of 13 possible features. The training set included water sprays of varying temperature (intensity), patterns, widths, and in various background environments from low clutter to highly dynamic. Training also used non-water objects related to reflections, smoke, and other motion objects. All combinations of features were analyzed to determine the optimal combination of features resulting in the lowest error using two criteria, cross-validation and resubstitution, based on a Bayesian classification method. The most relevant second order statistic texture features

were identified to be autocorrelation, dissimilarity, inverse difference normalized, and max probability.

The classification results were then applied to a separate dataset with videos including outdoor water spray with fire, water in low visibility environments, an actual firefighting demonstration by a humanoid robot onboard a ship, and with water sprayed from three different nozzles. Overall, the classification performance error was determined to be 5.97% based on validation of a test dataset of videos not included in the training set. The precision, recall, F-measure, and G-measure were 86.1 - 97.4% for classifying water and non-water objects using the test dataset with water classification alone having 94.2-97.4% accuracy. The results indicate the method can be effectively used for classifying water sprays for firefighting tasks where the robotic system is relatively stationary. More dynamic systems may require motion compensation to adjust for camera motion, which is an area of future investigation.

4 Spray Trajectory Modeling and Validation Using IR Stereovision

4.1 Introduction

The autonomous suppression algorithm presented in Chapter 2 assumed a linear projection of the spray to determine the desired yaw and pitch angles of the nozzle. This assumption holds for close-range firefighting operations and in high-pressure systems where the spray may be approximated as a straight-line. In order to keep the firefighting robot out of extreme temperature and smoke conditions, firefighting operations from further distances may be necessary. This requires a spray trajectory model to predict the suppressant path and solve for the initial yaw and pitch attack angles to place water on the fire accurately.

To develop a more robust system, adjustments are required due to varying parameters that can alter the path of the suppressant such as wind, and fluctuations in the pressure or flow rate of the line. To develop a fully autonomous robot capable of performing tasks onboard ships, the robot will be required to grasp local objects such as the fire nozzle on deck. Due to the shape of the fire nozzle (shown in Figure 4.1) and difficulty in robot manipulation tasks, the robotic gripper will not always result with the same grip on the nozzle. Improper grips will cause different orientations of the nozzle and the exact nozzle pose is not known to the level of accuracy necessary for fine adjustments. In addition to improper grasps, the wrench on the robotic gripper of a fully charged water line may cause the nozzle to slip in the gripper as the robot is performing firefighting tasks. The unknown direction will present errors between the desired spray trajectory and trajectory at any given time that must to be corrected in order for efficient and accurate fire suppression.

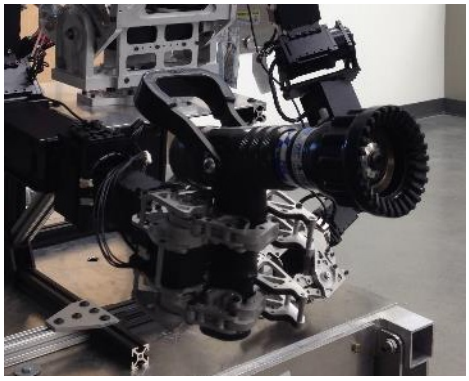

Figure 4.1. Fire nozzle grasped in robot gripper.

Currently, an autonomous fire suppression system has not been designed to correct for errors between fire and spray placement. One automatic firefighting device relies on a vision system moving in parallel with the nozzle to place a detected fire in the center of the image [93]. This approach would assume a linear projection of the spray path which may hold if the fire is in close proximity to the system. Another system uses compensation angles that are experimentally determined prior to adjust the nozzle pitch based on the initial pitch angle [19]. For a desired pitch angle between 15°-20° the nozzle is compensated by adding 2°. In this approach, the assumptions are made that the predetermined compensation angles will always result in successful application of water on the targeted location. The sensor feedback used in these systems is an ON/OFF type fire detector that determines if the fire is still burning or has been suppressed but no closed-loop control is used to correct for errors in the spray location. There is no work shown that corrects for errors in both the pitch and yaw angles in real-time for spray based systems.

A 2D spray model previously validated with a high flow rate fire monitor was adjusted to fit the nozzle parameters used in the large-scale experiments with the current system. The model was then validated with measurements taken with a visual camera and data from an IR stereovision system. To adjust for unknown parameters causing errors in the spray path, real-time trajectory correction was implemented to effectively target a fire and efficiently move a nozzle to prevent fire growth and damage from prolonged placement of water spray off-target of the fire. Water classification is used in a pair of IR cameras to segment the water spray and localize points along the spray path using stereovision. A Golden Section Search method is utilized in determining the optimal angle to minimize error between the localized spray points and trajectory model. The estimate of yaw and pitch angles allows a system to adjust the nozzle based on the error between desired and current spray path.

4.2 Trajectory Modeling

In order to deliver the fire suppressant onto a burning surface efficiently, proper positioning of the nozzle is necessary. This can be accomplished through a discharge trajectory model that predicts the following properties: maximum and/or minimum range, height, and width of the area where water is most concentrated, also called the “footprint” or “landing zone”. The difficulty in predicting spray trajectories lies in varying parameters such as discharge flow, pressure, angle, and also wind velocity and direction that can alter the trajectory path. Prior work developed a three-

dimensional simulation model [94-95] based on the Moving Particle Semi-Implicit (MPS) method [96]. Validity of the simulation results was verified with a comparison of water and foam discharge experiments and the simulation model [97-99]. A "spreadsheet model" was then developed [56] that is a function of trajectory angle, wind speed and direction, and spray pressure and flow rate. The model has been adjusted to fit the spray characteristics of the nozzle used in the autonomous suppression system.

4.2.1 Simulation Model

The 3D simulation model that serves as the basis of the trajectory model developed [56] was constructed based on the MPS method, a simulation technique developed for incompressible fluid dynamics. The governing equations of the MPS method are the continuity equation and the Navier-Stokes equation. Mass, momentum and energy conservation equations are used and transformed to particle interaction equations in simulation. Break-up behavior of the droplets is classified using the Weber Number W_e and viscosity effects of the droplet breakup correlated with the Ohnesorge Number O_n. To simplify droplet behavior, three models: water stream, water mass break-up, and wind turbulence, were used in place of the MPS method to reduce computation time.

Water trajectories vary extremely depending on flow rate, pressure, angle, and wind. Previous work used large-scale water discharges in the simulation model for a range of flow rates (10-40 kL/min), pressures (0.6-0.9 MPa), and pitch angles (30°-50°). Data from large-scale water experiments showed comparable results between the simulation model and experiments with the maximum range and maximum height varying by less than 10%. Discharge characteristics show the maximum range becomes longer by 7% from the standard when only the flow is increased. The increased flow rate results in water mass not readily dispersing with less effect of the trajectory to air resistance. When the pressure is increased the maximum range becomes longer by 16%. If both parameters are increased, the maximum range can become 29% longer. The footprint of spray trajectory exhibits an elliptical shape and is offset to one side of center due to cross winds. The footprint and range of the spray will also vary due to the spray pattern used. For water flows, jets often refer to water flows whose spanwise diameter and streamwise momentum stay approximately the same order of magnitude along the entire path. Water sprays expand in the spanwise diameter and the streamwise momentum will decrease significantly. Solid water jets can deliver water over longer distances but may drive burning materials away from the fire base

resulting in propagation or fire spread. Sprays can increase the coverage area of a system but will result in lower water densities being delivered. A narrow-diameter water spray was used in the suppression system to provide larger coverage of fires at the spray landing zone and increase likelihood of at least a portion of the spray reaching an area of the targeted fire.

4.2.2 Spreadsheet Model

The new model developed by [56] uses a histogram of the water particles' height coordinates at intervals along the discharge axis (distance from the nozzle). A frequency distribution table classifies the particles coordinates as abundance ratios of fluid particles at each distance from the nozzle. This method can be used to develop mass delivery percentage trajectories representing the proportion of particles along the discharge axis per discharge flow. A trajectory of 100% delivery represents the maximum range and height of the spray. The water discharge trajectories, which vary due to flow rate, pressure, angle, wind, and mass delivery percentage, were approximated with a third-order function. The trajectory is dependent on variation in the coefficients of the third-order function that ignores air resistance, Eq. 1.

$$h = -\frac{\rho g}{4Pcos^2\theta}x^2 + \tan(\theta)x + h_o \quad (1)$$

where x is the distance from the nozzle, h_o is the height of the nozzle at distance 0, θ is the nozzle pitch angle, ρ is water density (1000 kg/m^3) and g is gravitational acceleration (9.81 m/s^2).

Pressure P is used because the initial velocity u can be estimated from the discharge pressure using Bernoulli's principle

$$u = \sqrt{\frac{2P}{\rho}} \quad (2)$$

Representative coefficients of the terms x^3, x^2, x^1, and x^0 are set to a_o, b_o, c_o, and d_o respectively. Since there is no x^3 term among the representative values in Eq. 1, coefficient a_o is initially set to zero and increases depending on the effects of the flow parameters. The water discharge trajectory model is then expressed in Eq. 3, with functions for various parameters expressed as Eq. 4-12.

$$h = a_0 G_3(U)G_3(Q)G_3(\theta)M^{-n}x^3 + b_0 G_2(U)G_2(Q)G_2(\theta)G_2(P)x^2 + c_0 G_1(\theta)x + d_0 \quad (3)$$

$$n = 1.2 + 0.019U' + 0.0021U'^2 \quad (4)$$

$$G_3(U) = 1.0 - 0.15U' + 0.0049U'^2 \quad (5)$$

$$G_2(U) = 1.0 + 0.005U' \quad (6)$$

$$G_3(Q) = Q'^{-0.8} \quad (7)$$

$$G_2(Q) = 1.0 - \exp\left(-\frac{Q'+0.1}{5}\right) \quad (8)$$

$$G_3(\theta) = 1.0 - 2.86\theta + 3.0\theta^2 \quad (9)$$

$$G_2(\theta) = (cos\theta)^{-2} \quad (10)$$

$$G_1(\theta) = tan\theta \quad (11)$$

$$G_2(P) = P'^{-1} \quad (12)$$

(initial coefficients of the third-order function:)

$a_0 = -7.0 \times 10^{-4}\ [1/m^2]$

$b_0 = -2.0 \times 10^{-3}\ [1/m]$

$c_0 = 1.0\ [-]$

$d_0 = h_0\ [m]$

where *M* is the percentage of mass delivered (0.1 to 1, or 10 to 100%), *U* is wind velocity, θ is the nozzle pitch angle (in radians), *P* is the discharge pressure (MPa), *Q* is the flow rate (kL/min), *h* is the height of the trajectory at *x*, the distance from the nozzle, and h_0 is the nozzle height. *Q*', *P*', and *U*' are dimensionless quantities of the mass flow, pressure, and wind velocity. The model is formed such that a height for any given distance is calculated in proportion to the variation in the parameters. Figure 4.2 is an example of the model with initial coefficient values for 10° and 15° pitch angles with 60-100% mass percentage delivery. In the trajectory model, 100% mass delivery refers to the furthest distance the spray will reach, which also corresponds to the back edge of the landing zone. An advantage of the model used over other droplet trajectory models is the time it takes to calculate a height given a known distance for any point. Other models consist of partial differential equations which have to be iteratively solved whereas the spreadsheet model only requires one input distance and calculates the height of the spray trajectory at the point given flow rate, angle, and pressure.

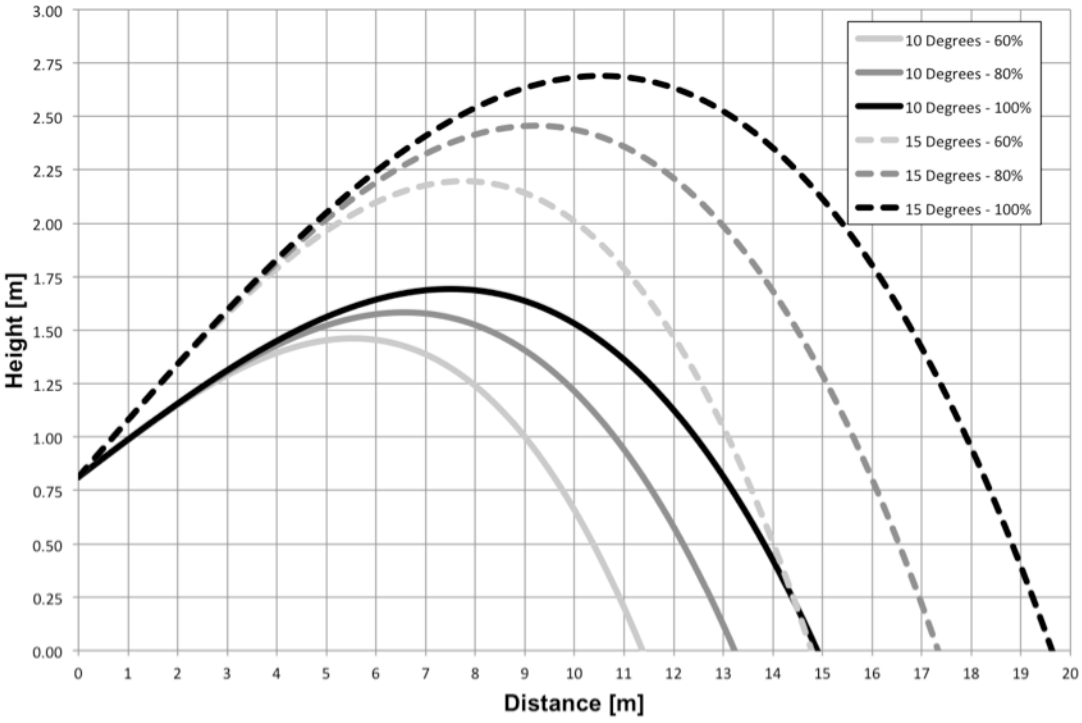

Figure 4.2. Trajectory model with 10° and 15° input angles and 60-100% mass delivery.

4.3 Experiments

To adjust and validate the third-order trajectory model, large-scale water trajectory experiments were performed. Measurements of peak trajectory height, maximum range, footprint, flow rate, and pressure were collected to adjust the model coefficients.

4.3.1 Experiments

An adjustable spray pattern water nozzle was mounted on a yaw-pitch system consisting of two Robotis Dynamixel servomotors. Spray tests were performed at various pitch angles (0°, 5°, 10°, 15°, 20°, 25°) to compare with the model. The flow rate and pressure of the system were kept constant and measured as 0.345 MPa and 0.018 kL/min respectively. The yaw angle was also varied (-10°, -5°, -2.5°, 0°, 2.5°, 5°, 10°) to determine if errors between the yaw angles set by the controller and the observed yaw angles existed. Figure 4.3 contains a top view of the setup used for data collection. Markers were placed along the horizontal direction of the nozzle at 4.5, 6.0 and 7.5 m. Two vertical scales were also used for reference in video analysis of the spray height.

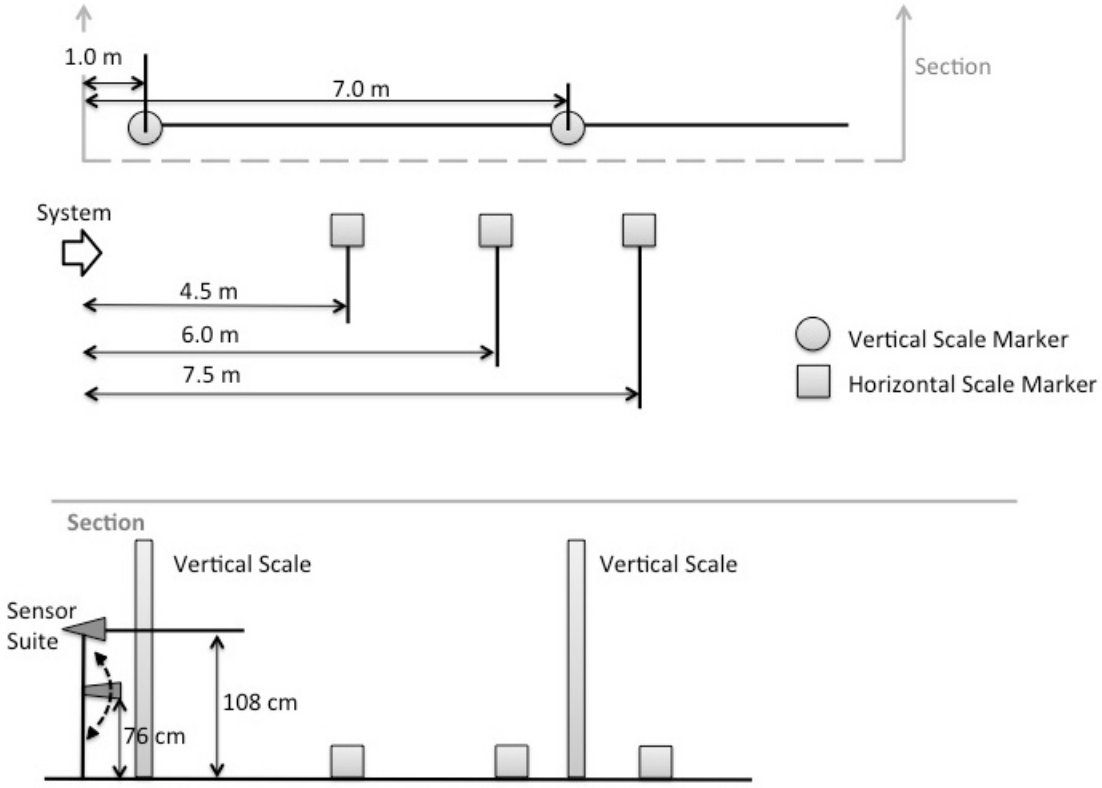

Figure 4.3. Experimental setup for spray data collection.

Video data was collected to measure height and range values at the 2-D side view of the spray. An RGB camera with a resolution of 1080p and frame rate of 30 fps was placed 11 m away from the center of the spray path perpendicular to the IR vision system and nozzle. IR data was taken with two FLIR A35 cameras mounted above the nozzle for water classification and stereo matching for data points of the spray.

To collect data points from the video sets, horizontal and vertical scale lines were overlaid on each frame. The lines were placed in the image at the known horizontal and vertical marker locations. A resolution factor in inches per image pixel was calculated by dividing the known measurement of distance between two adjacent markers and the number of pixels between lines. The height of the spray at each distance as well as the peak of the trajectory was manually observed using the center of spray as a best estimate of the spray path to use in initial adjustment of the nozzle to a targeted fire location. To select the data points, video analysis was performed with lines overlaid and a cursor used to manually select a point while observing a number of frames sequentially to better observe the spray. The uncertainty involved in determining the pixel location

in the video analysis was +/- 1.067 inches. This is determined by using the difference in spray height given the pixel selected is one pixel above or below the actual pixel selected and is the pixel/inch ratio used in overlaying visualization lines. Due to small pressure fluctuations and spray breakup resulting in larger or smaller spray peaks, the variance in the center of the spray as selected manually for any given distance varied approximately +/- 5.33 inches.

The distance, or throw, was observed at the center of the "landing zone" and also physically measured during testing due to the end of the spray not always being distinctly visible in the videos used. The width of the footprint was also measured during collection of the test dataset. Examples of frames from the videos used to collect data points are shown in Figure 4.4 and Figure 4.5. The white horizontal line is representative of the height of the nozzle (0.76 m) and ground level. A yellow vertical scale can be seen at 18 ft along the horizontal axis. The mass distribution of the spray landing zone was determined through water collection at ground level. The largest mass flux at the center of the spray landing zone was between 2.61 and 2.68 kg/m^2-s.

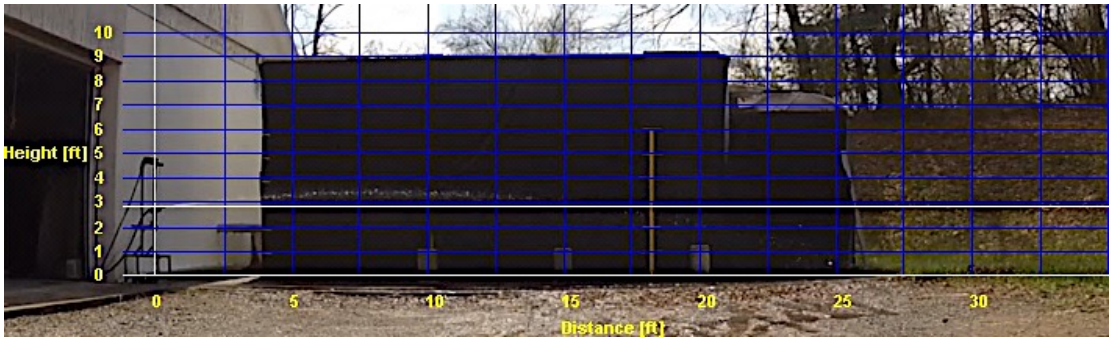

Figure 4.4. Visual camera still of 5° water spray test used for determining data points.

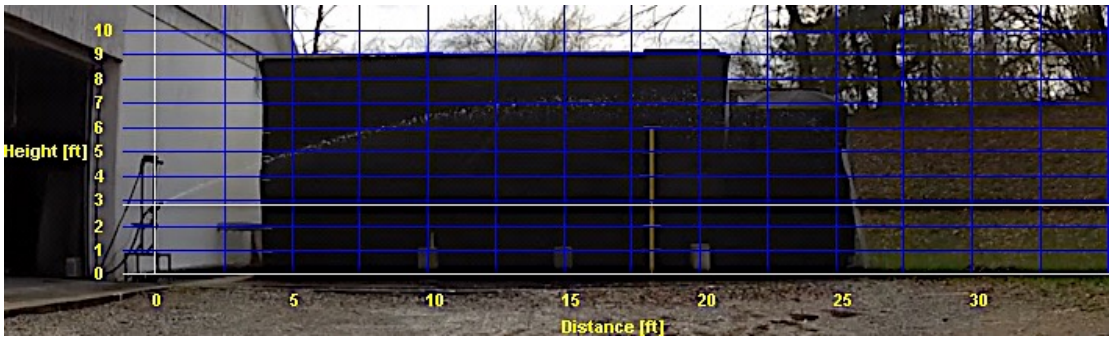

Figure 4.5. Visual camera still of 15° water spray test used for determining data points.

4.3.2 Model Adjustments and Validation

Differences in the model and recorded data were observed due to the large flow rate and pressure differences between the trajectory model as originally proposed by [56] and the experimental values. The difference between 10-90% mass percentage trajectories was adjusted by reducing the variable, n (Eq. 4), from 1.2 to 0.2. For the x^3 term of the function, the mass percentage M is raised to the n-th power as M^n. This adjustment was made due to the lower flow rate of the nozzle used resulting in a much smaller footprint when compared to the larger fire discharge monitor. The coefficient a_o was decreased from -0.0007 to -0.0001 to reduce the effects of the parameters in the x^3 as it is not in the representative values in Eq. 1.

The model as proposed is compared with the measured data points for the nozzle set at 10° in Figure 4.6. The noticeable difference in the models is due to the initial coefficient values that need to be adjusted to better fit the system in use. Data points from video analysis are shown to lie between 10-90% mass delivery in the model with the updated coefficient values.

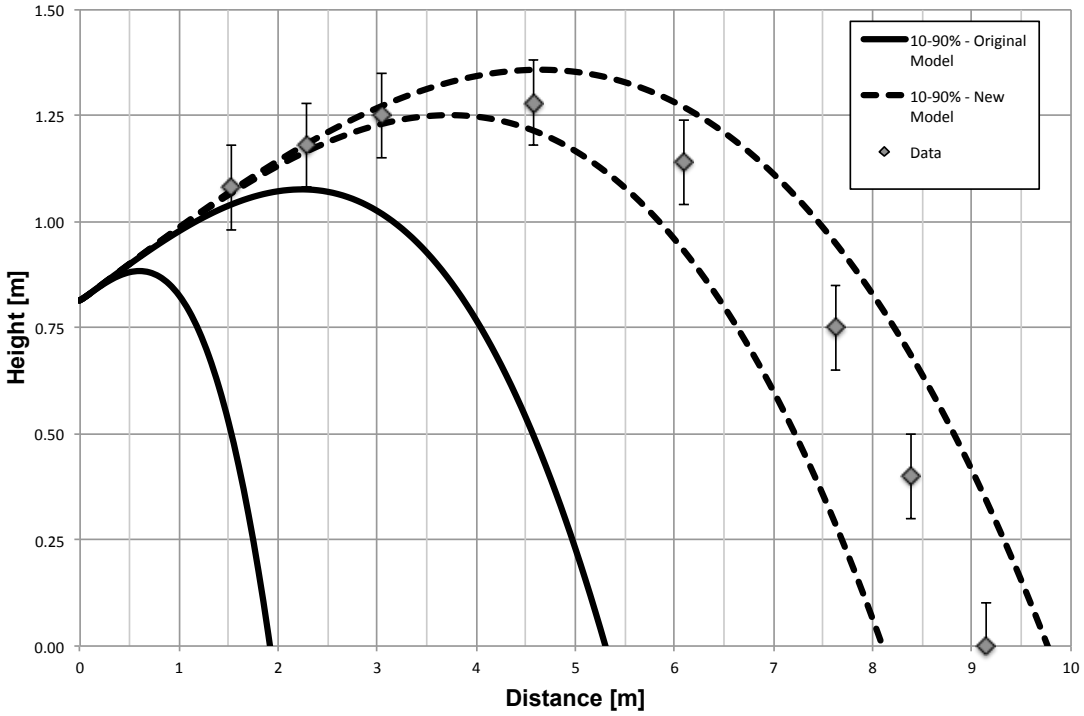

Figure 4.6. Model with original coefficient values for 10° water spray and new model to fit experimental data.

4.4 Spray Localization with IR Stereovision

To correct for errors in nozzle orientation while spraying, data representing points of the spray were taken using the water classification method discussed in Chapter 3. Water was classified and segmented from left and right IR images and an IR stereovision technique calculated disparity values along the spray path.

4.4.1 Water Classification

To generate a pair of binary images for use in stereo-processing, identified non-water objects were ignored and only the classified water regions were used. Pixels associated with the water region were set to 1 while all other pixels were set to a value of 0. To reduce the number of pixels associated with the spray, a linear regression was performed on the segmented images. First, the center column pixel at each row of the water object is used to create an array of row and column points in the image. This reduces the weighting of larger segmented regions with more "water pixels" that will generate inaccurate disparity results. The best fit line represents the center path of the spray as it is the most beneficial in determining the spray pitch and yaw angles. Figure 4.7 contains segmented images for the left and right IR cameras. The blue data points represent the center column at each row of the classified water object. The red line is a best fit through the centered column pixels. The raw IR images are shown at the left of the binary images.

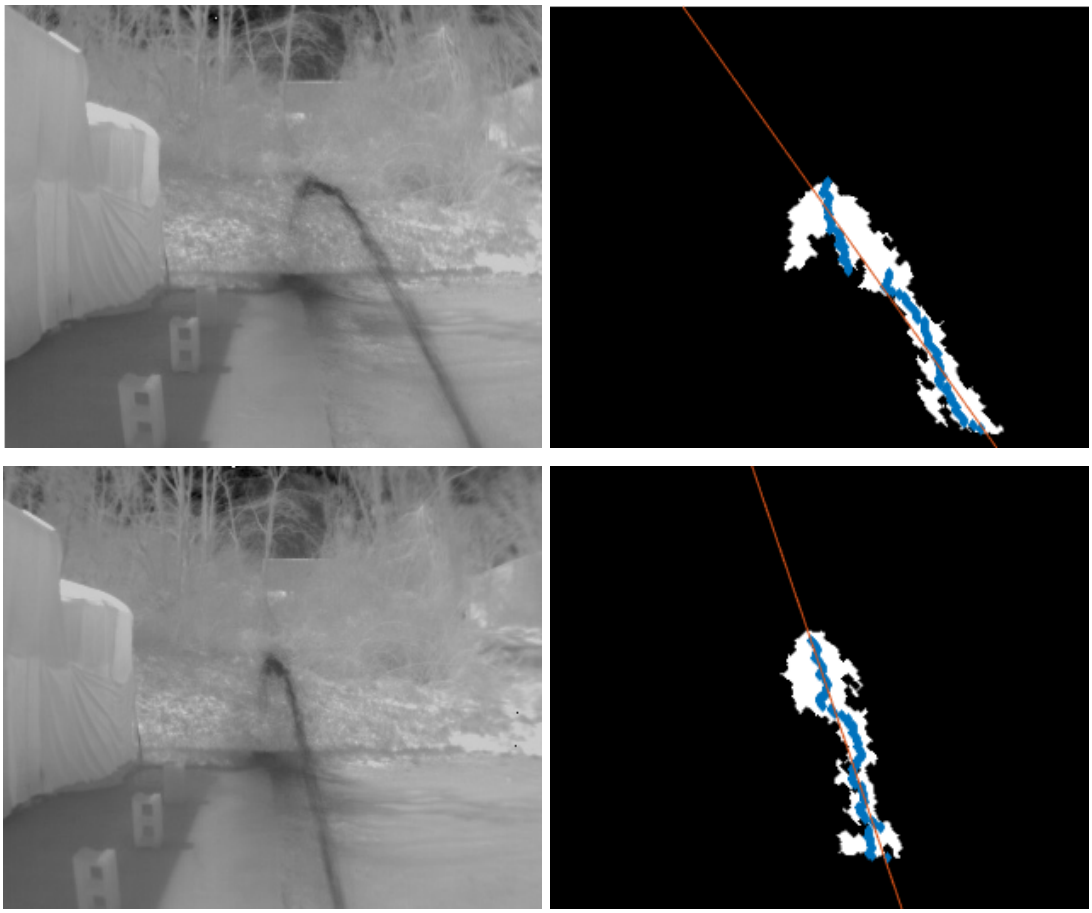

Figure 4.7. Left and right binary images from water classification with best fit line through classified water object.

To reduce the computational time involved in pixel matching over an entire image array for disparity calculations, the binary images in Figure 4.7 were filtered to form an approximation of the centerline spray path. The linear section along the spray length is representative of the general pitch angle. The peak of the spray path would be useful in proper estimation of the pitch angle as it would be another constraint to inversely determine the pitch angle of the trajectory model that reduces the error between the estimated peak and measured peak from image processing. Due to limitations of the FOV and resolution of the cameras, there is a large amount of uncertainty in definitively selecting a pixel location associated with the peak spray height. There are points further and behind the peak that differ only slightly in height and the accuracy of matching a point associated with the peak in stereo processing is reduced due to the distance from the camera plane increasing. The end of the spray, or landing point, could also be included in best fit approximations

but is difficult to properly determine for long range operations due to the spray breakup behavior. Since the density of the spray decreases significantly at these further locations, the segmentation and classification processes used cannot accurately filter out regions associated with the end of the spray and other ROIs due to the blending of water with the background environment. For an input column value, the row value as determined with the best-fit was used to set the image value to 1. The first row of the best-fit line binary images was determined by measuring the first row of the water object in each image. This limits the best fit line to the region as segmented in Figure 4.7. Results from this method are displayed in Figure 4.8. The top row in the binary image is the limiting factor or stopping point of the best fit line extensions of the binary images shown in Figure 4.8.

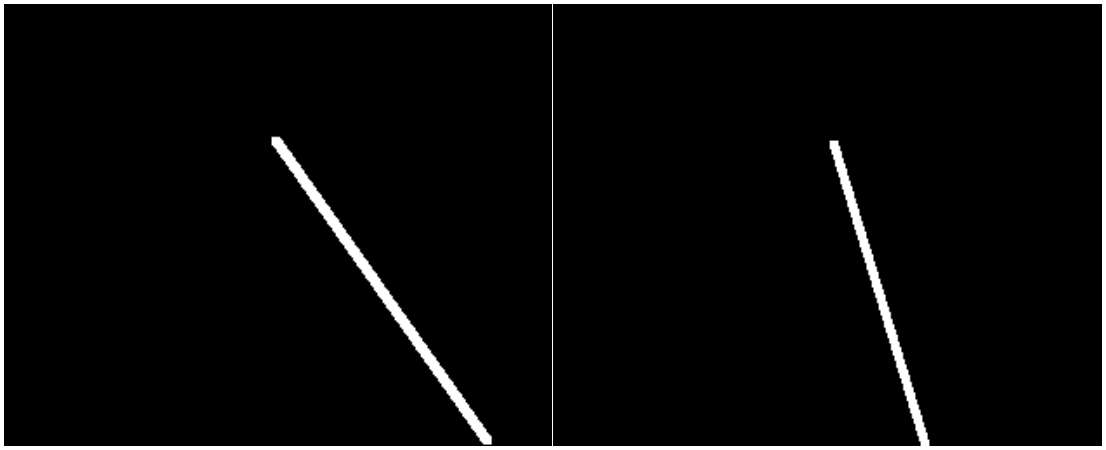

Figure 4.8. Processed left and right binary images used as inputs in stereo-matching.

4.4.2 Disparity Calculations

While stereo-matching algorithms exist to determine which pixel in the right image corresponds to each pixel in the left image by searching a finite grid space, the binary images in Figure 4.8 can be used to simplify stereo-matching and reduce computation time as acquisition time of the IR images is critical for real-time application of autonomous fire suppression systems. For each row of the left binary image, the center of the white line representing the center spray trajectory was used to determine the pixel difference at the same row in the right image through use of the epipolar constraint. This is the basis of a simple stereo system, which is presented in

Figure 4.9. For an epipolar constraint on the stereo-matching the y-coordinate will be same as Eq. 14 and Eq. 16 are equal.

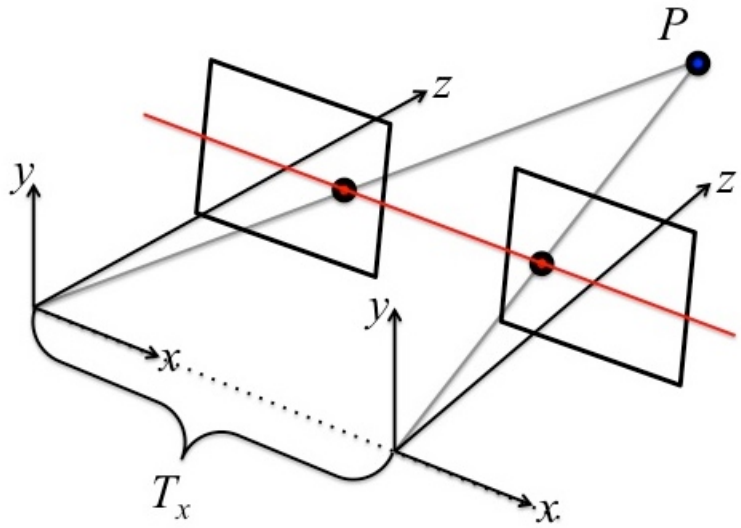

Figure 4.9. Epipolar constraint used in disparity calculation of water best fit line.

$$x_L = f\frac{X}{Z} \tag{13}$$

$$y_L = f\frac{Y}{Z} \tag{14}$$

$$x_R = f\frac{X-T_X}{Z} \tag{15}$$

$$y_R = f\frac{Y}{Z} \tag{16}$$

Before the water has been segmented and classified, the left and right IR images are aligned using a set of image rectification values obtained prior. This process ensures the disparity value is representative of the ground truth distance of an object in view. Objects were placed at known distances from the camera lens with disparity values determined using the baseline of the system (distance between IR cameras) and focal length. The rectification was verified by comparing the resulting disparity values at the object location in the left rectified image. Stationary objects were used as the distance for any given pixel of the water spray is difficult to measure with certainty physically. Figure 4.10 contains the disparity map generated for a water spray object with darker shades of gray representing further distances along the spray path.

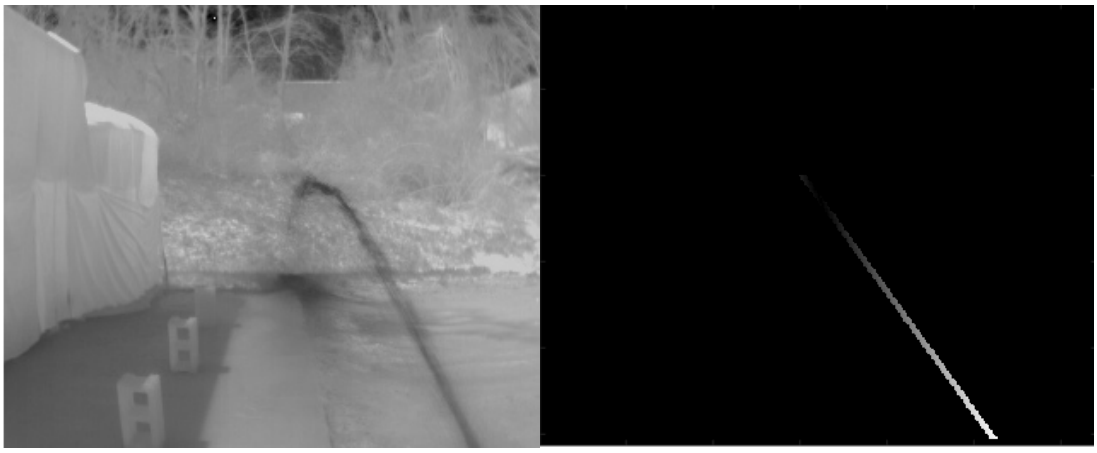

(a) (b)

Figure 4.10. (a) IR image (b) depth image of classified spray object (darker shades of gray represent smaller disparity values/larger distances).

4.5 Spray Error Correction

Errors in the set nozzle angles and the measured spray angles exist due to improper orientation of the nozzle. This will often occur when the robot grabs the nozzle to begin suppression tasks. In addition, slight variations in the flow rate and pressure of the system can influence the spray angle in that lower pressures than the set rate results in a decrease in the throw and peak of the trajectory. To account for these errors, an error correction approach is proposed to fit the trajectory model to a series of data points associated with the water spray as obtained using the IR stereovision system.

4.5.1 Pitch Angle Optimization

Golden Section Search was used to optimize the spray trajectory model to best fit the disparity points of the spray from the vision system. Golden Section Search is a non-linear optimization method for finding the maximum or minimum of a unimodal function by narrowing the range of values inside which the minimum is known to exist. The method maintains the function values for triples of points whose distances form a golden ratio [100, 101]. It is known to be an efficient search method given a good estimate of the initial search interval where a minimum or maximum value is known to lie within and has been used in trajectory optimization of flight paths [115].

In a stereovision system, the disparity values range from 1, 2, 3, … n, which correspond to distance by the relationship between the focal length, disparity, and camera baseline. The distances

associated with each disparity are indexed into an array and input to the Golden Section Search. When disparity between matching pixels is performed, a range of height measurements exists for each disparity integer due to multiple pixel matches in the image being associated with the same distance. In Figure 4.11, the grey markers are data points of the spray from the vision system for a height at a given distance from the nozzle. The dashed line represents the linear best fit through the spray data points. In the correction analysis, the error between heights at a given distance, *d*, as measured with the vision system and the height at the same distance, *d*, in the trajectory model must be minimized.

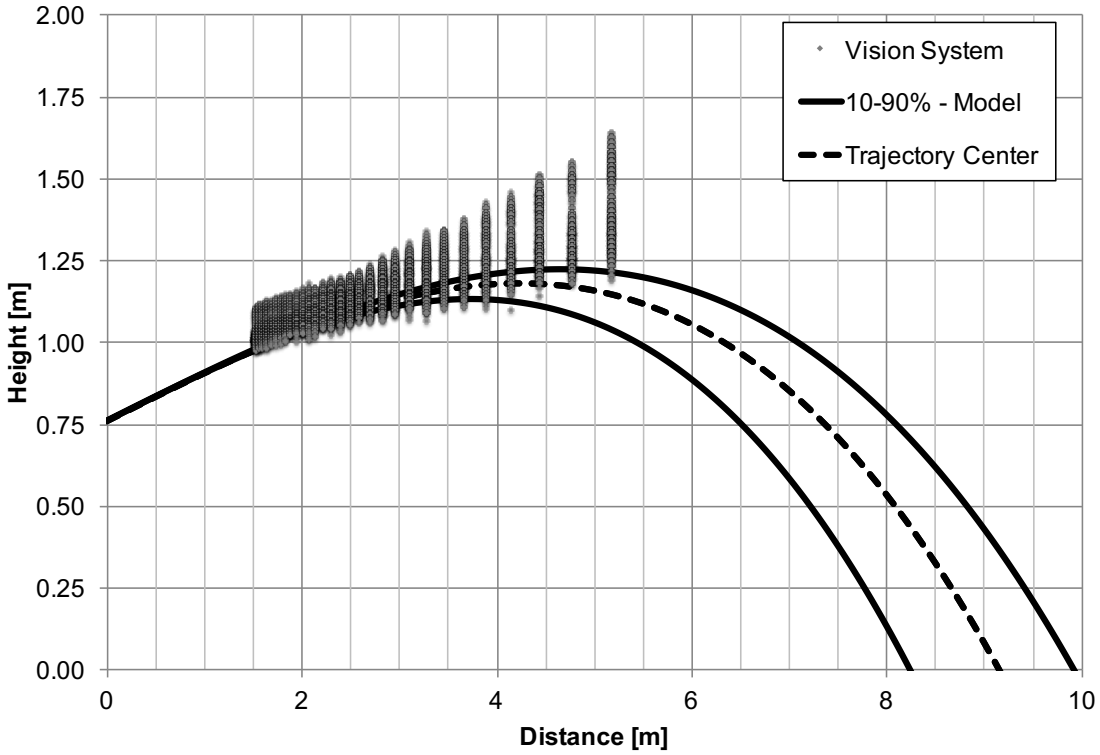

Figure 4.11. Comparison of trajectory model (10-90% water mass) and disparity points from vision system.

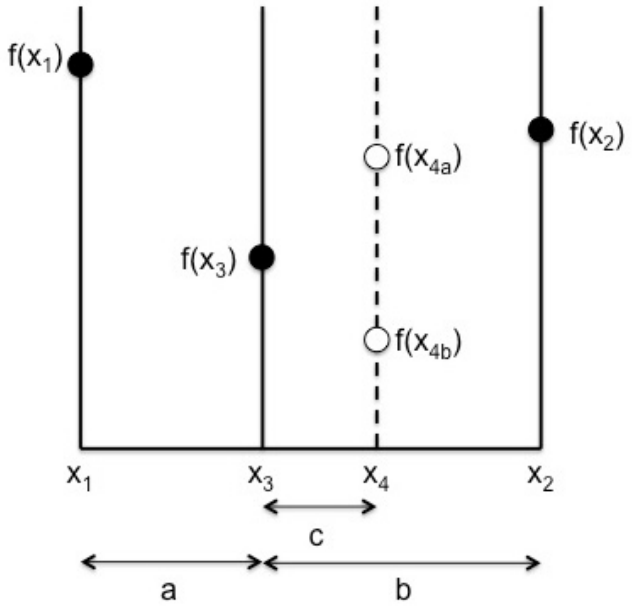

Figure 4.12. Illustration of Golden Section Search at single iteration.

Figure 4.12 illustrates a single iteration in the Golden Section Search for finding a minimum. The value of $f(x)$ is first evaluated at three points: x_1, x_2, x_3. A minimum lies inside the interval since $f(x_3)$ is smaller than both $f(x_1)$ and $f(x_2)$. The function is then evaluated at a fourth point, x_4. If the function yields $f(x_{4a})$, then a minimum lies between x_1 and x_4 and the new triplet of points is x_1, x_3, x_4. If the function yields $f(x_{4b})$, then a minimum lies between x_3 and x_2 and the new triplet of points is x_3, x_4, x_2. The next search is then narrower and guaranteed to contain the minimum value. The new search interval will have a length of $a + c$ or a length of b. The Golden Section Search requires that the two intervals be equal to avoid what is termed a run of "bad luck" which leads to wider intervals being used and slowing the rate of convergence. To ensure equal lengths the method chooses

$$x_3 = x_1 + (x_2 - x_3) \tag{17}$$

To calculate where x_3 is placed, the spacing between these points is chosen such that the same proportion of spacing is used for each new interval. This avoids scenarios where x_3 is placed very close to the edge interval values and the interval width shrinks by the same constant proportion for every iteration, k. If the function yields $f(x_{4a})$ then the proportions should be

$$\frac{c}{a} = \frac{a}{b} \tag{18}$$

and if the function yields $f(x_{4b})$

$$\frac{c}{b-c} = \frac{a}{b} \tag{19}$$

Eliminating c from the two simultaneous equations yields:

$$\left(\frac{b}{a}\right)^2 = \frac{b}{a} + 1 \; or \frac{b}{a} = \varphi \tag{20}$$

where φ is the golden ratio

$$\varphi = \frac{1+\sqrt{5}}{2} = 1.618033988 \ldots$$

The initial search interval is the initial pitch angle +/- 5°.

$$x_1 = \theta_{setpoint} - 5° \tag{21}$$

$$x_2 = \theta_{setpoint} + 5° \tag{22}$$

This assumes the nozzle is within 5° of the set angle. The interval can be increased such that larger errors may be accounted for without increasing the number of iterations significantly. The distance and height of each data point taken from the disparity values are placed in arrays as follows:

$$D_{disp} = [d_1, d_2, d_3, \ldots, d_n] \tag{23}$$

$$H_{disp} = [h_1, h_2, h_3, \ldots, h_n] \tag{24}$$

For a given pitch angle in the equation model, a height at each distance in D_{disp} is calculated as

$$H_M(d_{1-n}) = [h_1, h_2, h_3, \ldots, h_n] \tag{25}$$

and for each distance there exists a residual between the height in the disparity points and the trajectory model

$$D_n = |H_M - H_V| \tag{26}$$

For every iteration in the Golden Section Search, the function is evaluated such that the angle in the interval having the property that the residual sum of squares (RSS)

$$RSS = {D_1}^2 + {D_2}^2 + {D_3}^2 + \cdots + {D_n}^2 \tag{27}$$

is a minimum is used to select the next search interval. Figure 4.13 is an example of the residuals between data points and the trajectory model. The red markers represent points along the spray path generated from the depth map.

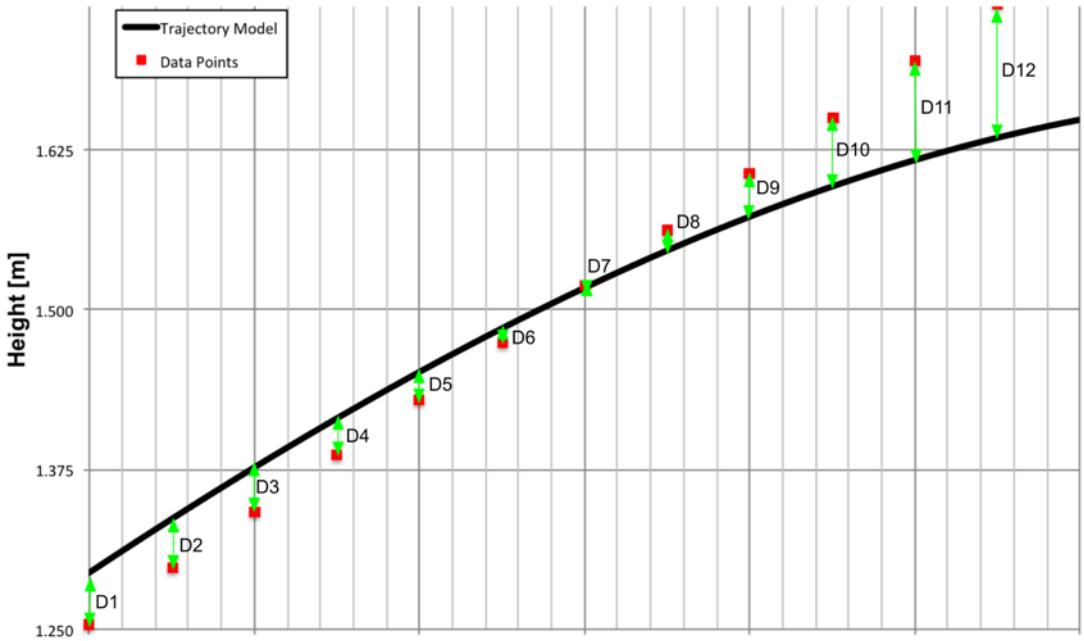

Figure 4.13. Calculation of residuals between trajectory model and data points of water spray.

The RSS between a set of data points taken from a spray test with the nozzle set at 10° and the trajectory model is plotted in Figure 4.14. The dashed line represents where the minimum value (11.2°) for this function exists. The range values and probe points used in the Golden Section Search at each iteration are presented below the RSS plot. The minimum interval length in the search was set as 0.1° so as the interval proportionally shrinks with each iteration, if the interval is less than 0.1° the center value at the convergence interval is used as the observed pitch angle of the system at the current time.

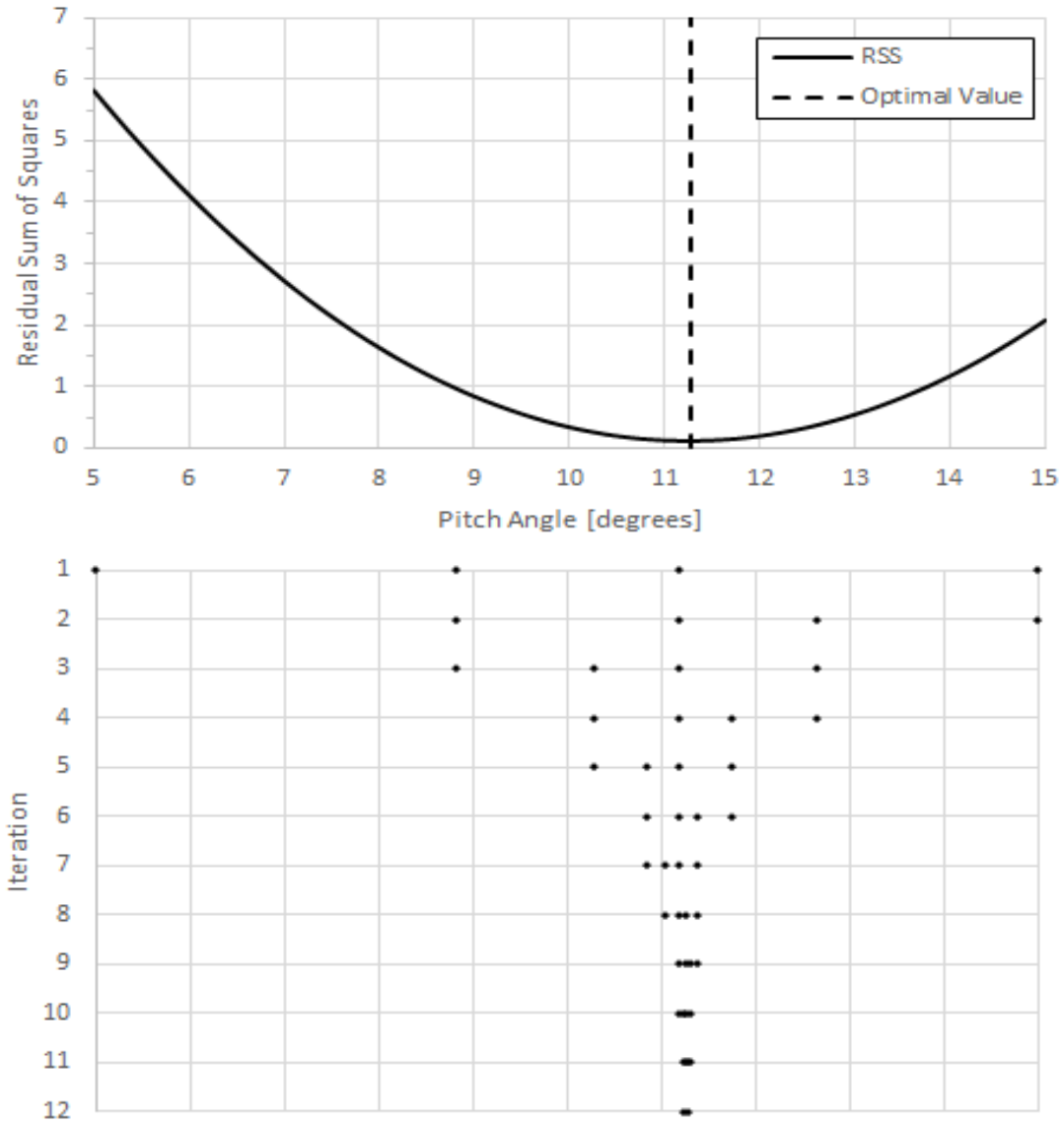

Figure 4.14. Residual sum of squares error used in pitch angle correction using the Golden Section Search.

Table 4.1 contains results from the optimization used for the example in Figure 4.14. Eleven iterations were needed to achieve convergence once the size of the interval (a+b) reaches 0.0813°, less than the 0.1° criteria. The pitch angle was determined to be 11.2557° as the midpoint of the interval at convergence.

Table 4.1. Golden Section Search results for spray optimization.

Iteration (k)	x_1	x_3	x_4	x_2	a+b
1	5.0000°	8.8197°	11.1803°	15.0000°	10.0000°
2	8.8197°	11.1803°	12.6393°	15.0000°	6.1803°
3	8.8197°	10.2786°	11.1803°	12.6393°	3.8197°
4	10.2786°	11.1803°	11.7376°	12.6393°	2.3607°
5	10.2786°	10.8359°	11.1803°	11.7376°	1.4590°
6	10.8359°	11.1803°	11.3932°	11.7376°	0.9017°
7	10.8359°	11.0488°	11.1803°	11.3932°	0.5573°
8	11.0488°	11.1803°	11.2616°	11.3932°	0.3444°
9	11.1803°	11.2616°	11.3119°	11.3932°	0.2129°
10	11.1803°	11.2306°	11.2616°	11.3119°	0.1316°
11	11.2306°	11.2616°	11.2808°	11.3119°	0.0813°

4.5.2 Yaw Angle Optimization

In addition to the pitch angle of the nozzle, the yaw angle must also be corrected. Whereas a trajectory model must be used to predict the spray path for a given distance and height, the yaw angle and spray distance from the center line can be represented as a linear function. To calculate the observed yaw angle of the spray path, the disparity values are transformed to XYZ coordinates. The distance, z, and x-coordinate, which represents how far left or right of the center line of the camera are used. A best fit approach is used to fit a linear projection to the z and x points of the spray. The slope of the line is used as a representation of the actual yaw angle.

4.6 Results

This research consists of the integration of a spray trajectory model and water classification for error correction in an autonomous fire suppression system. Water is classified and segmented from IR images using statistical texture features selected through a Bayesian classification technique. The trajectory model at a predicted pitch and yaw angle was compared with data taken from stereo-processed coordinates of the spray and data points of the spray height from visual video.

4.6.1 Error Correction Results

To determine how well the trajectory model corrects for errors in pitch and yaw angles, data points using the IR vision system are compared with data points from video analysis and the model prediction based on the nozzle being properly oriented. The updated pitch angle of the nozzle is determined by fitting the model to the vision system data points. Results for an initial pitch angle of 0°, 5°, 10°, and 15° are contained in Figure 4.15-Figure 4.18.

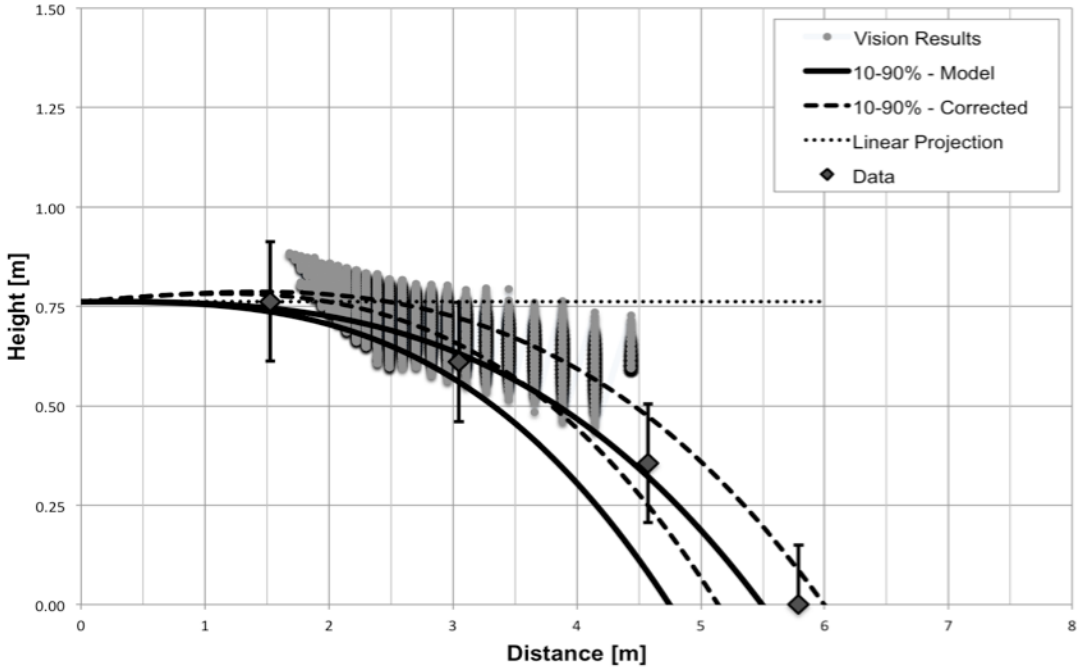

Figure 4.15. 0° water trajectory test with corrected pitch angle with disparity values.

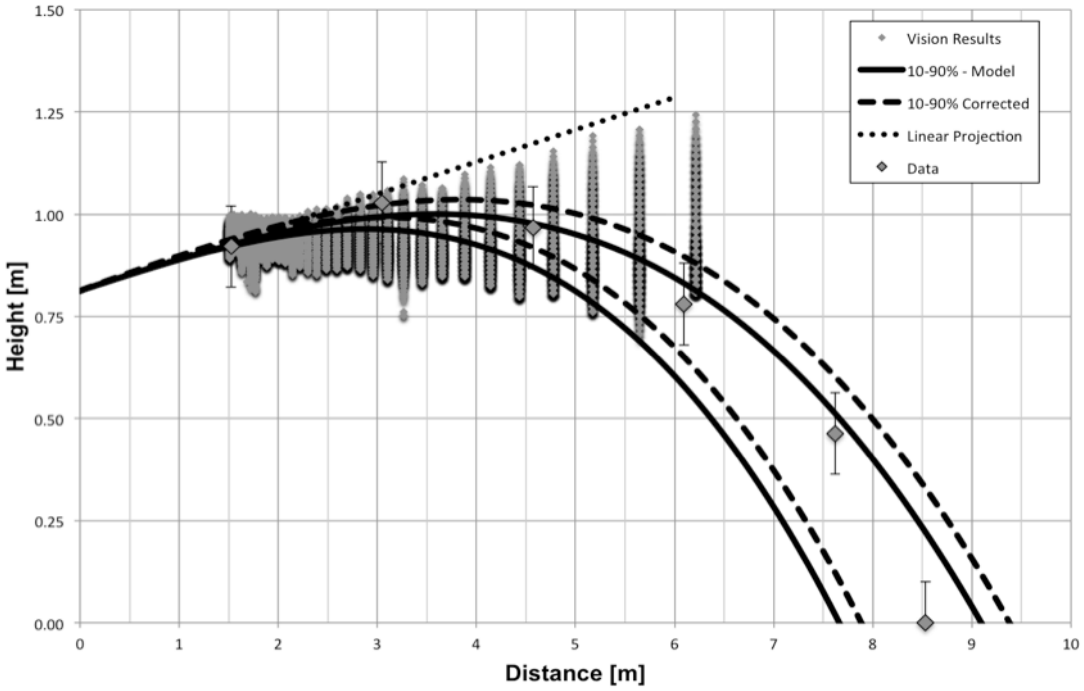

Figure 4.16. 5° water trajectory test with corrected pitch angle with disparity values.

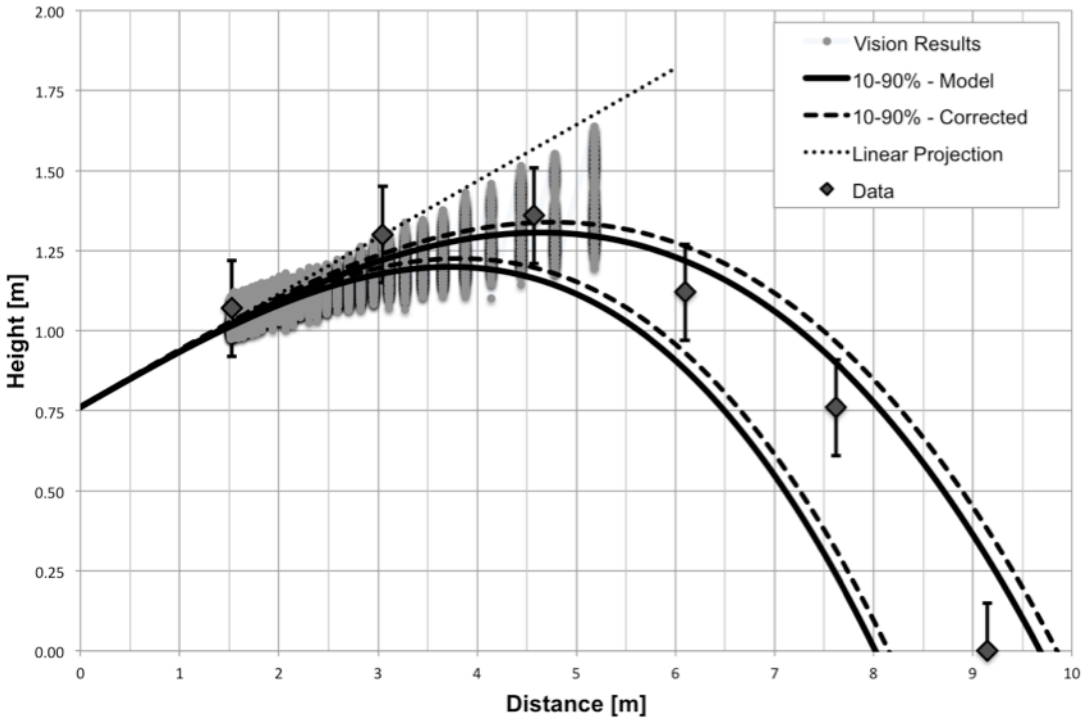

Figure 4.17. 10° water trajectory test with corrected pitch angle with disparity values.

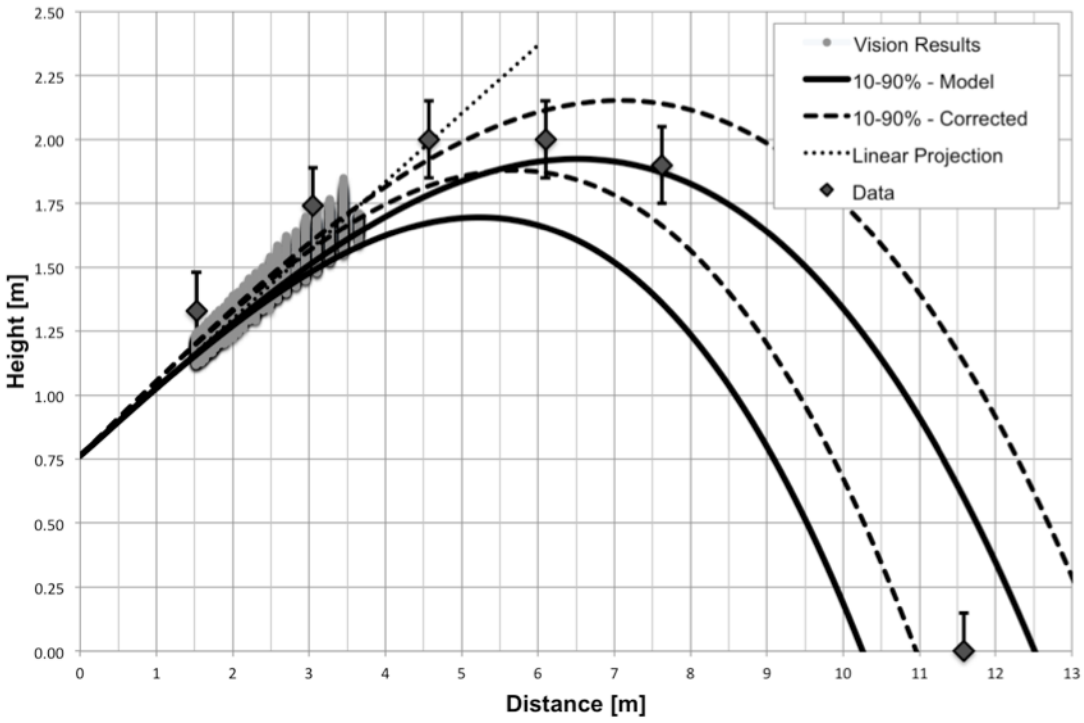

Figure 4.18. 15° water trajectory test with corrected pitch angle with disparity values.

Figure 4.15-Figure 4.18 indicate that the nozzle has a downward bias due to the pitch angle estimate being larger than the set pitch angle. The corrected trajectory also encompasses data points obtained through video analysis and the IR vision system with water classification and stereo processing results. In many firefighting scenarios, slight errors (<1°) will not affect the spray effectively reaching at least a portion of the targeted fire due to the width of the spray pattern used. This is also dependent on the effective reach of the spray because fires further away from the nozzle require better estimation of the spray direction. If the nozzle is offset such that the water does not reach any part of the fire, the calculated error can be used to adjust the attack angle. Figure 4.19 contains results of the yaw angle correction. The off-center distance values are left of the centerline for the initial yaw angle, 0°. The corrected angle was determined to be +0.9° placing the observed spray direction slightly to left of center. A limitation with the trajectory model used is the effect of wind on the yaw direction of the spray path. As formulated, the effect of wind is only taken as a magnitude and direction either backing the spray or as an adverse wind. To account of shifts in the yaw direction of the spray, additional information would be necessary such as the landing point of the spray localized with respect to the nozzle. This landing location could be used

with the additional information of the closer proximity portion of the spray to best fit a higher order function since a crosswind may have a larger effect on the back portion of the spray only.

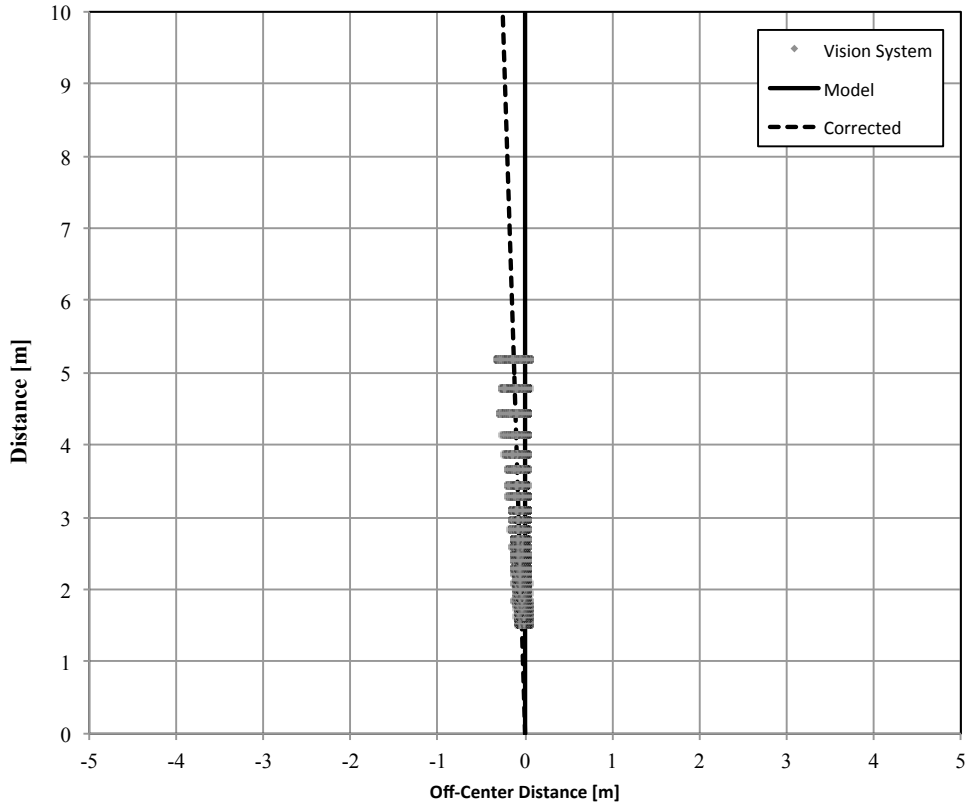

Figure 4.19. 0° yaw angle test with corrected yaw angle with disparity values.

IR videos from 11 tests were used to develop and analyze the method of pitch and yaw angle estimation. Results from 11 tests are contained in Table 4.2. The yaw and pitch setpoint angles are those initially set by the motor controller. The corrected angles were determined using the Golden Section Search optimization technique. The number of iterations for convergence fell between 11 and 12 for the given initial interval range of 10°. For the nozzle configuration used, small discrepancies (< 1.5°) between set and estimate angles were calculated.

Table 4.2. Golden Section Search results for spray optimization.

	Setpoint Angles		Corrected Angles		
Test	Yaw	Pitch	Yaw	Pitch	Iterations
1	0.0°	0.0°	1.21°	1.54°	11
2	0.0°	5.0°	1.47°	5.87°	11
3	0.0°	10.0°	1.65°	10.29°	12
4	0.0°	15.0°	0.96°	16.33°	11
5	0.0°	20.0°	1.49°	21.54°	12
6	-2.5°	10.0°	-1.16°	9.17°	12
7	-5.0°	10.0°	-3.96°	8.57°	12
8	-10.0°	10.0°	-8.20°	10.14°	11
9	+2.5°	10.0°	+3.33°	8.33°	12
10	+5.0°	10.0°	+5.80°	8.74°	11
11	+10.0°	10.0°	+10.63°	8.64°	12

4.7 Conclusions

This chapter presents a method of predicting yaw and pitch angles of water spray using an IR vision system and trajectory model for use in error correction in an autonomous fire suppression algorithm. A model for water discharge trajectory, based on simulated models for water sprays, was adjusted to fit the nozzle parameters used in this work. Flow rate and discharge pressure were both lower values than reported in the previous model. Flow rate, pressure, angle, wind velocity, and mass delivery percentage were used to predict the spray height for any given distance from the nozzle. A comparison was provided between data points taken from video analysis of water spray at various pitch angles and data points along the spray path from an IR vision system. The data points are calculated by using a Bayesian water classification method to segment water from IR images and stereo processing a binarized pair of images of the spray to determine the distance and height of a pixel in the images.

A Golden Section Search technique was used to optimize the pitch angle to fit the trajectory model and data points from the IR vision system due to its accuracy and speed for real-time implementation. The error between the linear best fit of the disparity points and the trajectory model is used to determine the RSS at each input pitch angle. The search technique finds the local minimum of the unimodal function until convergence is achieved and the optimal pitch angle is determined. Yaw estimation is also calculated using a linear best fit of x-z spray coordinates. The results from this section will be used within an autonomous fire suppression algorithm to correct the yaw and pitch angle of a nozzle in real-time.

5 Autonomous Fire Suppression System with Real-Time Feedback Based Decision Tree Controller

5.1 Abstract

A computer vision-based autonomous fire suppression system with real-time feedback of fire size and spray direction is presented in this paper. The system has been developed for use in a firefighting robot for close-range, localized fire suppression tasks in enclosed environments. A probabilistic water classification method was developed for segmenting water spray in a pair of IR cameras. Stereo processing was performed to localize points along the spray path for use in yaw and pitch angle estimation. A Golden Section Search with linear least squares optimization was used to determine the optimal pitch angle of the spray position at each sampling time. Kalman filtering was used to remove noise from the angle measurements and obtain a better estimate of the current nozzle orientation. A decision tree was used to determine the correct nozzle positioning mode using image feedback to suppress the fire and accounts for errors in direction, fire size during suppression, and when to adjust the nozzle based on IR feedback. Through implementation of a PI controller, the system is able to correct for unknown disturbances causing erroneous targeting of a localized fire. Experiments are presented with the initial nozzle angled correctly and with forced offsets in the system to set the initial spray position incorrectly in order for the system to correct. Suppression times ranged from 7.2 to 16.3 s with a standard deviation of 3.86 s and average time of 11.15 s. A total of 12 tests demonstrated performance of the system given a forced offset to the initial nozzle orientation resulting in an error between the spray location and the fire target. Suppression times ranged from 8.1 to 27.9 s with a mean of 16.93 s and standard deviation of 6.24 s. The proposed system can be implemented on a robotic firefighting platform to autonomously detect a fire, choose a proper manipulation goal and suppress full scale fires given disturbances causing erroneous targeting.

5.2 Introduction

Intelligent firefighting robots are an area of active research to reduce firefighter injuries and deaths. Autonomous systems may also increase the effectiveness of firefighting tasks through

advanced vision systems and image feedback support in low visibility environments. Frequently, the damage resulting from inefficient application of water will exceed damage done by the fire to property and other valuables. Current firefighting robots developed are remotely controlled by operators in indoor and outdoor environments [10, 17, 27-30]. The shipboard autonomous firefighting robot (SAFFIR) has been developed as a support tool in located and suppressing fires inside ships and structures. An autonomous fire suppression algorithm must be developed for use on a humanoid robotic platform to efficiently manipulate a nozzle for suppression and make intelligent decisions on suppressant placement based on observations made in the environment.

Several methods have been proposed for identifying fire and smoke using image processing techniques but the number of automated fire suppression systems demonstrated are limited or conceptual [31, 102-104]. Recently, automatic jet fire extinguishing systems based on infrared (IR) vision have been developed and used in firefighting operations [105]. Robotic fire monitors use computer vision techniques to detect and suppress fires but real-time error correction in these systems has not been implemented for scenarios involving wind or slippage of the nozzle causing motor bias. Chen et al [19] developed an automatic fire searching and suppression system with remote controlled fire monitors and a fire search method using a single CCD camera fixed to move in parallel with the fire monitor nozzle. The total response times of water cannons, fire scanning, and accuracy of targeting are an area that can be improved [20]. The integration of fire detection using video surveillance techniques and suppression has been presented in [32] and [103] but rely on visual cues for fire detection and do not present control design for improper targeting of the spray. In order to identify the area in the FOV where the spray is located, a probabilistic water classification method was used. The advantage of assessing the water spray direction in a suppression system is the ability to correct the spray path for errors in targeting due to pressure and flow rate losses, and bias in the motor position or nozzle mount. Automatic fire suppression systems often included assumptions about the spray trajectory based on linear projection or prior experiments to set bias angles for various fire distances [106]. An intelligent suppression system must integrate a number of different subsystems including: fire detection, fire localization, spray identification and localization, trajectory modeling, closed-loop control of spray direction, and nozzle manipulation based on fire feedback control.

The proposed autonomous fire suppression system was developed using two IR cameras as a fire detector and in stereo for localization. An initial nozzle position is determined through use

of fire coordinates from the IR stereovision system and a spray trajectory model for prediction of the spray path. The spray is segmented in the vision system using a probabilistic classification method to measure the current spray yaw and pitch angles. The error between the desired nozzle angles and observed values are used with a PI controller to adjust the nozzle in real-time using a decision tree control scheme for fire suppression. The system was demonstrated in various scenarios including indoor and outdoor operation with forced offsets to the initial nozzle position.

5.3 System Architecture

The vision system consists of two FLIR A35 long wavelength IR (7-14 μm) cameras capable of imaging through zero visibility environments and a visual camera. An adjustable spray pattern nozzle was mounted on a pair of ROBOTIS Dynamixel servomotors that are controlled using the suppression algorithm to manipulate the nozzle.

5.3.1 Control Overview

The control flow chart for the autonomous suppression system is presented in Figure 5.1. The IR cameras are used to detect the presence of a fire in the FOV of the system. The fire is kept in the FOV from the beginning of all tests to eliminate the need to move the cameras or scan the area. Previous work [21, 55] has been developed to use smoke and fire probabilistic classification methods to identify a heading direction to help the robotic platform move toward a possible fire. In a standalone system, the cameras would continuously scan the area for fire or begin searching the space once an externally placed fire detector (i.e. fire alarm) indicates the presence of a fire in the space. In large spaces, reliance on external fire detectors will reduce response times due to proximity of the sensors to the fire location.

Once a fire has been identified, a target is selected corresponding to the center base of the fire. The pixel location of the target is used with a disparity map generated from the IR stereovision system to calculate a 3D coordinate position relative to the imaging plane with the left IR camera as the reference origin. Given knowledge of the pressure and flow rate of the system, a spray trajectory model is used to predict the yaw and pitch angle to initially set the nozzle. Due to a number of factors, the initial nozzle setting may result in inaccurate targeting of the spray onto the fire. Errors can be related to the nozzle not being properly set in the robot hand or mounted system

or shifting during firefighting operations. Fluctuation in pressure and flow rate will also disturb the system resulting in erroneous pitch angles as the model is fit with constant pressure and flow rate. For testing response of the system, an external disturbance was introduced at the initialization step in the flow diagram to force the nozzle to be offset from the desired initial angles.

Once the valve is opened, a feedback loop continuously monitors the presence of the fire. A decision tree approach is used to make intelligent decisions on how to manipulate the nozzle to efficiently and accurately aim the spray onto the fire until fully suppressed. The decision tree was developed through large-scale experiments performed with water as a suppressant and wood-crib fires.

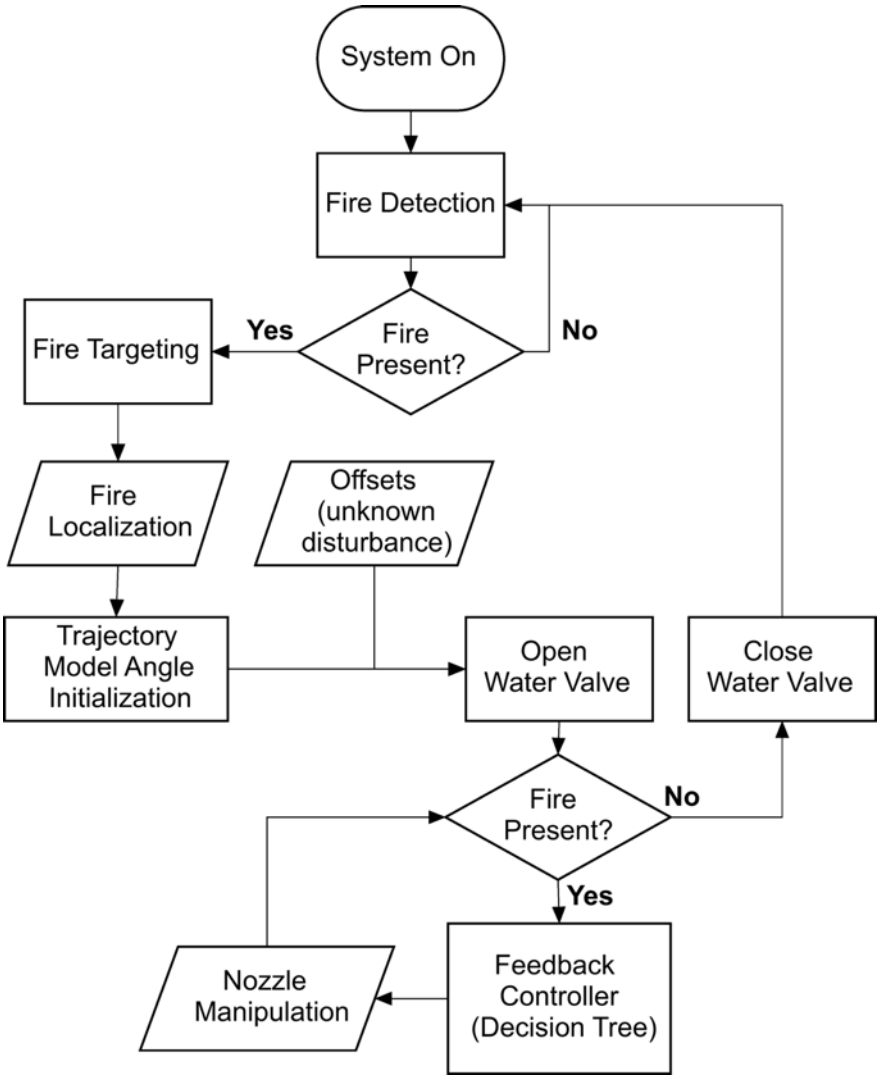

Figure 5.1. Suppression algorithm general flow chart

5.4 Sub-Systems

The system consists of a series of image processing based sub-systems for closed-loop control including: fire localization, water classification, trajectory modeling, spray localization, pitch and yaw angle estimation, PI control, and visual servoing control.

5.4.1 Fire Localization

The IR cameras use an uncooled VOX microbolometer outputting 14-bit data with a 320 x 256-pixel focal plane array and a frame rate of 10 Hz. The small form factor (106 x 40 x 43 mm) and weight (0.2 kg) makes them ideal for use on a robotic platform to limit payload. RGB cameras for fire or smoke detection have been widely used but the methods [35, 38, 107-110] do not apply to firefighting robots due to high false positive rates from color variations or reflections. Handheld thermal cameras are typically used to aid firefighting operations in smoke-filled environments [39-42] so are recommended for indoor firefighting tasks.

Fire is higher in temperature (and image intensity) than the background, making intensity a useful characteristic in segmenting the fire from a thermal image. For implementation in a real-time system, a mean intensity threshold was used for segmenting fire from the IR images along with a variance threshold. Reliance on intensity as the only segmentation criteria will result in multiple objects possibly being detected in the scene such as reflections or other objects that are at an increased temperature. Use of other features such as second-order textures, contours, or temporal features can be used in addition to intensity to remove false positives from being perceived to be fire and erroneously targeted by the system. A proposed technique that uses IR cameras with clustering-based image auto-thresholding showed accurate results in classifying fire, fire reflections, smoke, and smoke reflections [55]. In the study, variance was considered as a classifying feature and showed the highest difference in the probability density functions over smoke, reflections, and hot objects. The variance metric is taken by analyzing all intensity values of an object that is segmented using the intensity threshold at the first stage of fire detection. The probability distributions of the first-order feature variance for smoke, fire, and reflections are illustrated in Figure 5.2 showing fire has a clear separation between other high intensity regions due to smoke and reflections from the fire itself.

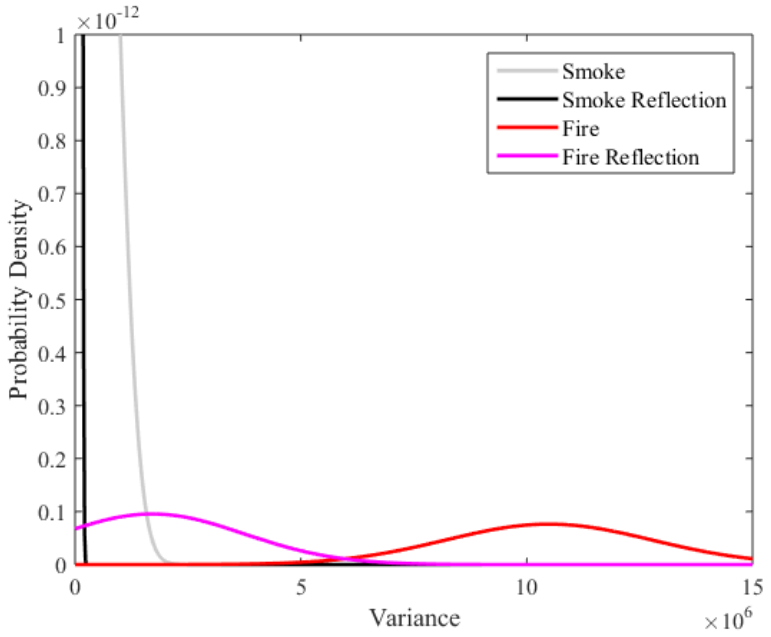

Figure 5.2. Variance probability density distribution of fire, smoke, and reflections.

Fire reflections and hot objects in the test setups were smaller in size compared to the fire but can also be cooled after fire suppression if they are still at a high intensity above the threshold value. Potential fire pixels were segmented using Eq. 1

$$I_R(x_i,\ y_i) \geq K_I\ \cup\ Variance\left(IR_{object}\right) \geq K_V \qquad (1)$$

where $\boldsymbol{I_R}(x_i,\ y_i)$ is the IR intensity at image location x, y and K_I is a threshold value. Intensities above K_I are defined as possible fire and values below K_I are set to zero to create a masked image. The temperature range of the cameras when used in low gain is -40°C to +550°C forming an intensity range from -16,384 to -1. A threshold (K_I) of 300°C was used to classify fire pixels within view of the camera based on prior experiments performed in the low visibility and clear conditions used in the suppression tests. The intensity threshold resulted in little to no reflections from the fire and provided a clear segmentation of the fire in the IR image but may lead to larger reflections detectable as fire in different fire environments. An additional threshold was applied for the variance of each object segmented with intensity, K_V. Previously collected data of segmented fire, fire reflections, smoke, and smoke reflections in IR was used to determine the variance threshold. The mean variance threshold was set as two standard variations below the mean variance of fire objects in the dataset since the variance of fire is clearly distinguishable from reflections and other hot objects.

Processing is performed to optimize image contrast and brightness based on the minimum and maximum pixel intensity values. Fire pixels are segmented and highlighted in red to use in the user display. For a single fire scenario, the last or bottom row associated with the fire object is chosen as the targeted image row location $I_R(x_i)$ and the left and right edges of the object are averaged to identify the center column of the fire $I_R(y_i)$.

The three-dimensional coordinates of the base of the fire must be used to plan for the application of suppressant onto the fire. Commercial autonomous systems rely on a single camera and nozzle being rigidly mounted together [19]. The system then attempts to estimate a distance for the fire based on the amount the target of the fire moves in consecutive images for a small change in the camera angle. For the system developed in this paper, the imaging is separate from the nozzle manipulator to show the potential application for robotic firefighting. The IR pair is rectified to simplify the correspondence problem in identifying matching points between the images by removing optical distortion. For single camera systems, the size of the fire could alter what distance is estimated as the fire may be located at the same position within a 2D image if it is large and further away or smaller and closer to the camera. The IR stereo system has been shown to predict distances of objects within 3 m of the system to within 9.3% in clear conditions as well as in smoke filled conditions when the visibility is less than 1 m [24]. As the distance from the camera lens increases, the uncertainty in the measurement will decrease in stereo vision systems as the relative distance between corresponding pixels decreases.

5.4.2 Water Classification

A three frame differencing method was proposed as a method to segment possible water objects in IR. It makes use of the high variance of intensity of water pixels between consecutive frames. A probabilistic classification technique identified possible second order texture features that could be used to classify water from non-water objects. Twelve textural features were collected using a gray level co-occurrence matrix (GLCM) of segmented objects. The classification error for each combination of all features was collected in order to select the combination with the lowest error using two methods, re-substitution and cross-validation error. The training dataset of 11 videos with 11,765 frames and 44,588 candidates was used to train the water classifier. The test dataset used to evaluate the algorithm consisted of 6 videos with 9,203

frames and 20,793 candidates. The scenes used included outdoor water spray with and without fire in view, indoor water spray in high and low visibility environments, and room temperature water leaks. An example of the results of water classification are shown in Figure 5.3.

The fire localization step creates a mask to remove hot objects, smoke, reflections, and fire from being segmented as possible water objects. For high ceiling storage areas with higher pressure systems, water classification may be applicable as a way of determining where the spray is landing on the ground surface. Due to the camera resolution and lower pressure used in the system, the end of the spray is not always distinguishable. The linear portion of the spray trajectory and arc of the throw were segmented and used to determine an approximate nozzle pitch and yaw at any time step.

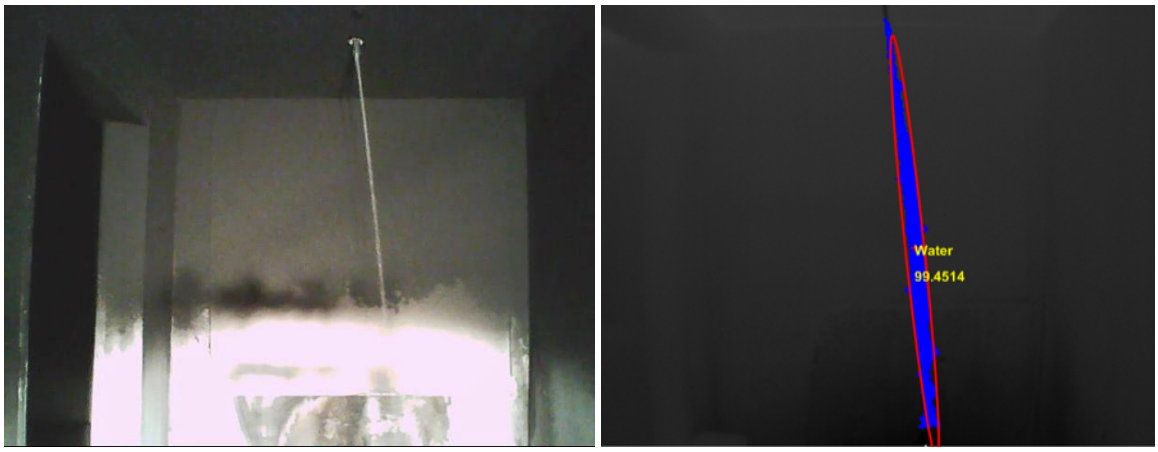

Figure 5.3. Visual image capture of water stream and IR water classification.

5.4.3 Trajectory Modeling

In order to predict the path of the water spray, a trajectory model previously developed was adjusted to fit validation data of the spray used in the current system at a known pressure and flow rate. The model was used to predict a height approximation of the spray for any distance. It was also used to set a desired yaw and pitch angle of the nozzle given the 3D fire coordinates obtained through localization. The error between the height of the spray at the fire distance was minimized to find the optimal pitch angle.

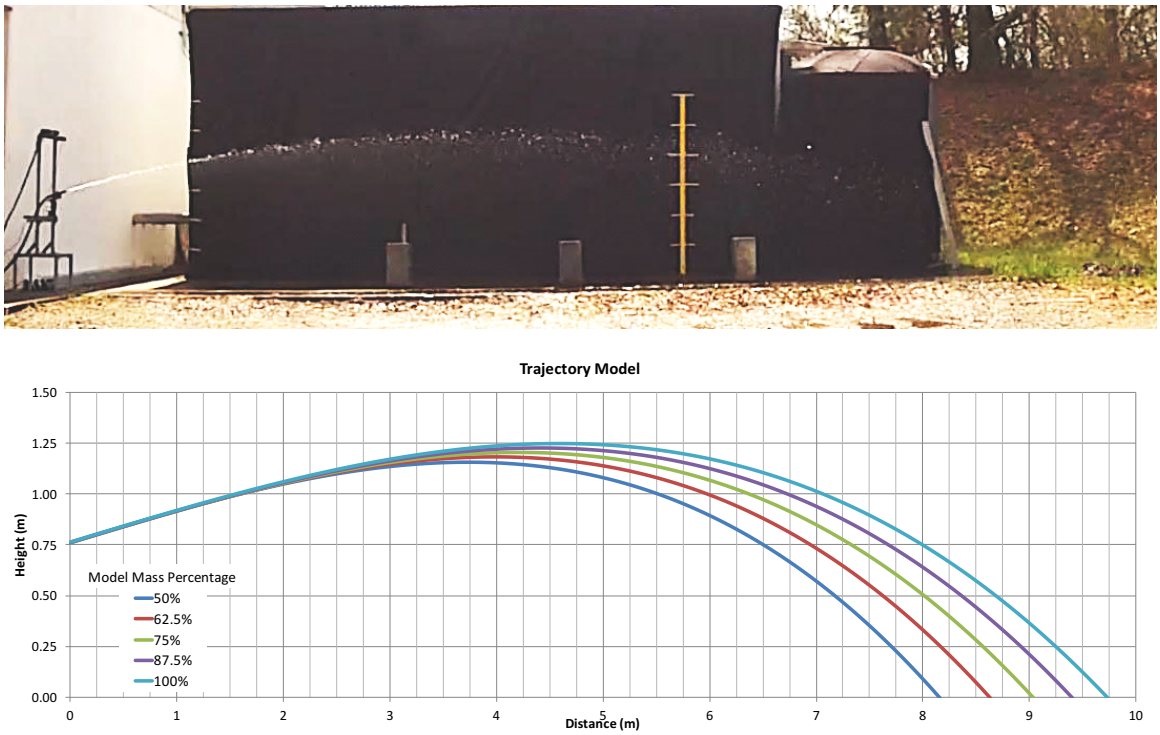

Figure 5.4. Side view of spray trajectory and model for pitch angle = 10°.

5.4.4 Spray Localization

The trajectory model was used with water classification to localize points along the spray path for a real-time estimate of the current position. Once the spray was classified in the left and right IR image, an estimation of the center of the spray was calculated through use of a linear regression. An example is shown in Figure 5.5 with the red line representing the center spray path.

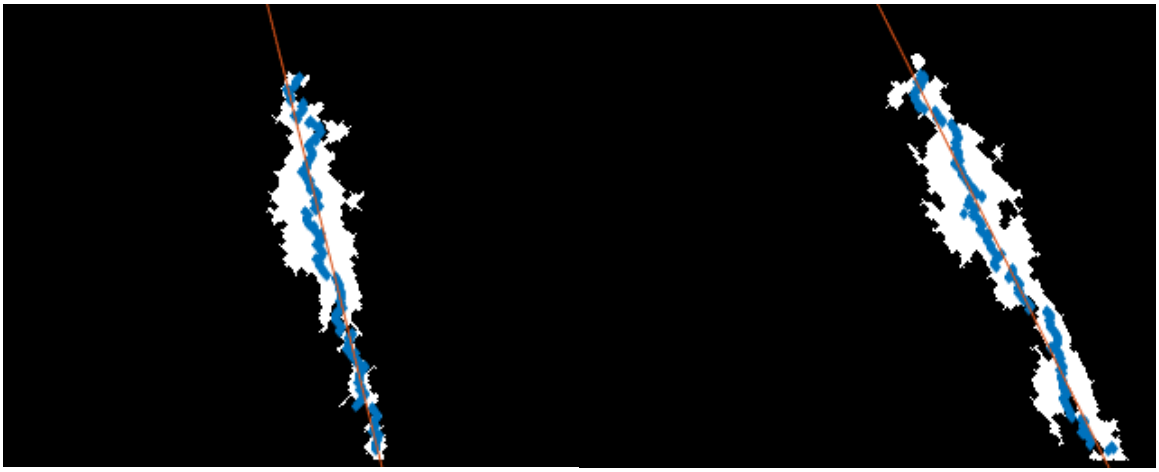

Figure 5.5. Left and right image of water classification with centerline estimation.

Using an epipolar constraint, disparity values between the left and right centerline spray were used to create a disparity map as shown in Figure 5.6(b). From the disparity map, an array of 3D points along the spray path are generated for use in determining the current yaw and pitch angle.

Figure 5.6. (a) Visual image of water spray (b) disparity map of water spray using IR stereo pair.

5.4.5 Angle Estimation

A golden-section search method was used to optimize the trajectory model to the spray estimate obtained in the localization process. A Golden Section Search seeks to find the local minimum or maximum of a unimodal function by narrowing the range of values inside which the extremum is located. Values for a triplet of points is maintained by using the golden ratio to select distances. The probe points correspond to angles as input to the trajectory model and the error is the RMS of the residuals of depth points of the spray and the height at the same distance within the model. An example of a Golden Section Search optimization for localized spray points is shown in Figure 5.7. The setpoint for the model was 5° and an optimal angle of 9.79° is determined to fit the 3D spray points represented by the blue data points.

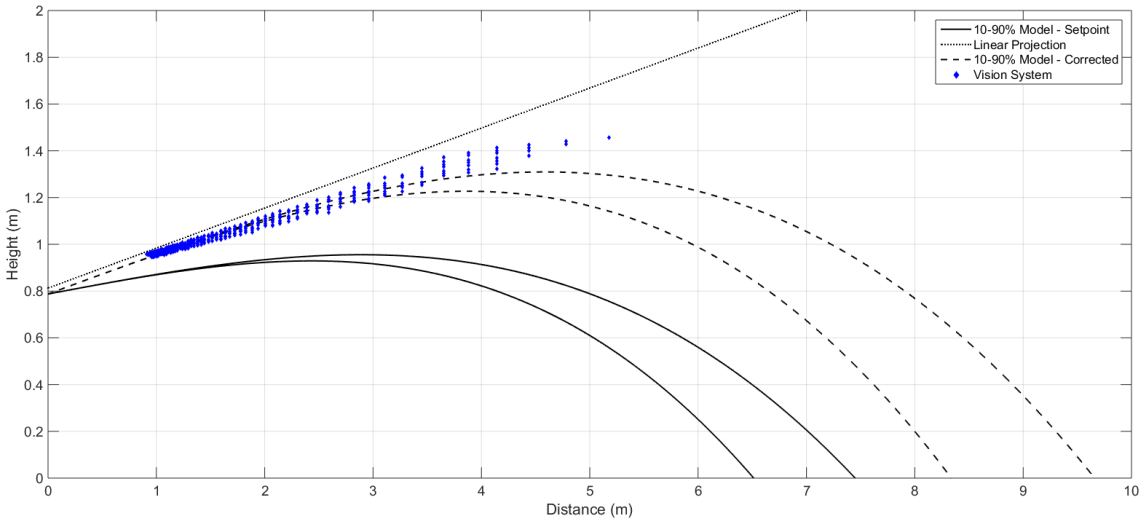

Figure 5.7. Pitch angle optimization using Golden Section Search.

5.4.6 Nozzle Controller

Kalman Filtering

The observed angle measurements result in a large amount of noise due to a number of factors including camera resolution, uncertainty in disparity calculations, segmentation accuracy of the water spray, flow rate and pressure changes, and motor motion. To account for this noise and estimate the pitch and yaw angle of the spray for any given time, a Kalman Filter was implemented. For estimation of a single variable, the state equations of the classical Kalman filter can be ignored resulting in the general form:

Current Estimation — Measured Value

$$\hat{X}_k = K_k \cdot Z_k + (1 - K_k) \cdot \hat{X}_{k-1} \tag{2}$$

Kalman Gain — Previous Estimation

where k represents the state or discrete time interval, $\hat{X}_k$ is the current estimation, K is the Kalman gain, Z is the measured value and $\hat{X}_{k-1}$ is the previous estimation. The purpose of the Kalman Filter is to find the current estimate $\hat{X}_k$, of the signal, measurement or other variable.

To apply Kalman filtering to a given problem the following two general equations of the Kalman Filter must be applicable:

$$x_k = Ax_{k-1} + Bu_k + w_{k-1} \quad (3)$$

$$z_k = Hx_k + v_k \quad (4)$$

where the signal values, x_k, are evaluated using a linear stochastic equation. The signal is a linear combination of the previous value plus a control signal, u_k, and process noise. Eq. 4 shows that the measurement value (angle estimate) is a linear combination of the signal value and measurement noise, v_k, which is considered to be zero-mean white Gaussian noise. The variables *A*, *B*, and *H* are general form matrices but are simplified as numerical values (=1) and assumed to be constant. There is often no control signal so u_k is ignored and *A* is set to 1 since the Kalman filter is being applied on an assumed constant value. Once it is determined that the system fits into this model, estimates of the mean and standard deviation of the noise functions, v_k and w_k.

For the system as modeled, the measured value is the angle estimated using the vision system and trajectory model through Golden Section Search optimization and is written as θ_M. The estimation $\hat{x}_k$ in the general Kalman Filter equations is the estimate of the current angle of the spray and is written as φ. With the updated variables and assumptions on the general form matrices *A*, *B*, and *H*, the time update (i.e. prediction) and measurement update (i.e. correction) equations are written as:

Time Update

$$\hat{\varphi}_k^- = A\hat{\varphi}_{k-1} + Bu_k = \hat{\varphi}_{k-1} \quad (5)$$

$$P_k^- = AP_{k-1}A^T + Q = P_{k-1} \quad (6)$$

Measurement Update

$$K_k = P_k^-(P_k^- + R)^{-1} \quad (7)$$

$$\hat{\varphi}_k = \hat{\varphi}_k^- + K_k(\theta_{M_k} - \hat{\varphi}_k^-) \quad (8)$$

$$P_K = (1 - K_k)P_k^- \quad (9)$$

The iterative process between the time update and measurement update steps is shown in Figure 5.8.

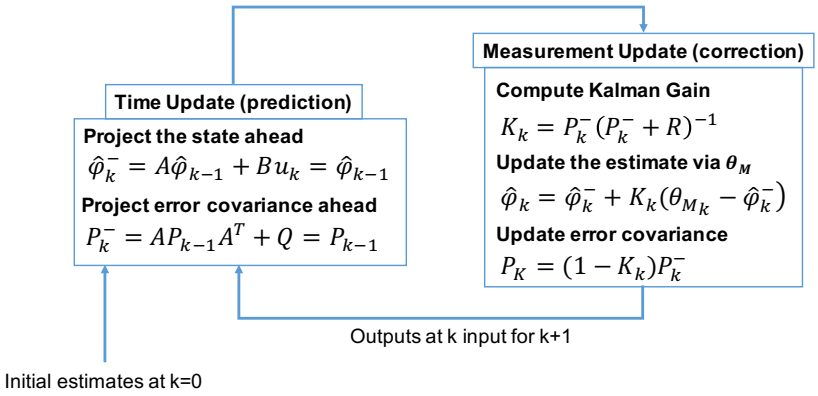

Figure 5.8. Kalman Filtering iteration through estimates.

In Eq. 7, R is an estimate of the associated noise in the system. To initialize R, the standard deviation of the first 5 sample points of the yaw and pitch angles estimated is used. An example of estimated pitch angle using the IR vision system and trajectory model over time is shown in Figure 5.9. At time 0, a solenoid valve is opened causing the initial burst of water spray. An unsteady region exists below approximately 2 seconds and is especially noisy from 0-1 seconds due to improper estimation of the angle using water classification and stereo processing and the water spray not settling at a constant angle at that time. Once the back pressure settles, the estimated angle starts to fluctuate around 10°.

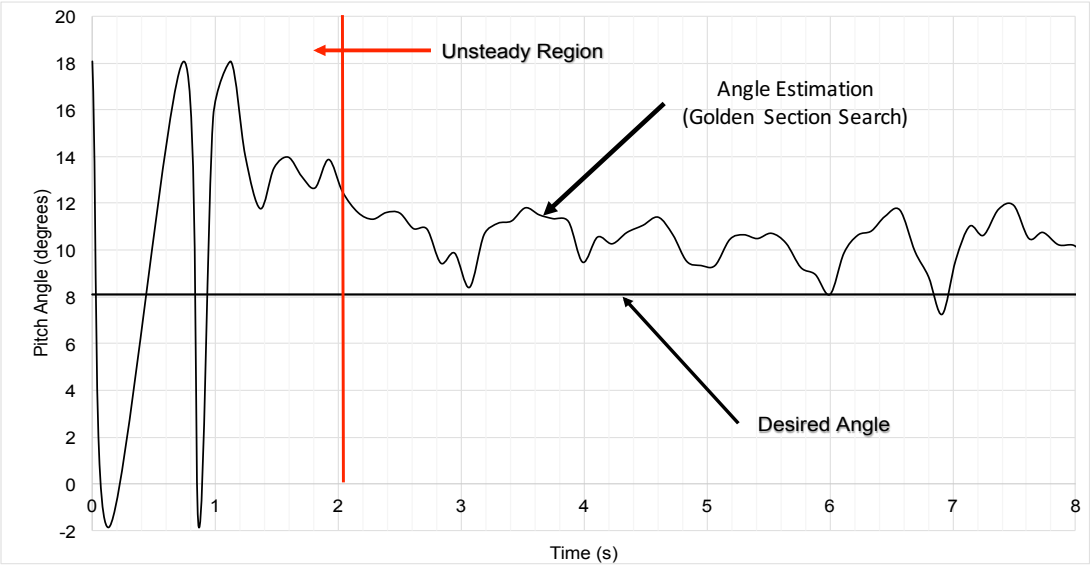

Figure 5.9. Angle estimation from Golden Section Search against desired angle from model and localized fire (setpoint).

An example of the noise in the angle measurement being Kalman filtered is shown in Figure 5.10 for a set nozzle angle of 9°. The predicted pitch angle through use of a Kalman Filter is represented with the dashed line and starts to converge to 3 seconds after opening of the valve. The first 0.5 seconds or approximately 5 data points are to compute the mean and standard deviation of the measurement and are the initial conditions of the Kalman Filter equations, *R* and $\varphi_{k=0}$. There exists some tradeoff between sampling accuracy and actuator speed since longer sample times yield better estimation of the actual spray angle. The covariance value P is used as an indicator to judge the deviation between the true value and updated value. An event-driven output can be used so when P falls below a given threshold, μ, the output is input to an angle controller. For any given initial covariance, $P_{k=0}$, the value will converge and in the suppression algorithm was initially set as *P=1*.

$$P < \mu \rightarrow \beta = 1 \tag{10}$$

$$P \geq \mu \rightarrow \beta = 0 \tag{11}$$

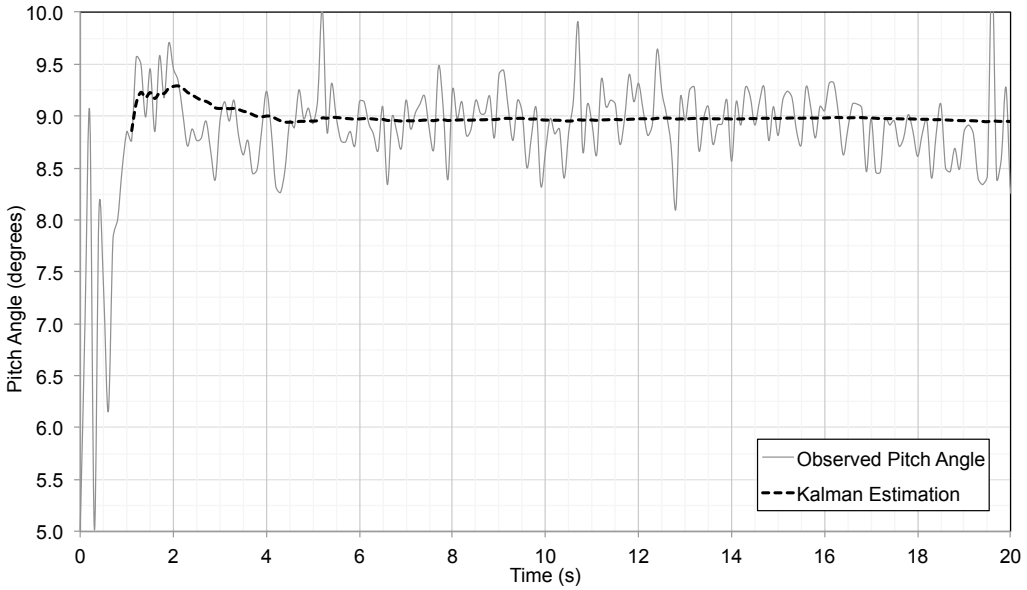

Figure 5.10. Kalman filtered estimation of the tilt angle of the nozzle.

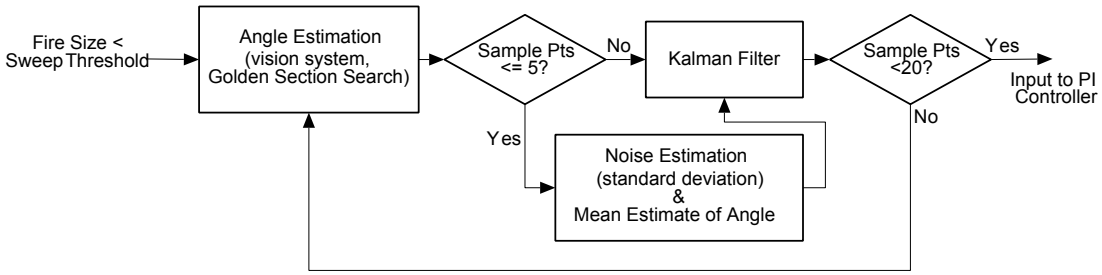

Figure 5.11. Kalman estimation process in suppression algorithm.

The Kalman estimation process used in the suppression controller is shown in Figure 5.11. First, an angle estimation is determined through use of the Golden Section Search method with data points from the IR vision system and trajectory model. The first 5 estimated angle points, are used to estimate the noise of the angle values and the mean and are used as initial conditions within the Kalman Filter. The Kalman Filter is provided with the next 15 data points, a measured value (the angle estimated with the vision system), to provide an improved estimate of the actual spray angle since the nozzle will not always be perfectly aligned in the robotic gripper or other mounted system. After the first 20 data points, 5 for initialization, and 15 for Kalman estimation (approximately 2 seconds with IR capture rate of 10 fps), the current estimate, $\varphi_{k=15}$, can be used to determine the error between the current spray angle and a desired angle or setpoint.

PID Controller

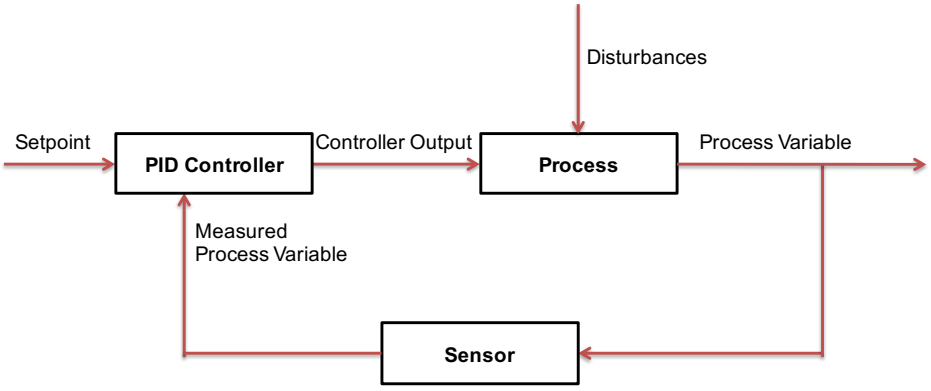

Figure 5.12. Classic block diagram of process under PID control.

PID controllers are reliable and easy to implement and often used for linear and non-linear systems with robustness to uncertainties and disturbances. The classical approach of a process control using PID is shown in Figure 5.12. For the terms included in the diagram, the process variable can be considered the nozzle pitch and yaw angle, the sensor is the IR vision system and the processing of the water spray and trajectory optimization, the setpoint is the optimal angles determined using the fire location and trajectory model, and disturbances include wind and bias issues due to the grip configuration of the fire nozzle.

Since the system uses an observer-based approach without a model of the process, PID control is an optimal controller choice. A pair of controllers were designed to control the yaw and pitch of the nozzle. The algorithm of the PID controller is as follows:

$$CO(t) = K_P e(t) + K_I \int_0^t e(\tau)d\tau + K_D \frac{d}{dt} e(t) \quad (12)$$

where *CO(t)* is the controller output for nozzle movement, *K* is a gain value applied to the integral, proportional, and derivative error and *e(t)* is the measured error between the setpoint angle (fire localization and trajectory model), θ_{SP}, and Kalman estimation of the angle of the water spray, φ_k.

$$e(t) = \varphi_k - \theta_{SP} \quad (13)$$

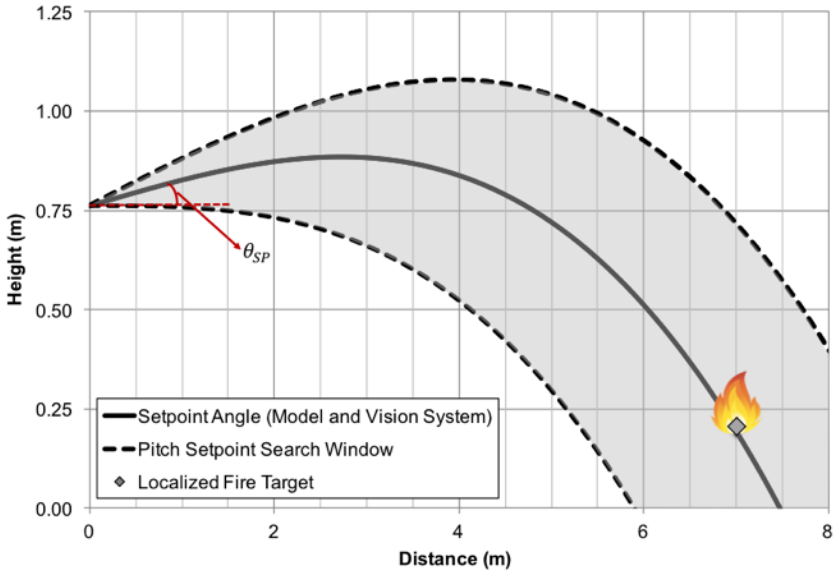

Figure 5.13. Angle setpoint calculation with trajectory model and localized fire target.

The setpoint angle, θ_{SP}, is determined using the localized fire target and the spray trajectory model. Through IR stereovision and the target at the base of the fire, *I(x, y)*, as determined using the fire segmentation and detection algorithm, the height and distance is provided. Since the trajectory model outputs a height measurement for at any given distance for an input spray angle, the error between the fire height at distance, *D*, and the spray model height at the same distance, *D*, can be minimized by iteratively searching input angles. Only a single distance is needed to calculate the height so the process is not computationally expensive and the output is the setpoint or desired angle, θ_{SP}. The angle to place the water spray on the fire target is considered stationary as the fire to suppress is assumed to remain in the same location.

In PID control, the proportional term directly scales the error so with a smaller proportional gain, the output to the motor will command smaller movements. Large gains result in an unstable filter that overshoots the desired value. The integral gain, K_I, handles errors that accumulate over time and is suitable when steady state errors are present. Large gains can interfere with response to current changes. The derivate gain, K_D, is related to how the system behaves between time intervals and is used to dampen the system and improve stability. In noisy systems, this gain is often ignored since error changes are not constant with time.

Due to the high noise associated with the angle measurement in computer vision, the derivative gain was set to zero and a PI controller was implemented. An error dead-zone, or deadband, is used to reduce the amount of actuation and rejects the output from the controller if the measured angle is within the deadband limit. Deadbands are found within many systems including robotics and machine tools [111, 112], pneumatic actuators [113], servo systems [114], power units [115] and many more. If the measured angle error falls outside the deadband the output from the PI controller is applied to the servo motor associated with the corresponding yaw or pitch angle. If the error is bounded by the deadband no actuation is required as the observed angle falls within the range of the desired orientation for suppression.

$$u(t) = \begin{cases} u, & e(t) \geq DB \\ 0, & |e(t)| \leq DB \\ u, & e(t) \leq -DB \end{cases} \tag{14}$$

This makes the controller event-driven in that the control output is only used if the observed pitch or yaw angle is outside of the deadband. The width of the deadband was set by determining

the angle deviation from the trajectory model that results in an area of the wood crib fire still being reached by the spray. For a targeted fire in view, a deadband of the desired angle ±1° was used. The trajectory path of the desired pitch angle ±1° is shown in Figure 5.14 in which the wood crib fire is represented by the dashed box in red. The deadband limits can be constricted in a more accurate and reliable targeting scheme or with a tighter spray pattern as further deviation from the desired path may not reach the fire. Larger spray patterns may have softened deadband limits due to the larger spray landing zone reaching the fire despite more significant deviation from the optimal yaw and pitch angle.

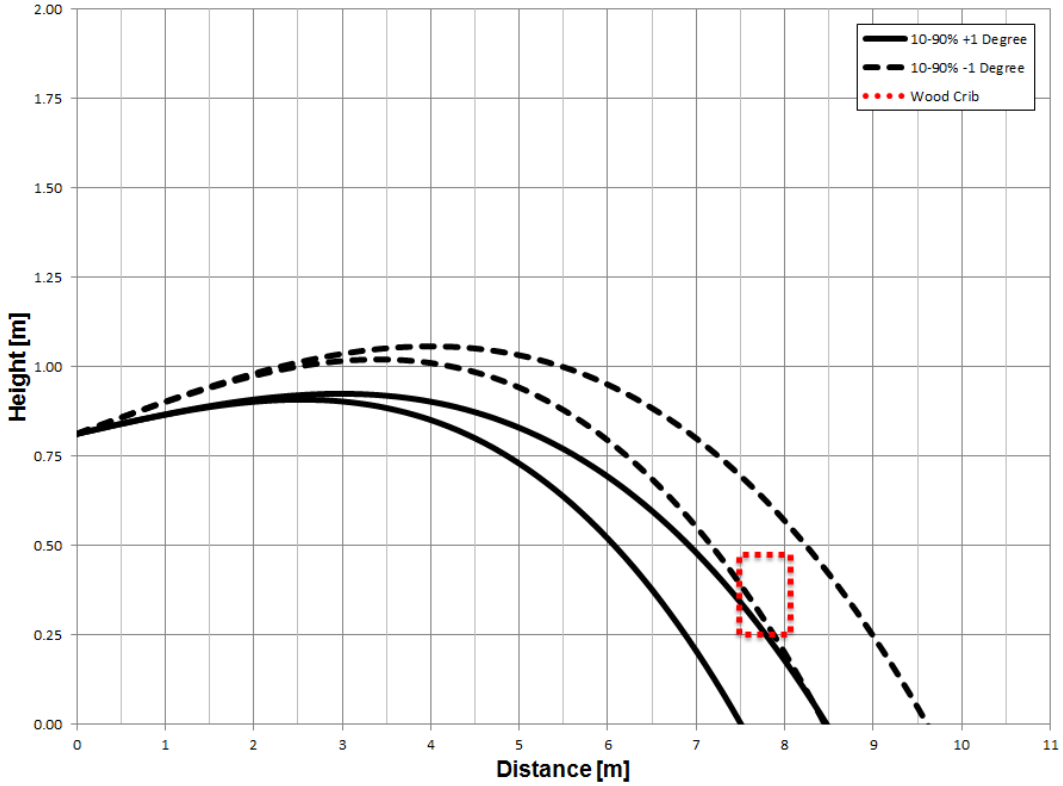

Figure 5.14. Spray trajectory path at deadband limits in PI controller.

Manual tuning was performed to set K_P and K_I through experiments performed with real time acquisition of the spray angles as no physical model fully represents the system. A proportional gain of 1 was the initial value used in testing but resulted in overshooting of the deadband limits with a high fluctuation in acquisition angle due to large shifts in the direction of the spray. The proportional gain, K_P, was incrementally decreased until a value of 0.75 was determined to perform well in combination with an integral gain of $0.1K_P$ ($K_I = 0.075$). Initial results with integral gains applied resulted in high overshoot due to integral buildup at the start of

the test since a sampling time is used and the nozzle may deviate from the desired value by a large amount. To account for integrator windup, the integral portion of the control is set to zero upon the initial actuator adjustment and is accumulated after each time the PI controller is used to actuate the nozzle. Each time the nozzle is adjusted, the error in the current angle estimation before the spray settles at an angle increases since the classification method uses a set of consecutive images to estimate position. After the sampling interval ends, the controller is used to actuate nozzle given that the position is outside of the deadband zone for the desired nozzle direction as calculated using the fire position and trajectory model. The PI control scheme is presented in Figure 5.15. Only after 20 data points have been used in the Kalman estimation process described prior will the PI controller be used. However, since the fire size and fire target are continuously determined, if the fire size decreases sharply in size (>50% decrease), the PI controller can be bypassed and a sweeping pattern applied since the spray has reached the fire target area.

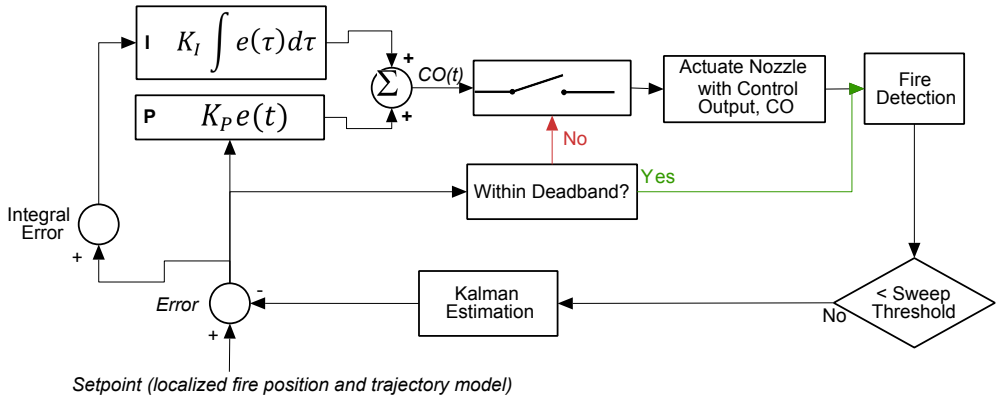

Figure 5.15. PI controller diagram for motor actuation.

The results for pitch correction are presented in Figure 5.16. The estimated pitch angle is plotted against time with the Kalman filter estimation in each sampling window (20 data points). The set pitch motor angle is shown in black and is only changed when the estimated angle falls outside the deadband. At the start of the test the pitch angle is above the deadband limit and decreases using the Kalman estimated angle and PI controller. The initial response of the controller resulted in the estimated spray angle to still fall outside the deadband limit so a second control output was sent to the pitch motor at approximately 133 seconds. After this second control output the spray angle was continuously estimated to fall inside the deadband so the pitch motor remained fixed.

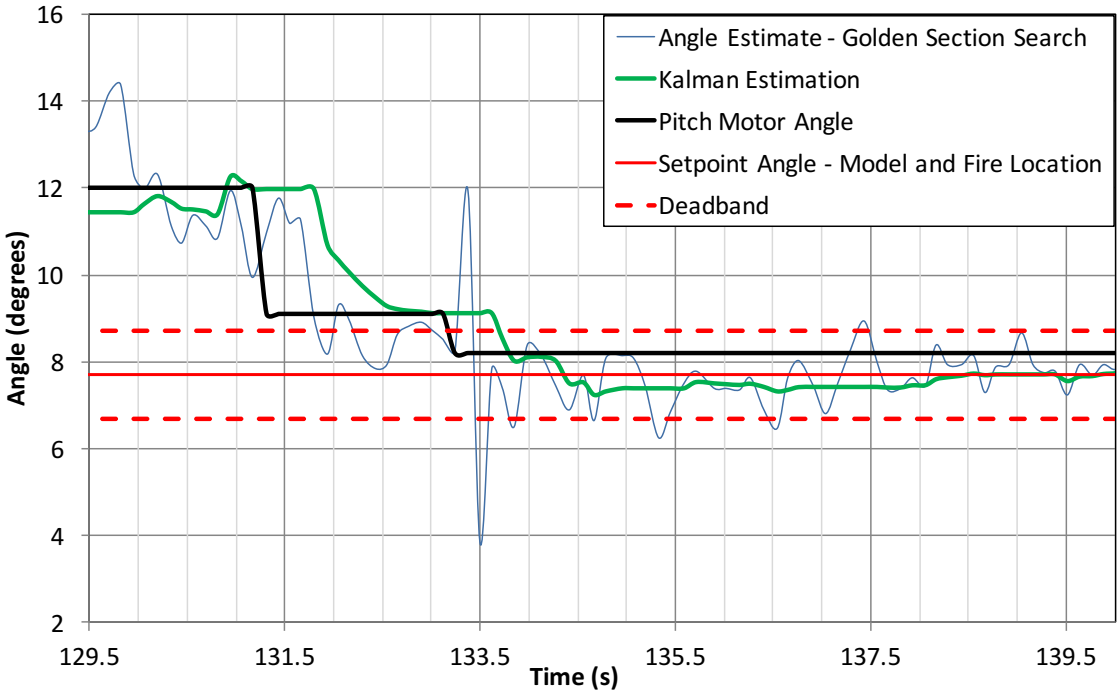

Figure 5.16. Kalman Filtering and motor response using PI controller.

5.4.7 Visual Servoing

A secondary control scheme was created to handle firefighting scenarios where the spray has reached the fire. A previous suppression algorithm showed this technique to be able to successfully manipulate a nozzle according to movements of a fire target in the 2D IR image array. The target is tracked and the pan-tilt system uses a step function to actuate the nozzle in the direction the target moves. This process is used in larger fires where the fire is initially knocked down and remaining portions of the fire remain burning. If the bottom of the wood-crib is suppressed, the targeted area should move towards the top of the image frame so the nozzle increases the pitch angle in a constant step size. Given a target

$$T = I(x, y) \tag{15}$$

where x and y represent the pixel row and column of the fire target respectively. The servoing process will adjust the nozzle as follows:

$$u_{pitch} = \begin{cases} -\delta, if\ \left(T(x_{current}) - T(x_{previous})\right) > 0 \\ +\delta, if\ \left(T(x_{current}) - T(x_{previous})\right) < 0 \end{cases} \tag{16}$$

$$u_{yaw} = \begin{cases} +\delta, if\ \left(T(y_{current}) - T(y_{previous})\right) > 0 \\ -\delta, if\ \left(T(y_{current}) - T(y_{previous})\right) < 0 \end{cases} \quad (17)$$

The step value δ is a constant angle applied to both servo motors to step in the direction of movement in the fire target and is set at 0.5°.

5.5 Decision Tree

To design the overall nozzle controller to behave intelligently, various modes or states are used to determine an appropriate response. Once the valve is opened and suppression has started, a decision tree is used to determine the proper mode of action. The various modes include continued sweeping motion, trajectory optimization and with a proportional gain controller, visual servoing mode, and completed suppression mode. Feedback is used to determine the fire size at every time step in the system to determine if the fire size is decreasing, increasing, unchanged, or is fully extinguished. The spray is segmented and classified and used with the IR stereovision system to measure the yaw and pitch angle of the spray to determine if errors exist between the set position of the nozzle and current position. Bias errors with the motors or improper grip of the nozzle by the robot can lead to such errors.

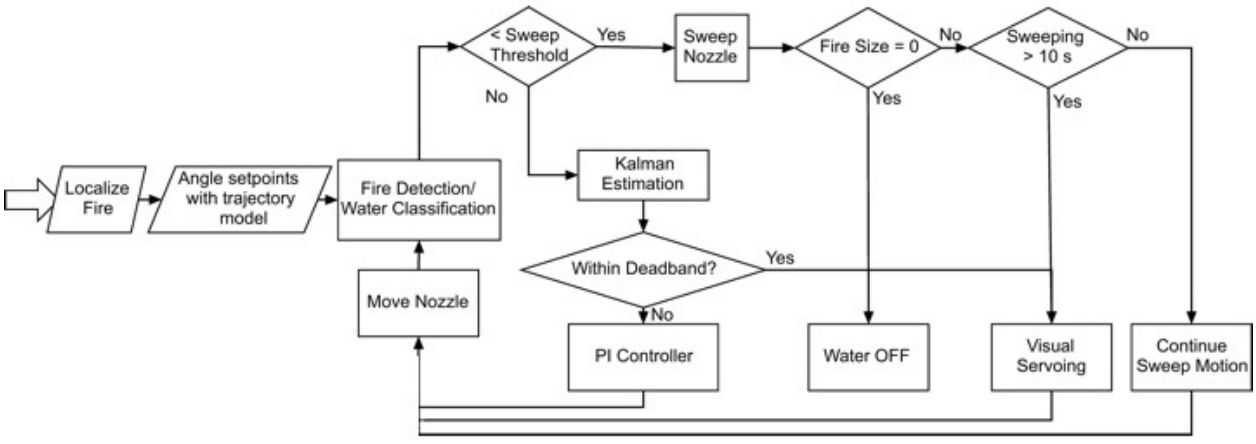

Figure 5.17. Decision tree controller used in nozzle actuation for autonomous fire suppression.

The fire is localized by segmenting the fire using variance and intensity thresholds and the 2D fire target in the 256x320 IR image array is compared against a depth map provided by the IR stereovision system to provide a 3-dimensional location. This location is used with the trajectory

model to determine the setpoint pitch and yaw angles to place the water spray on the fire base. Fire detection and water classification are performed for every image acquired to segment water and fire and calculate the fire size (in pixels) and fire target (row and column). If the total size of the fire increases between frames, the larger value is used as the peak fire size to use in comparisons to the current fire size. The current fire size is divided by the largest fire size and if the ratio falls below a sweeping threshold than the nozzle oscillates back-and-forth to cover the area. A large decrease in the fire size is used as evidence to indicate the water spray has reached the fire target. As the spray may not be explicitly located at the fire base, sweeping is used to cover the entirety of the fuel bed to ensure the fire is fully suppressed. If the nozzle is in the sweeping state for more than 10 seconds it is an indication that the nozzle is not properly reaching the entirety of the wood crib based on empirical evidence from fire testing. If this situation occurs, the visual servoing control process is used to adjust the nozzle based on updates to the fire target. Based on the oscillation frequency and amplitude, the droplets may not reach the back of the wood crib so often the nozzle must be pitched upward for better performance.

If the sweep threshold is not met, Kalman estimation of the spray angles and PI controller are used to adjust the nozzle. The trajectory optimization and angle estimation algorithms are used with the desired yaw and pitch angles to estimate the error to correct. Once the sampling period ends (20 data points), the output is used with the deadband limits to determine if both angle orientations are accurate according to the trajectory model and the fire location. If the output is outside the deadband, the PI control sends the controller output to the corresponding pitch or yaw motor. If the sweep threshold is not met and the yaw and pitch angles are determined to be accurate for suppression, visual servoing is used in lieu of PI control. For the system described, this scenario arises due to larger pressure losses in the system causing a false prediction of the desired pitch angle and results in underspray of the fire. For each iteration of the control process the motor commands from each state (continued sweeping, visual servoing, PI control), is sent to adjust the nozzle position.

5.6 Experiments

The autonomous suppression system was evaluated at a large-scale test facility in both indoor and outdoor environments. Tests were conducted with forced offsets introduced to the system such that the initial attack angle of the nozzle did not reach any part of the wood crib fire. Other tests were done without any offset introduced to show how the system responds.

5.6.1 Scenarios

A total of 20 suppression tests were performed in the study to evaluate the performance of the autonomous system in indoor and outdoor environments. A total of 8 tests were performed without an unknown disturbance introduced into the system to show how well the trajectory model predicts the orientation of the nozzle to reach the fire. Propagating fires were used in 2 tests to show performance of the system when the bottom of a fire was suppressed with a large portion at the top of the wood crib continuing to burn. The other 12 tests had an offset introduced to the system that was corrected by the system using the vision system, controller, and trajectory model. The fires were placed at further distances than in the previous system to show how a linear assumption of the water spray is not acceptable and that a predictive model is necessary for accurate spray direction.

The experimental setup consists of wood crib fires placed at varying positions and heights within the field of view of the suppression system with a maximum distance of 9.5 m. The same size wood cribs were used to show repeatability of the system. The wood crib consisted of 24 sticks, measuring 50 mm in diameter, arranged in 6 layers of 4 sticks. The overall dimensions of the array were 300 mm × 300 m × 200 mm. The wood cribs were ignited using a fuel source placed underneath and were allowed to fully develop before suppression. This setup was used in clear condition tests with the autonomous system as well as in clear condition tests with a forced offset introduced into the system to show the robustness of the approach to a poor initial guess or external disturbances such as air currents.

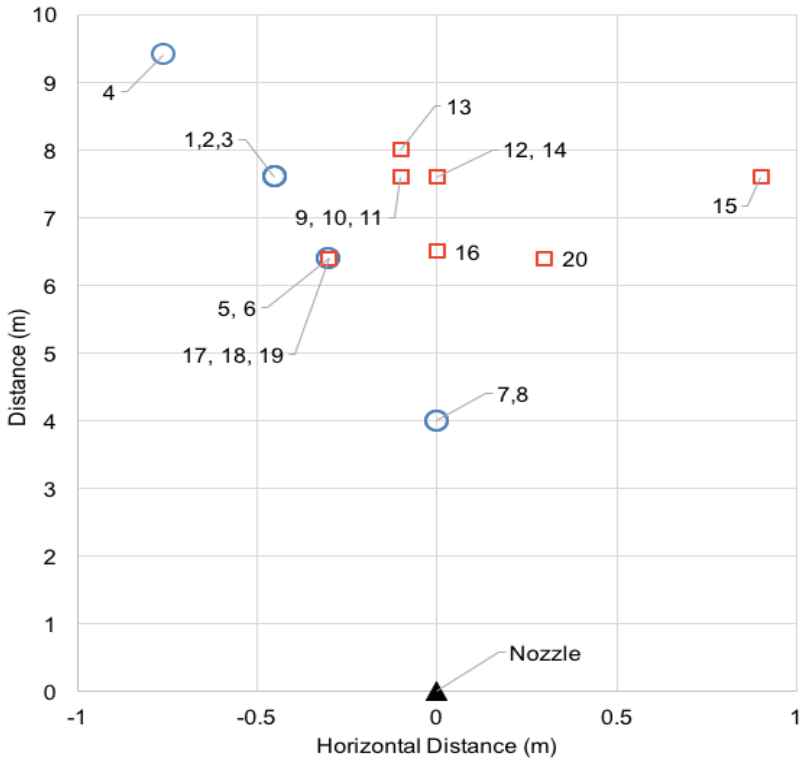

Figure 5.18. Wood-crib fire locations for labeled non-offset tests (blue circle) and offset suppression tests (red square)

5.6.2 Procedure

Suppression tests were initiated by igniting a liquid fuel source beneath a wood crib fire. Once the fuel source had burned off and the wood crib had become fully developed, approximately 3 minutes later, the autonomous fires suppression algorithm was initiated. There was no time recorded for fire growth since the system initiated suppression with a fully developed wood crib fire in the field of view. The algorithm detected the fire, positioned the nozzle and a solenoid valve was opened upon detection in under 0.2 seconds. For tests with forced offsets introduced, the system adjusted the nozzle according to the decision tree previously proposed. The solenoid valve automatically was closed once the fire was no longer detected.

5.7 Results

5.7.1 Nozzle Response and Suppression Times with Proper Orientation

Results from tests performed without an offset on the initial nozzle orientation are summarized in Table 1. The initial yaw and pitch direction are the desired angles for the spray to reach the target given the 3D fire location input to the trajectory model. The distances of the fire ranged from 4.0 to 9.7 m. The total suppression time is the duration from the opening of the valve to when the IR sensors no longer detect the presence of a fire in view. The sweeping time is the total time the nozzle oscillated from the fire being knocked down to fully suppressed. An indication of visual servoing is provided to show what tests needed nozzle adjustments due to erroneous initial targeting or long sweeping times at one pitch angle not fully suppressing the fire.

Table 5.1 Results of Suppression Tests without Offset on Initial Orientation

No.	Scenario	Fire Distance [m]	Estimated Angles		Suppression Time [s]	Sweeping Time [s]	Visual Servoing?
			Pitch [°]	Yaw [°]			
1	Outdoor	7.6	8.3	3.4	16.3	12.4	Yes
2	Outdoor	7.6	6.4	3.4	7.5	6.4	No
3	Outdoor	7.6	6.4	3.4	8.2	5.8	No
4	Outdoor	9.4	9.3	4.6	13.4	12.2	Yes
5	Indoor	6.4	5.9	2.9	16.2	10.2	No
6	Indoor	6.4	5.9	2.9	12.1	8.5	No
7	Propagating	4.0	3.1	0.0	7.8	0.0	Yes
8	Propagating	4.0	3.1	0.0	8.7	0.0	Yes
					Suppression Time for Single Location (Tests 1-3):		10.67 ± 4.89 s

The suppression time for the first fire location was 10.67 s with a standard deviation of 4.89 s. The other tests fell within the first location range despite some indoor tests (5 and 6) and larger wood cribs (7 and 8). In Test 1, the water was delivered short of the fire target, however, the observed pitch angle was within the deadband limit set by the controller. This required visual servoing to increase the pitch to reach the fire. Still images from Test 4 are shown in Figure 5.19 from a fully developed fire to the end of test with the fire fully suppressed. An indoor test is displayed in Fig. 17 with the fire size versus time plotted in Fig. 18. The base of the fire is

suppressed in Fig. 19(b) and as the fire target row rises in the 2D IR image array the nozzle increases the pitch angle as shown in Fig. 19(c).

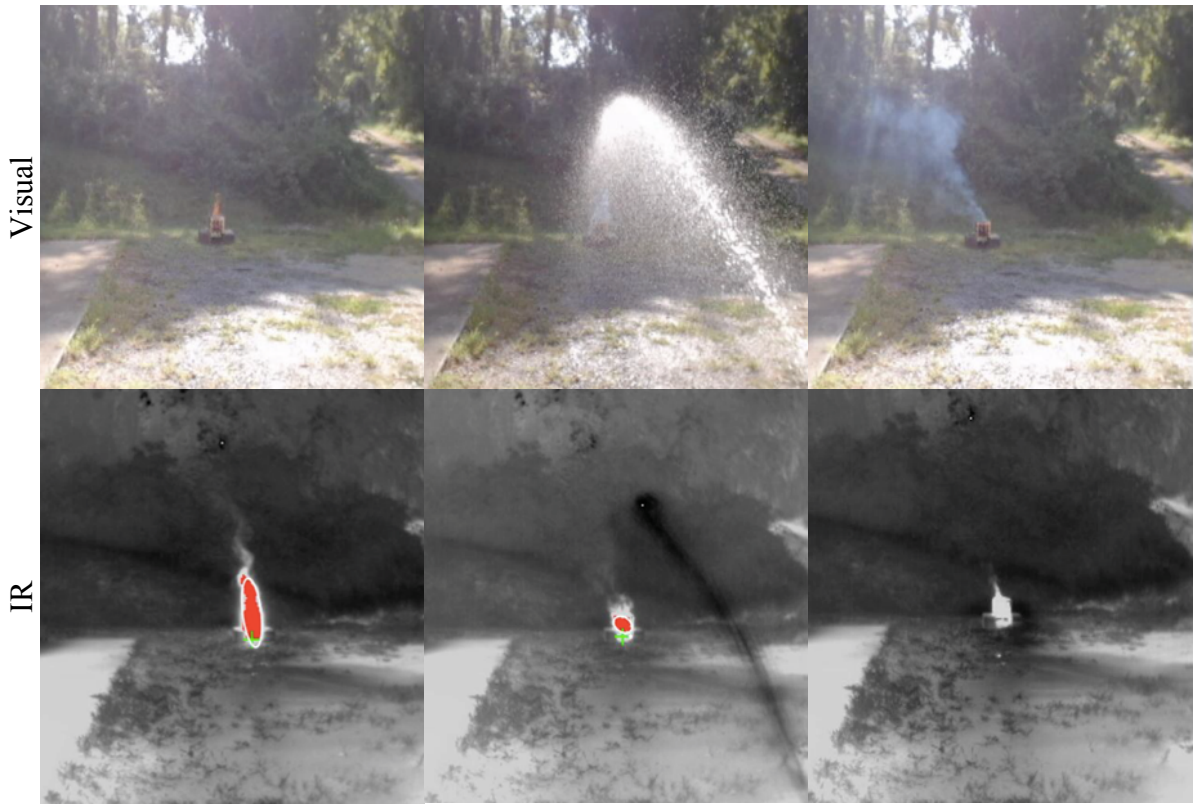

(a) (b) (c)

Figure 5.19. IR and visual images from Test 4 (a) fully developed (b) fire knocked down (c) end of test

The fire size, in pixels, was tracked throughout every test and is shown as a function of time in for Test 4 in Figure 5.20. Indicators of the opening of the valve, initiation of sweeping motion, visual servoing if required in the test, and the time the fire is fully suppressed are shown. The control response for Test 4 is shown in Figure 5.21. The estimated angle from Golden Section Search and the Kalman estimation are provided along with the motor position for the pitch and yaw of the nozzle throughout the test. After 1.2 seconds, the system sweeps the nozzle back and forth as the fire size decreased by over 50% indicating the water spray reached the targeted fire. Since the system sweeps the fire base for approximately 10 seconds, visual servoing was used to step the pitch angle up by 0.1 degrees until the fire was fully suppressed.

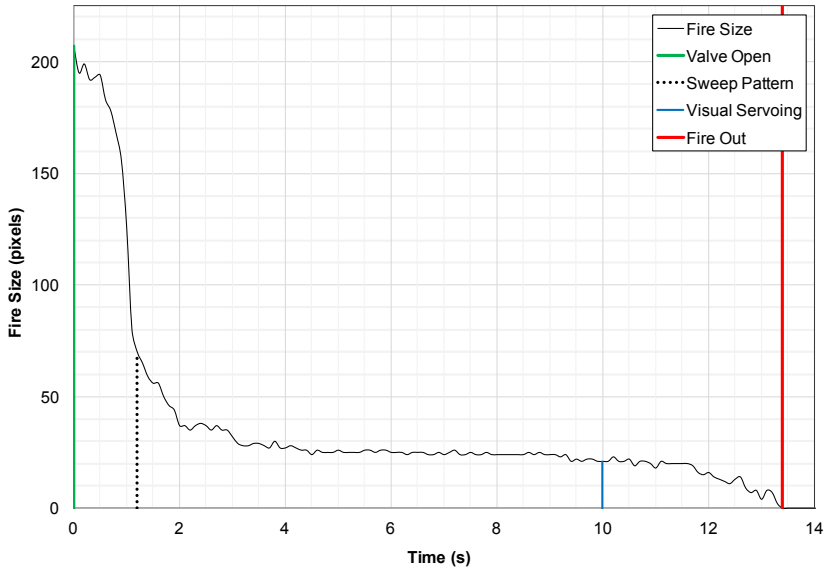

Figure 5.20. Fire size versus time for Test 4.

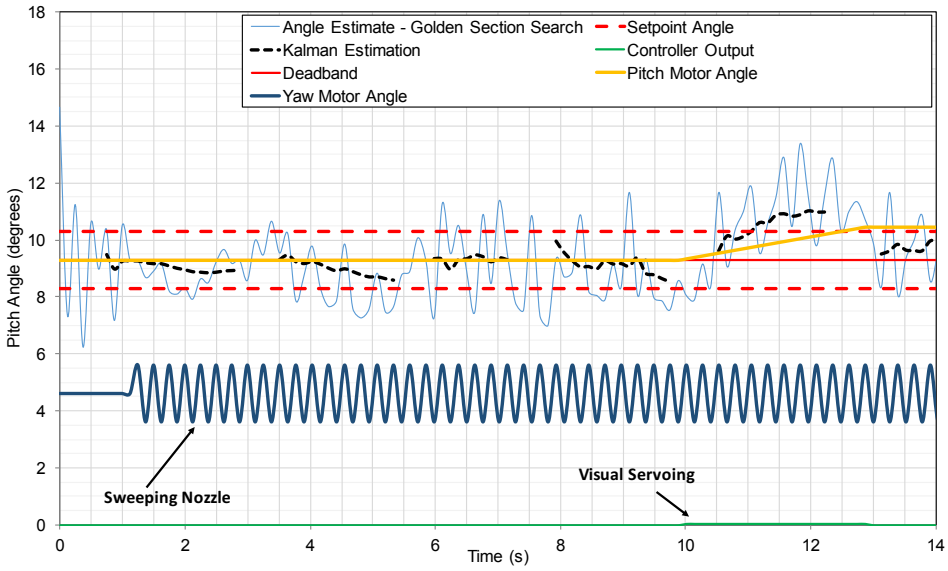

Figure 5.21. Control Response for Test 4.

An indoor test is displayed in Figure 5.22 with the fire size versus time plotted in Figure 5.23. The valve was opened at 5 seconds and the fire is reduced by approximately 50% after 2 seconds initiating the sweeping pattern. The fire was successfully extinguished at 17 seconds. The control response is provided in Figure 5.24 with the sweep pattern applied to the yaw motor 2 seconds after the valve is opened.

(a) (b) (c)

Figure 5.22. IR and visual images from Test 6 (a) fully developed (b) fire knocked down (c) end of test with smoke buildup.

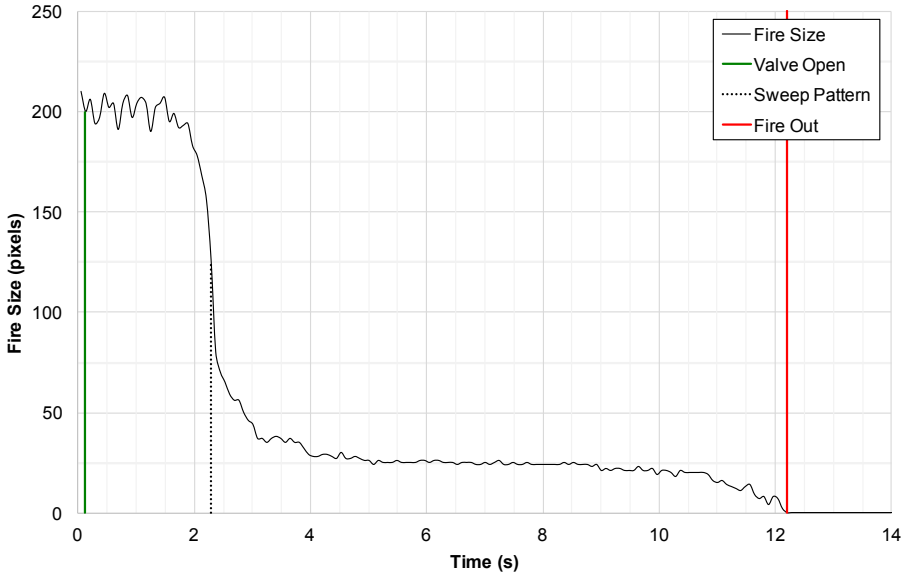

Figure 5.23. Fire size versus time for Test 6.

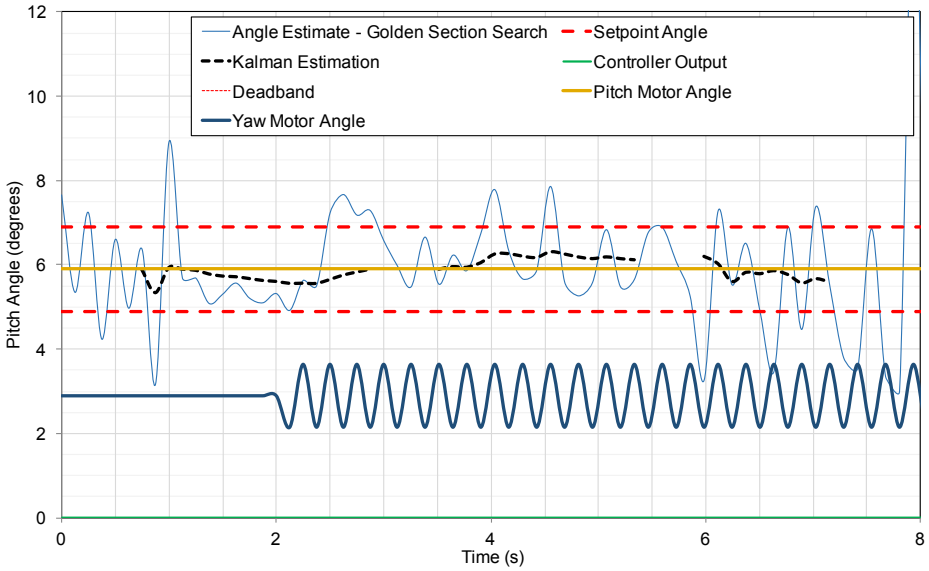

Figure 5.24. Control response for Test 6.

A taller wood crib was used to show how well the target of the fire is tracked under the visual servoing process control. The fire size was approximately three times the size of the other fires used. The base of the fire is suppressed in Figure 5.25(b) and as the fire target row rises in the 2D IR image array the nozzle increases the pitch angle as shown in Figure 5.25(c). For the propagating fire tests (7, 8), the suppression times were 7.8 and 8.7 seconds. The system initially targeted the bottom of the fire accurately and as the fire target moved upward in the 2D IR image, the nozzle pitch was increased until fully suppressed.

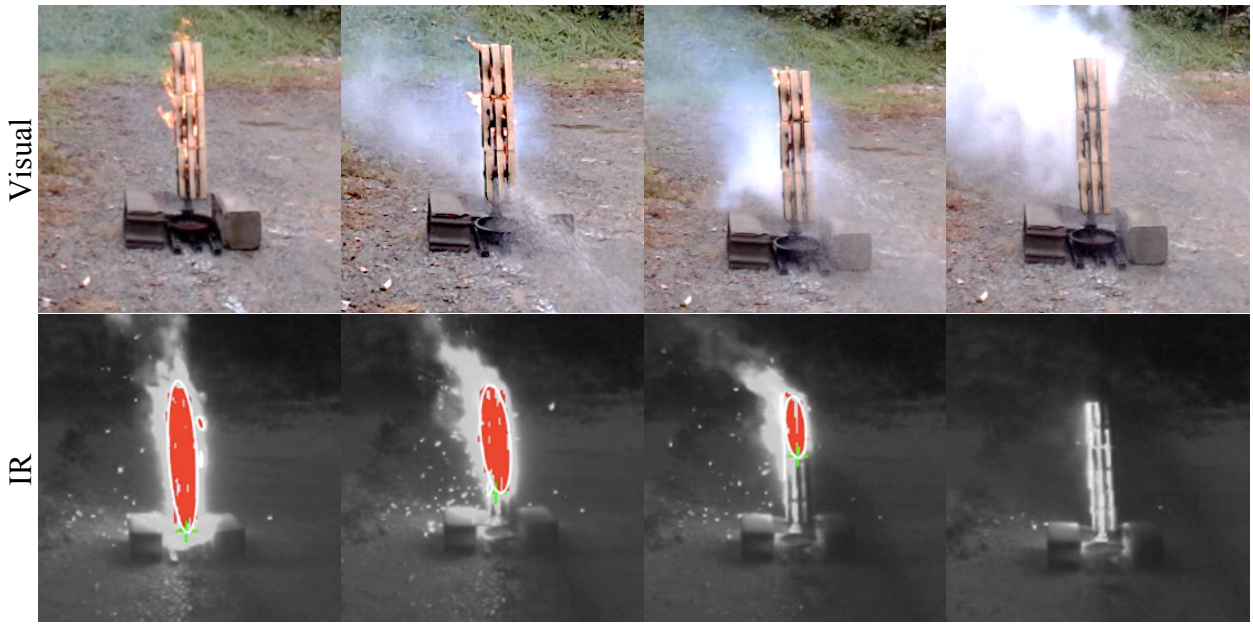

Figure 5.25. IR and visual images from Test 7 (a) fully developed (b) bottom portion of fire suppressed (c) middle portion of fire suppressed (d) end of test

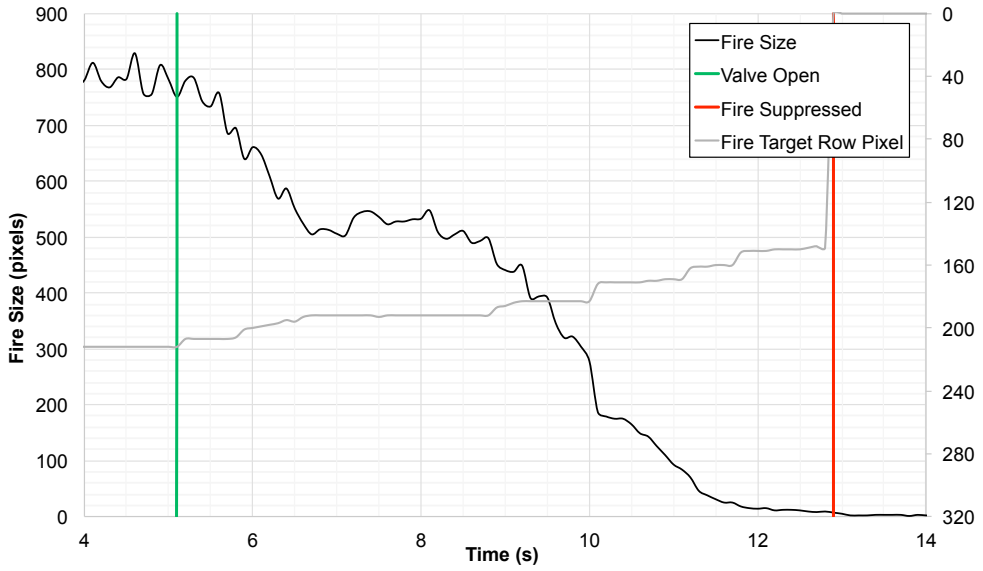

Figure 5.26. Fire size and target row versus time for Test 7.

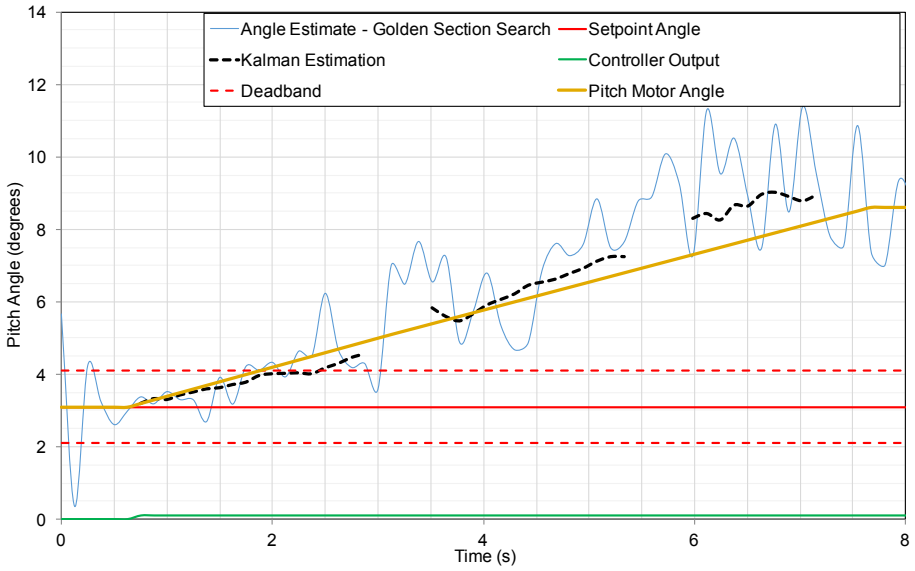

Figure 5.27. Control response for Test 7.

5.7.2 Nozzle Response and Suppression Time with Initial Offset Orientation

Results from tests performed with the addition of an offset on the initial nozzle orientation are summarized in Table 2. The initial angles are the desired angles for the spray to reach the target given the 3D fire location input to the trajectory model. The offset conditions to the initial nozzle placement are listed. A negative angle indicates the nozzle was set to underspray the target at the beginning of the test. Negative yaw initial offsets indicate the nozzle started spraying to the left of the calculated desired yaw direction. The distances of the fire ranged from 6.4 to 9.7 m and indoor and outdoor environments were used.

Table 5.2 Results of Suppression Tests with Offset on Initial Orientation

No.	ENV	Fire Distance [m]	Initial Angles Pitch [°]	Initial Angles Yaw [°]	Offset Conditions Pitch [°]	Offset Conditions Yaw [°]	Suppression Time [s]	Sweeping Time [s]	Response Time [s]	Visual Servoing?
9	Outdoor	7.6	8.3	-0.8	-5	-5	16.3	12.4	1.9	Yes
10	Outdoor	7.6	8.3	-0.8	-5	0	26.9	8.6	4.7	Yes
11	Outdoor	7.6	8.3	-0.8	-5	+5	22.9	15.2	3.4	Yes
12	Outdoor	7.6	6.7	0.0	-5	-5	13.4	12.2	2.4	Yes
13	Outdoor	8.0	7.1	-0.7	-5	-5	15.5	11.5	2.9	Yes
14	Outdoor	7.6	6.7	0.0	-5	0	8.1	5.4	2.1	No
15	Outdoor	7.6	7.2	6.8	-5	+5	27.9	21.6	3.7	Yes
16	Outdoor	6.5	4.7	0.0	+5	+5	12.0	6.9	2.5	No
17	Indoor	6.4	6.4	-2.7	-5	+3	15.6	3.0	3.6	Yes
18	Indoor	6.4	6.4	-2.7	-5	+3	12.5	7.6	2.2	No
19	Indoor	6.4	6.4	-2.7	-5	-3	11.1	3.2	2.8	Yes
20	Indoor	6.4	6.4	2.7	-5	+3	6.2	0.0	1.6	No
							Suppression Time at Location 1 (Tests 9-11):			22.03 ± 5.35 s

The suppression time for the first fire location (Tests 9-11) was 22.03 with a standard deviation of 5.35 s. The average initial response time or duration of time it took from opening of the valve to the initial correction in nozzle orientation was 2.97 s. For the other locations in the outdoor environment, and the indoor suppression tests, the suppression times fell below the average time for the first location. Suppression times in the indoor test setting were 11.35 s with a standard deviation of 3.91 s. Visual servoing was required in 8 out of the 12 tests. In most of these cases, the sweeping time exceeded the acceptable amount of time for full extinguishment as set by the controller so the nozzle was shifted upward to reach the back of the wood-crib. In Figure 5.28(a) is a visual image taken from Test 13 at the beginning of the test with an initial offset forcing the nozzle to underspray the target. The nozzle is corrected based on the estimated yaw and pitch angles and reaches the fire in Figure 5.28(b). IR representations of these two events are displayed in the Figure 5.28(a) and Figure 5.28(b). The fire is highlighted in red and the water spray is classified and displayed in blue to the right of the fire. In Figure 5.28(a) the water is noticeably underspraying the fire and in the corrected position, Figure 5.28(b), the fire size has decreased by more than 50% the initial size (in pixels) and the nozzle begins sweeping the fire base.

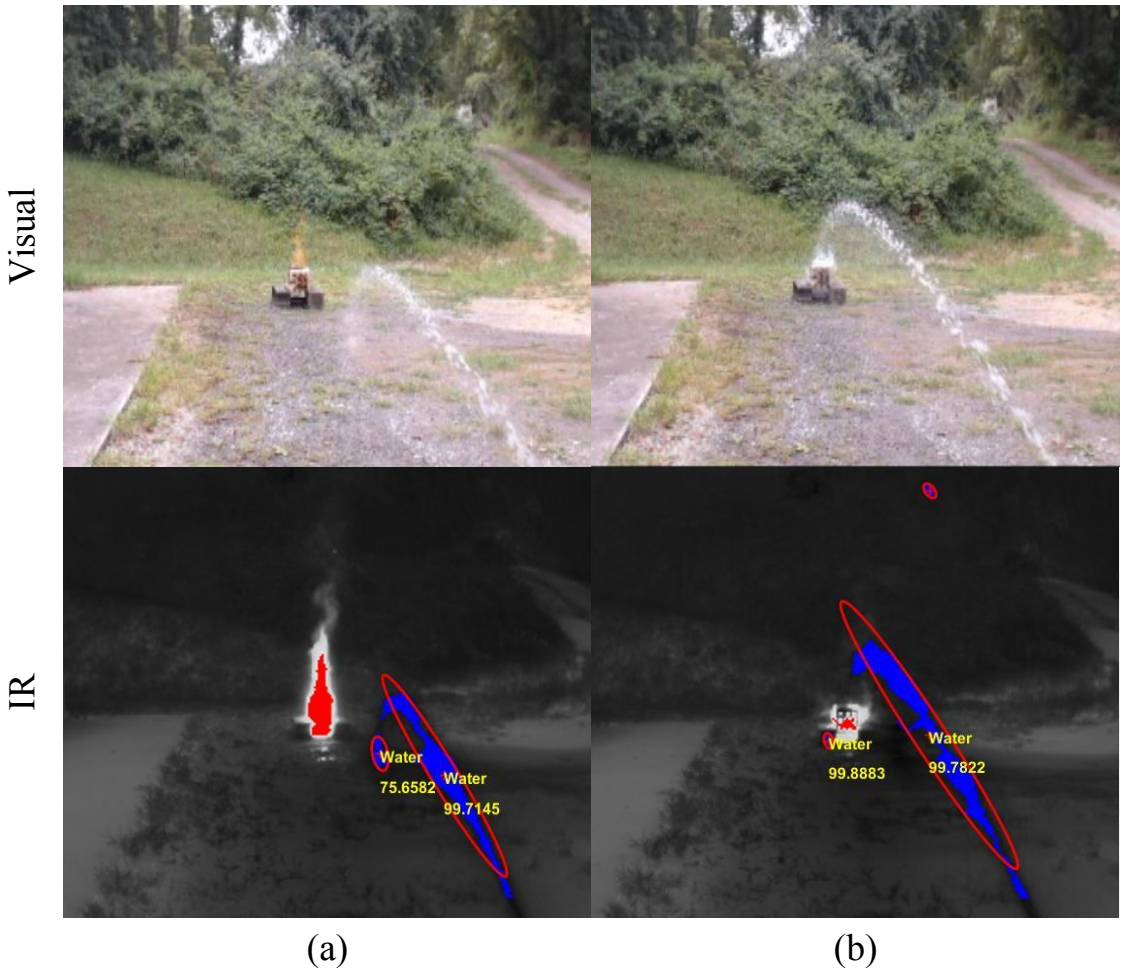

Figure 5.28. Visual and IR images of nozzle direction in Test 13 at (a) initial nozzle direction with forced offset (b) corrected angle with water spray reaching fire

The pitch angle throughout Test 13 is shown in Figure 5.29 from the opening of the valve. The desired angle with a 1° deadband is located around 7.1°. The first 5 measurements are taken to estimate the nozzle angle and the standard deviation is used as the initial noise value, R, input to the Kalman filter. After 15 data points are collected, the error is used with the PI controller to actuate the nozzle upwards toward the desired angle. During the next sampling period, the pitch angle falls within the deadband indicating it is set at the proper placement to place the water spray on the fire base.

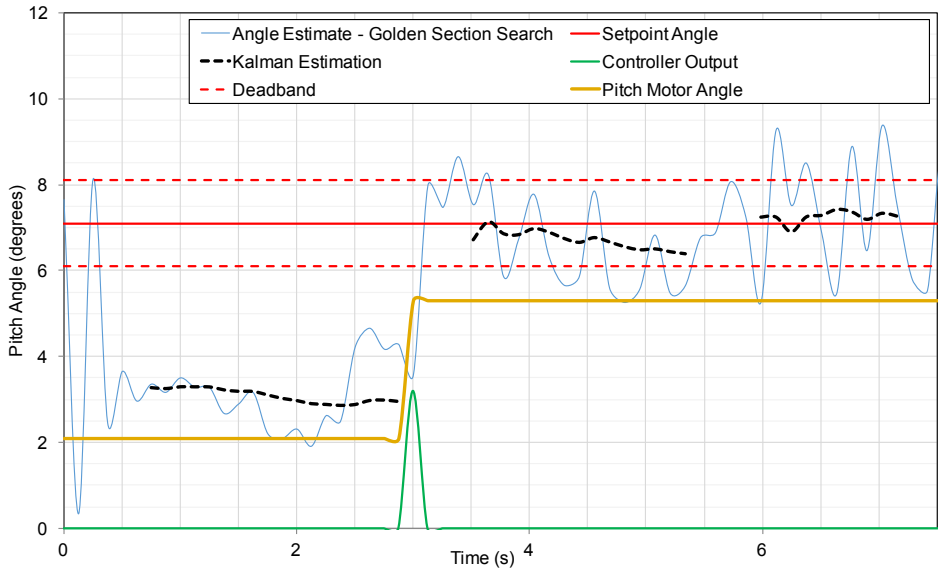

Figure 5.29. Controller response in Test 13.

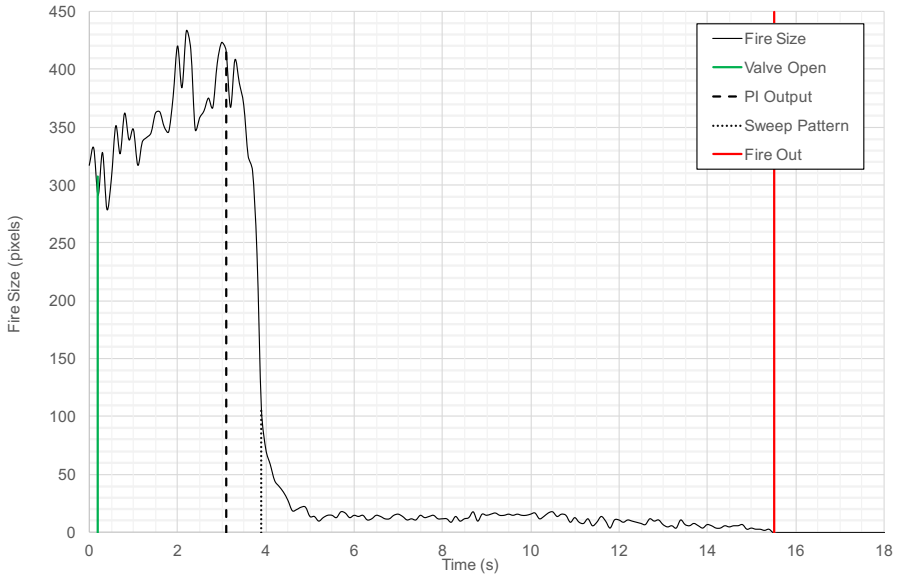

Figure 5.30. Fire size and target row versus time for Test 13.

Major events from Tests 16 and 20 are shown in Figure 5.31 and Figure 5.34. The events include: the fully developed wood-crib fire prior to system start, initial spray placement off-target, corrected nozzle direction, and extinguishment of the wood-crib fire. Test 16 was performed outdoors with an initial offset of 5° applied to the desired nozzle orientation resulting in the spray landing to the right and further away than the fire location. Test 20 is an indoor suppression test with offsets of -5° and -3° applied to the desired pitch and yaw angles respectively. The fire has

been shown in red to indicate the relative size during each of these events. Figure 5.32 and Figure 5.35 include the fire size tracked during each test. Points throughout the test are highlighted for opening of the value, initial PI control output, initiation of the nozzle sweeping motion, and the time visual servoing was used to adjust the nozzle further. Once the fire size reaches zero, the solenoid valve was closed. The control response for both tests are shown in Figure 5.33 and Figure 5.36. In test 16, the first sampling period with Kalman estimation indicates the effective spray angle is larger than the setpoint determined with the localized fire and spray model. A control response shifts the pitch motor downward and the spray angle is then estimated to fall within the deadband limits set. In test 19, the pitch motor is shifted upward to account for the 5° bias introduced to the pitch setting at the beginning of the test. Visual servoing is required

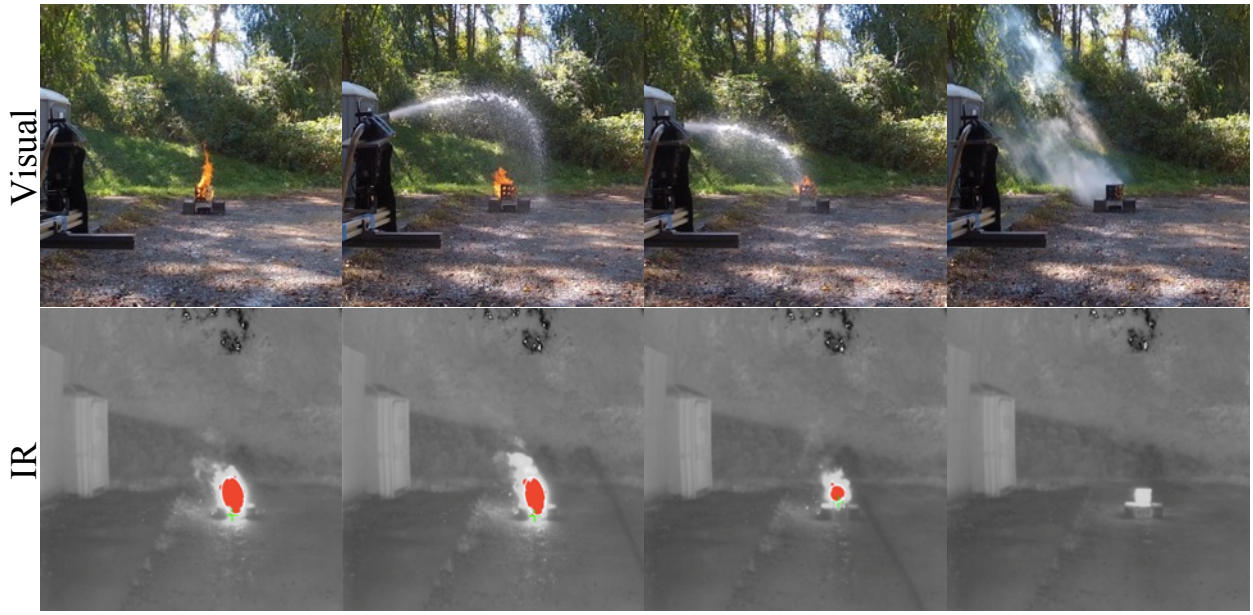

Figure 5.31. Test 16 Visual and IR images at (a) fully developed fire (b) initial off-target spray over and right of fire (c) correction of nozzle direction (d) suppressed fire.

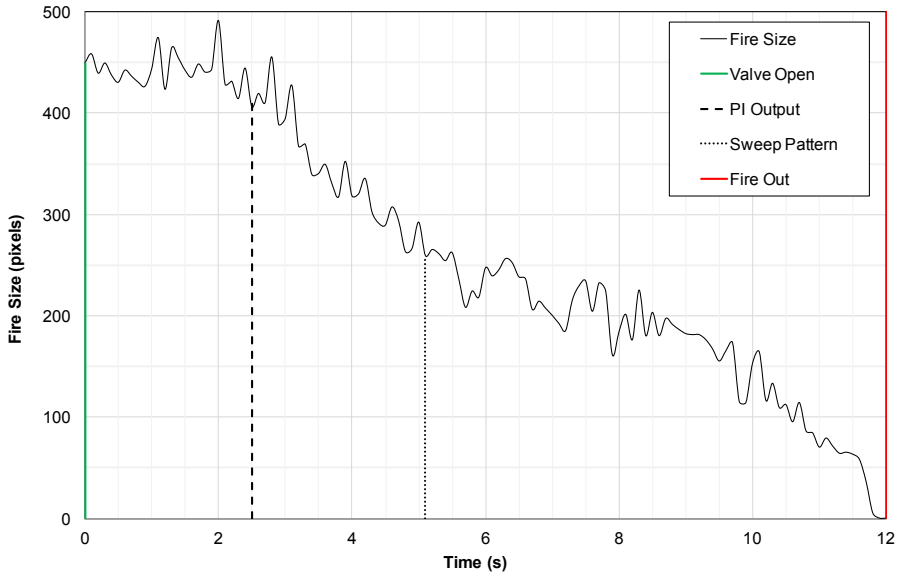

Figure 5.32. Fire size and target row versus time for Test 16.

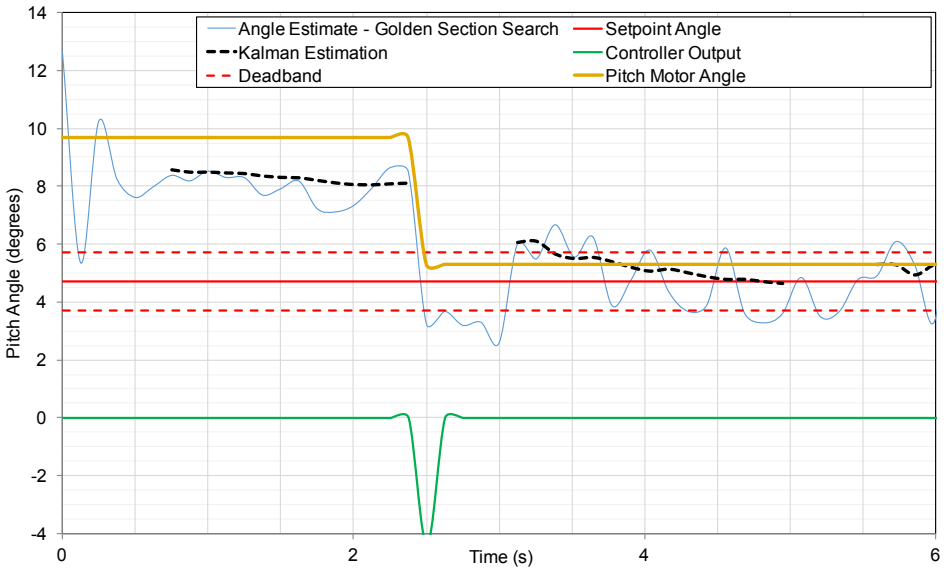

Figure 5.33. Controller response for Test 16.

(a) (b) (c) (d)

Figure 5.34. Test 20 Visual and IR images at (a) fully developed fire (b) initial off-target spray under and left of fire (c) correction of nozzle direction (d) suppressed fire.

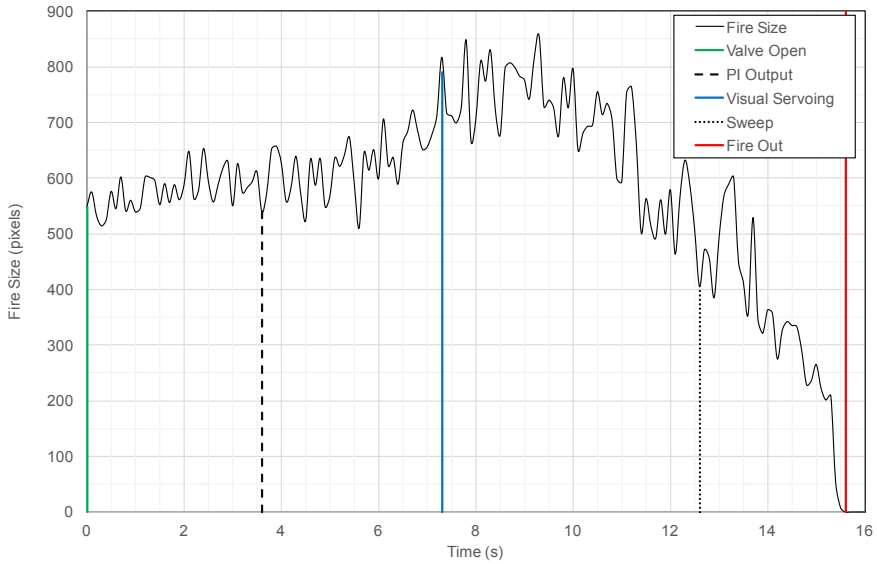

Figure 5.35. Fire size and target row versus time for Test 19

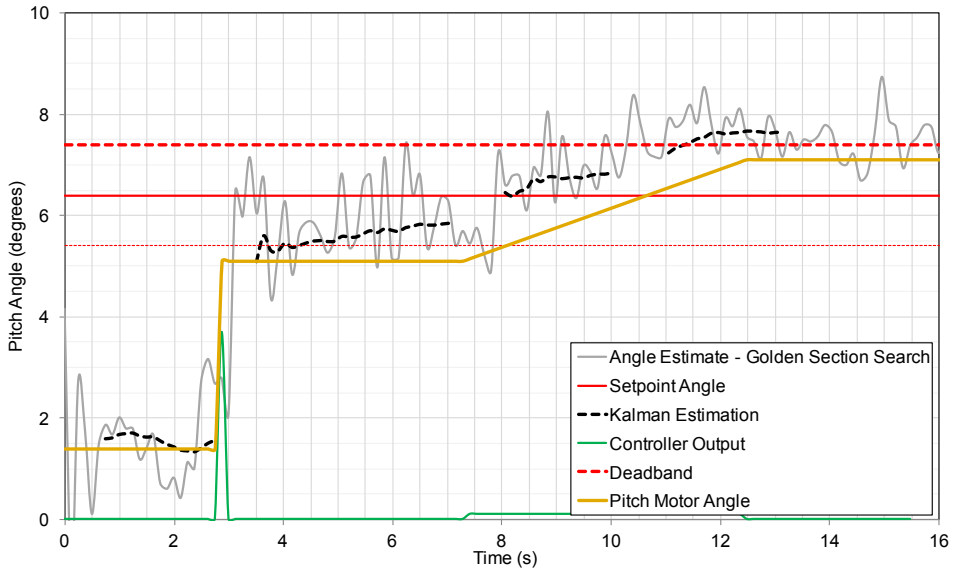

Figure 5.36. Control response for Test 19.

5.8 Discussion

The trajectory model used in the system was able to provide an acceptable approximation of the spray path given the results of tests performed without initial offsets introduced. The decision based controller proposed was able to effectively manipulate the nozzle given some errors in targeting and the spray path. Pressure was not measured continuously in the system as the pressure in a suppression system is often regulated and kept constant. Due to some fluctuation in the back pressure of the system the actual spray location differed from the trajectory model slightly but this is accounted for by predicting the effective pitch angle. The system processes two IR images and does all computations in approximately 100 ms. The processing time will increase depending on the amount of objects in the image needed to classify. The longest processing step is the calculation of the normalized GLCM for second order feature analysis. This is due to the method of searching neighboring pixels for every pixel within a segmented ROI. The classification stage including GLCM calculation and probability analysis is approximately 8 times longer than the pre-processing step of segmenting pixels of interest and morphologically filtering.

For Tests 1-6, the initial yaw and pitch angle were determined by minimizing the distance between the fire location height and distance and the spray trajectory model at the given fire

location. The spray model provided accurate results in the tests as the landing zone of the spray path often reached the fire location without having to adjust the motor positions of the yaw and pitch motors (Figure 5.21 and Figure 5.24) other than the sweeping pattern applied once the fire decayed by more than 50% the initial size at the start of the test. For the first fire location used the average suppression time was 10.66 s with a standard deviation of 4.89 s. The other fire locations including indoor environments and a far target (9.4 m) fell within the average times of the first fire position indicating location did not have a large effect on the total suppression time. The visual servoing control was necessary in 5 of the 8 tests. In some cases (Tests 1 and 4) it was used since the time spent sweeping the fire exceeded the 10 second limit set in the decision tree control scheme (Figure 5.21). The visual servoing mode will increase the pitch angle until the fire size decreases as underspray is more likely to occur in the system given pressure losses or errors in fire localization.

Visual servoing control for use in propagating fires was shown in in Tests 7 and 8. The approach was effective in fully suppressing a fire given an initial target at the center base and the average suppression time was 8.25 s with a standard deviation of 0.64 s. As shown in Figure 5.25 and Figure 5.26, the target row moves up in the image array, which causes the nozzle to increase the pitch angle to move in the direction of the new fire target. The control response in Figure 5.27 shows how visual servoing steps the pitch motor by 0.1 degrees as the target shifts upward. This approach does not require use of stereo processing throughout to continuously determine the fire distance as a stationary fire is assumed and limits processing time that would be necessary if constant stereo processing was necessary.

In Tests 9-20, an initial bias offset was introduced on the initial nozzle direction which forces the system to correct the position using the controller designed. The average initial response time in these tests was 2.82 s with a standard deviation of 0.89 s. The variation is due to an intermittent sampling rate in the system and different initial covariance and noise estimates. The image processing involved in each stage of the control process allowed the system to sample over 5 Hz but the sample rate was not discrete. For the first fire test location (tests 9-11), the average suppression time was 22.03 s with a standard deviation of 5.35 s. The other tests (12-20) had suppression times below the first fire location with the exception of Test 15 which yielded a time of 27.9 s. The longer times associated with the first fire location were a result of longer time spent in the sweeping pattern when a small portion (<10-20% initial fire size) of the wood crib was not

adequately reached by the spray. The sweeping motion will cover more area but the water density in the region around the fire decreases due to the decreased momentum of the flow along the spray length. In test 10, the nozzle was corrected twice by the PI controller after which the estimated spray angle (Kalman filtering) fell within the deadband limits but the fire size did not decrease by enough (>50%) to start sweeping. Visual servoing was used since the water undersprayed the fire and after 18.1 s the nozzle starting sweeping the fire.

Suppression times for indoor tests with offset conditions were lower (11.4 s) than outdoor environments with similar offset conditions (17.9 s). The increase in performance indoors may be the result of larger water mass flux rates reaching the closer fire locations used (6.4 m) as further distances and external conditions (i.e. wind) will increase spray breakup and reduce the amount of water reaching the targeted area of the fire.

Overall, the proposed approach showed that autonomous firefighting can be implemented in robotic systems for localized fire suppression. Given the design of humanoid robots, the nozzle and fire indicator and machine vision must be decoupled differing from fire monitors which often use a single fire indicator or camera mounted rigidly on top of a high pressure nozzle. The water classification and angle estimation provided a novel method of real time error estimation between the spray and fire target. Typically, autonomous systems do not account for errors where the suppressant does not reach any portion of the fire source.

5.9 Conclusion

A real-time autonomous fire suppression system with closed-loop control was proposed. The system was developed for use on a robotic firefighting platform for localized fire suppression operations. A probabilistic water classification method was implemented along with stereo processing to localize points along the spray as a technique of estimating the yaw and pitch angle for every time step. A Golden Section Search method with linear least squares optimization was used to determine the optimal angle to fit a spray trajectory model to the 3D points along the spray path. A PI controller was used to control the error between the current angle of the nozzle and desired path by filtering the estimated yaw and pitch angles. The control output is event-driven based on a deadband on the desired angles and the covariance value of a Kalman filter. To control the suppression process, a decision tree was used to determine the optimal approach to manipulate

the spray nozzle. The states of the system include: oscillation of the nozzle given a sharp decrease in fire size, PI control output if the error between the estimated angle and desired angle fall outside the deadband of the controller, visual servoing if the sweeping pattern is prolonged or current estimation places the nozzle at the correct angle but fire size has not decreased, and completion once the fire size has dropped to 0.

Experiments were performed to show the response of the system with wood-crib fires. A total of 8 tests demonstrated performance of the spray model and control process given an accurate initial orientation of the spray nozzle. By comparing total time to suppression of the various fire locations (11.6 s) to the suppression times of first fire location used (10.7 s), the location does not effect suppression times. This included indoor versus outdoor environments and elevated versus ground level fire locations. A total of 12 tests demonstrated performance of the system given a forced offset to the initial nozzle orientation resulting in an error between the spray location and the fire target. The total time to suppression increased in these tests (15.7 s) compared to the tests performed without initial offset (11.3 s) due to the system having to correct for initial bias errors of up to 5 degrees in yaw, pitch, or both directions. The average response time for the system to estimate and adjust the spray angle was 2.82 s. In tests with offset conditions, suppression times for indoor tests (11.4 s) were lower than those of outdoor tests (17.9 s). The time spent in a sweeping pattern was lower in the indoor tests as well. Overall, the method of estimating the water pitch and yaw angle combined with Kalman filtering and PI control provided an accurate technique of adjusting the spray nozzle to reach the fire target. The autonomous suppression method can be further developed for various fire scenarios and implemented onto a humanoid robotic platform or in a stand alone system.

6 Conclusions

This work has presented autonomous fire suppression strategies for an intelligent firefighting robot. Real-time suppression algorithms were developed using feedback control for intelligent and robust suppression of wood-crib fires.

In Chapter 2, a suppression control algorithm was presented for use in close-proximity fire suppression scenarios. The method uses IR thermography for fire detection and in a stereo pair for localization which provides a 3D target location of the fire. In many other systems, the fire distance is not determined but knowledge of the location can be used to better angle a spray system for accurate targeting. To reduce computation time, the fire is localized once to avoid stereo processing at every image sampling time. Feedback of the fire size and target (row and pixel) are used to employ a visual servoing strategy that adjusts a water nozzle based on changes in the fire target. A linear assumption is used to simplify the spray trajectory between the nozzle origin and the fire base as the need for a deterministic model is not necessary given large water pressures and flow rates. Full-scale tests were performed in high and low visibility environments to show performance of the system in varying firefighting scenarios. The system outperformed an operator as the suppression times for the system in low visibility were 4.5 s and the time for an operator to fully suppress the fire were 14.8 s. Offsets were also forced on the initial placement of the nozzle to place the water spray off-target of the fire base. With the offset parameters, suppression times did not vary significantly (4.5 s) from tests without offset conditions (3.7 s) in clear and low visibility test conditions. This showed that IR cameras can be used in fire detection and suppression systems without noticeable increases in suppression times even in very dense smoke environments in which other sensors (visual, LIDAR) will fail and a visual servoing technique is useful in actuating the nozzle to target a shifting location of the fire to suppress.

In Chapter 3, combinations of features were analyzed for use in the classification of water spray and leaks using thermal images. Texture features were extracted from objects segmented using a three frame-differencing method to threshold areas of high variance between frames. Other techniques of segmentation (background subtraction, optical flow) failed to show high performance due to the necessity of implementation in a real-time system that will show small movements between frames due to robot dynamics. Bayesian classification was performed to probabilistically identify water and non-water high variance objects during real-time processing.

Resubstitution and cross-validation error were used as objective functions in multi-objective optimization. Various environments and backgrounds were used in the training dataset with water sprays and leak at different temperatures and internal densities and a combination of Haralick texture features (autocorrelation, dissimilarity, inverse difference normalized, and max probability) selected in probabilistically classifying water vs non-water objects. The classification method was used on a test dataset to show performance in identifying water in IR videos and the results showed a 94.2-97.4% accuracy rate using recall, precision, F-measure, and G-measure. The classification method was shown to be effective in segmenting water in IR images which can then be implemented in spray applications where knowledge of the spray location will result in more efficient spray operations.

In Chapter 4, a spray trajectory model was introduced and validated against videos of the spray pattern used in the firefighting system. The model is scaled down to a 2D space to give the spray height for any given distance. Autonomous systems do not use spray models to predict the optimal attack angle of fire nozzles but in long range operations this was found to be necessary to better initialize the nozzle position to reach a targeted fire. The classification method in Chapter 3 is used to binarize left and right IR images and an epipolar constraint is used to determine disparity values associated with the spray path. The simplified pixel matching approach was necessary as processing times in IR stereovision will limit the real-time application of a feedback-based suppression algorithm. The disparity map is converted to distance to create 3D points of the spray in the FOV. The yaw and pitch angles of the spray for each iteration in a real-time system are estimated using a Golden Section Search for optimization which can be used to correct for errors associated with motor bias or improper grasps of a fire nozzle by a robotic hand.

In Chapter 5, an autonomous fire suppression algorithm was presented and experimentally validated for a variety of firefighting scenarios. The system includes a number of image processing techniques including: fire detection and localization, trajectory modeling, water classification, real-time estimation of the spray path, visual servoing, and feedback control. A decision tree controller is used to intelligently select the behavior of the nozzle controller to take in order to effectively and efficiently suppress a Class A wood-crib fire. A Kalman Filter was used to give an estimation of the spray angle in yaw and pitch directions. The measurements or estimated angles used in the Kalman Filter are estimations of the spray angle from the trajectory model and IR vision system provided depth map with a Golden Section Search optimization process. It was

found that a short sampling period (approximately 2 seconds) resulted in higher confidence of the actual spray angle as the initial burst of spray or movement of the nozzle results in higher noise of the angle estimated. The sampling time may be decreased if a more robust water classification technique is able to provide more accurate estimates of the spray angle without high levels of noise associated with them. A PI controller was used to correct for errors in nozzle direction given a desired spray angle (trajectory model with localized fire target) and current estimation of the spray angle (Kalman Filter). The system was tested in various conditions with the fire located at different distances and heights. For a single fire location (outdoors) suppression times were 10.7 s with a standard deviation of 4.9 s. Other fire locations outdoors and indoors resulting in suppression times within the same range showing negligible effect of location on total time to suppress the fire. Forced offsets to the initial placement of the spray were introduced to show the response of the system if the spray does not initially reach any part of the fire as a condition that may happen in robotic firefighting if the nozzle is gripped improperly or shifts during operation due to high torque associated with moving the fully charged water line. Suppression times for the first fire location with up to 5 degree offsets applied to both yaw and pitch angle were 22.0 s which were longer than the other test locations. This was due to more time spent sweeping the nozzle in order to suppress small sections of the fire continuing to be detected even though a large percentage of the fire (>75%) had been suppressed. Indoor fire location yielded shorter suppression times (11.4 s) as the fire placed closer to the system with no external disturbances (i.e. wind) results in less spray breakup at the fire location and a larger rate of water applied to the base of the fire.

7 Future Work

The suppression algorithm with feedback control can used in future work to further develop robotic firefighting systems. As many fire monitors currently do not use feedback control or spray tracking, the developed methods may improve performance and efficiency due to more knowledge of the environment in which they operate. The other area of application is in humanoid firefighting robots. Since the methods sought to provide a real-time approach to error correction of spray angle, improper gripping of a nozzle can be accounted for by estimating the spray direction. The nozzle pose in a gripper may not be able to be calculated precisely enough to account for the bias in the nozzle direction (yaw and pitch) and the hand orientation. One larger issue in implementation onto such a platform is the robot dynamics shifting the vision system during operation. Small shifts in the IR cameras was accounted for since the stationary platform used in the tests also shifted when the nozzle changed directions. With the frame differencing technique applied in water classification, faster frame rates will result in better performance as shifts in the camera will result in more perceived moving objects in the scene than just water sprays or smoke.

Other future work may seek to evaluate larger nozzles and flow rates than used in this work. For fire monitoring onboard ship decks or in large open warehouses, higher pressure systems will be necessary for the suppressant to reach fires located much further away from the vision system (>10-20 m). Similar approaches will be applicable as the trajectory model used can be fit to other spray conditions (pressure, flow rate) given some knowledge of the landing zone for various spray angles. Wind conditions can also be monitored and included in the trajectory model as the direction and magnitude of the wind may be resolved to push the spray left or right or back and forth.

The controller designed in this work may also be evaluated in larger fire scenarios where the fire may propagate due to pushing of the fire base by the water spray or fire spread onto nearby combustible material. Since the visual servoing control process seeks to follow the fire target as it shifts in the image array during suppression, propagating fires should be suppressed in reasonable times without errors where the spray direction moves further away from the target. The angle estimation process can be used in these situations to indicate the direction is erroneous and re-targeting can be performed. Another scenario to design the system for is a multi-fire environment. The existing controller can be further developed to label a number of detected fires if present and apply a strategy such as suppression of the larger or closer fire initially. Upon complete suppression

of one fire, the system could apply knowledge of the current yaw and pitch direction of the nozzle with information about the second fire location to intelligently output a motor output to direct the spray onto the new target and then begin the feedback control process once again.

Another area to further study is in monitoring an area where fire was initially located for re-ignition. In fire monitors or humanoid firefighting, the fire will not always be in clear view of the sensors used to detect fire. Blockages may prevent the vision system from determining where to apply the water spray while other sensors indicate a fire is still present in the area. This would require further developments in robot intelligence such as searching the space given a map of the environment beforehand (LIDAR) either by the robot building a map of the space beforehand or with other devices such as quadcopters providing additional support. If only the area of the fire initially visible to the robot is suppressed but there is still a strong indication that a fire is present in the space (external fire detection system) knowledge of obstacle and the fire location initially can provide information for the robot to navigate the space to seek a reasonable position to continue firefighting operations.

References

[1] NFPA, *Deadliest Fires in the U.S. with 5 or more Firefighter Deaths at the Fire Grounds, 1977-2012*: Fire Incident Data Organization, 2013.

[2] Karter Jr, Michael J., and Joseph L. Molis. "Firefighter Injuries in the United States, 2013." (2014).

[3] Fahy, R., P. Leblanc, and J. Molis. "Firefighter fatalities in the United States, 2013. National Fire Protection Association." (2014).

[4] M. J. Karter, *Fire loss in the United States during 2013*: National Fire Protection Association Quincy, MA, 2014.

[5] M. J. Karter, "Selected Special Analyses of Firefighter Fatalities," National Fire Protection Association Quincy, MA2005.

[6] E. Ronchi, S. Gwynne, D. Purser, and P. Colonna, "Representation of the impact of smoke on agent walking speeds in evacuation models," *Fire technology,* vol. 49, pp. 411-431, 2013.

[7] J. L. Bryan, "Behavioral response to fire and smoke," *SFPE handbook of fire protection engineering,* vol. 2, 2002.

[8] M. Wright, G. Cook, and G. Webber, "The effects of smoke on people's walking Speeds using overhead lighting and Wayguidance provision," in *Proceedings of the 2nd international symposium on human behaviour in fire. MIT, Boston*, 2001, pp. 275-284.

[9] T. Jin, "Visibility through fire smoke (No. 42): report of Fire Research Institute of Japan," 1976.

[10] K. Miyazawa, "Fire robots developed by the Tokyo Fire Department," *Advanced Robotics,* vol. 16, pp. 553-556, 2002.

[11] C. F. Tan, M. Alkahari, and A. Rahman, "Development of Ground Vehicle for Fire Fighting Purpose," 2011.

[12] J. Suthakorn, S. Shah, S. Jantarajit, W. Onprasert, W. Saensupo, S. Saeung*, et al.*, "On the design and development of a rough terrain robot for rescue missions," in *Robotics and Biomimetics, 2008. ROBIO 2008. IEEE International Conference on*, 2009, pp. 1830-1835.

[13] D. Longo and G. Muscato, "CLAWAR WP3 Applications: Natural/Outdoor and Underwater Robots," in *Climbing and Walking Robots*, ed: Springer, 2005, pp. 1159-1170.

[14] J. H. Hong, B.-C. Min, J. M. Taylor, V. Raskin, and E. T. Matson, "NL-based communication with firefighting robots," in *Systems, Man, and Cybernetics (SMC), 2012 IEEE International Conference on*, 2012, pp. 1461-1466.

[15] P. H. Chang, Y. H. Kang, G. R. Cho, J. H. Kim, M. Jin, J. Lee*, et al.*, "Control architecture design for a fire searching robot using task oriented design methodology," in *SICE-ICASE, 2006. International Joint Conference*, 2006, pp. 3126-3131.

[16] T. N. Khoon, P. Sebastian, and A. B. S. Saman, "Autonomous Fire Fighting Mobile Platform," *Procedia Engineering,* vol. 41, pp. 1145-1153, 2012.

[17] Y. D. Kim, Y. G. Kim, S. H. Lee, J. H. Kang, and J. An, "Portable fire evacuation guide robot system," in *Intelligent Robots and Systems, 2009. IROS 2009. IEEE/RSJ International Conference on*, 2009, pp. 2789-2794.

[18] Liu JX, Chen XB, "Design of fire targeting device for large space auto tracking jet suppression system," Science and Technology Innovation Herald, 2013, 11:243-246.

[19] Chen, Tao, et al. "An automatic fire searching and suppression system for large spaces." Fire safety journal 39.4 (2004): 297-307.

[20] Xin YB, Thumuluru S, Jiang FH, Yin R, “An experimental study of automatic water cannon systems for fire protection of large open spaces,” Fire Technology, 2014, 50:233-248.
[21] Kim, Jong-Hwan, Joseph W. Starr, and Brian Y. Lattimer. "Firefighting Robot Stereo Infrared Vision and Radar Sensor Fusion for Imaging through Smoke." Fire Technology: 1-23.
[22] Starr, Joseph W., and B. Y. Lattimer. "Application of thermal infrared stereo vision in fire environments." Advanced Intelligent Mechatronics (AIM), 2013 IEEE/ASME International Conference on. IEEE, 2013.
[23] Kim, Jong-Hwan, Brian Keller, and Brian Y. Lattimer. "Sensor fusion based seek-and-find fire algorithm for intelligent firefighting robot." Advanced Intelligent Mechatronics (AIM), 2013 IEEE/ASME International Conference on. IEEE, 2013.
[24] Starr, Joseph W., and B. Y. Lattimer. "Evaluation of navigation sensors in fire smoke environments." Fire Technology 50.6 (2014): 1459-1481.
[25] Starr, Joseph W., and Brian Y. Lattimer. "A comparison of IR stereo vision and LIDAR for use in fire environments." Sensors, 2012 IEEE. IEEE, 2012.
[26] McNeil, Joshua G., Joseph Starr, and Brian Y. Lattimer. "Autonomous fire suppression using multispectral sensors." Advanced Intelligent Mechatronics (AIM), 2013 IEEE/ASME International Conference on. IEEE, 2013.
[27] Penders J, Alboul L, Witkowski U, Naghsh A, Saez-Pons J, Herbrechtsmeier S, El-Habbal M (2011) A robot swarm assisting a human fire-fighter. Advanced Robotics 25 (1-2):93-117
[28] Liljeback P, Stavdahl O, Beitnes A (2006) SnakeFighter - Development of a Water Hydraulic Fire Fighting Snake Robot.
[29] Pack DJ (2004) Fire-fighting mobile robotics and interdisciplinary design-comparative perspectives. IEEE Transactions on Education 47 (3)
[30] Dearie S, Fisher K, Rajala B, Wasson S Design and construction of a fully autonomous fire fighting robot. Electrical Insulation Conference and Electrical Manufacturing; Coil Winding Conference, 2001 Proceedings. IEEE, 2001
[31] Rehman A, Masood N, Arif S, Shahbaz U, Sarwar F, Maqsood K, Imran M, Pasha M (2012) Autonomous Fire Extinguishing System. Robotics and Artificial Intelligence (ICRAI), 2012 International Conference on
[32] Yuan F (2010) An integrated fire detection and suppression system based on widely available video surveillance. Machine Vision and Applications 21 (6):941-948. doi:10.1007/s00138-010-0276-x
[33] De Santis A, Siciliano B, Villani L (2007) A unified fuzzy logic approach to trajectory planning and inverse kinematics for a fire fighting robot operating in tunnels. Intelligent Service Robotics 1 (1):41-49. doi:10.1007/s11370-007-0003-2
[34] Qureshi WS, Ekpanyapong M, Dailey MN, Rinsurongkawong S, Malenichev A, Krasotkina O (2015) QuickBlaze: Early Fire Detection Using a Combined Video Processing Approach. Fire Technology. doi:10.1007/s10694-015-0489-7
[35] Töreyin BU, Dedeoğlu Y, Güdükbay U, Çetin AE (2006) Computer vision based method for real-time fire and flame detection. Pattern Recognition Letters 27 (1):49-58. doi:10.1016/j.patrec.2005.06.015
[36] Phillips Iii W, Shah M, da Vitoria Lobo N (2002) Flame recognition in video. Pattern recognition letters 23 (1):319-327

[37] Çelik T, Demirel H (2009) Fire detection in video sequences using a generic color model. Fire Safety Journal 44 (2):147-158. doi:10.1016/j.firesaf.2008.05.005
[38] Ko B, Cheong K-H, Nam J-Y (2010) Early fire detection algorithm based on irregular patterns of flames and hierarchical Bayesian Networks. Fire Safety Journal 45 (4):262-270. doi:10.1016/j.firesaf.2010.04.001
[39] Amon F, Benetis V, Kim J, Hamins A Development of a performance evaluation facility for fire fighting thermal imagers. In: Defense and Security, 2004. International Society for Optics and Photonics, pp 244-252
[40] Amon F, Bryner N, Hamins A Evaluation of thermal imaging cameras used in fire fighting applications. In: Defense and Security, 2004. International Society for Optics and Photonics, pp 44-53
[41] Amon F, Ducharme A (2008) Image Frequency Analysis for Testing of Fire Service Thermal Imaging Cameras. Fire Technology 45 (3):313-322. doi:10.1007/s10694-008-0060-x
[42] Maxwell FD (1971) A portable IR system for observing fire thru smoke. Fire Technology 7 (4):321-331
[43] Lasaponara R, Cuomo V, Macchiato M, Simoniello T (2003) A self-adaptive algorithm based on AVHRR multitemporal data analysis for small active fire detection. International Journal of Remote Sensing 24 (8):1723-1749
[44] Thomas PJ, Nixon O (1993) Near-infrared forest fire detection concept. Applied optics 32 (27):5348-5355
[45] Wieser D, Brupbacher T (2001) Smoke detection in tunnels using video images. NIST SPECIAL PUBLICATION SP:79-90
[46] Sentenac T (2002) Evaluation of a charge-coupled-device-based video sensor for aircraft cargo surveillance. Optical Engineering 41 (4):796. doi:10.1117/1.1459450
[47] Bertozzi M, Broggi A, Caraffi C, Del Rose M, Felisa M, Vezzoni G (2007) Pedestrian detection by means of far-infrared stereo vision. Computer Vision and Image Understanding 106 (2-3):194-204. doi:10.1016/j.cviu.2006.07.016
[48] Hajebi K, Zelek JS Sparse disparity map from uncalibrated infrared stereo images. In: Computer and Robot Vision, 2006. The 3rd Canadian Conference on, 2006. IEEE, pp 17-17
[49] Grant G, Brenton J, Drysdale D (2000) Fire suppression by water sprays. Progress in energy and combustion science 26 (2):79-130
[50] DiNenno P (1995) SFPE Handbook of Fire Protection Engineering National Fire Protection Association. 3rd.
[51] Walker D, Zhang X, Kung P, Saxler A, Javadpour S, Xu J, Razeghi M (1996) AlGaN ultraviolet photoconductors grown on sapphire. Applied Physics Letters 68 (15):2100. doi:10.1063/1.115597
[52] Zhang S, Wang W, Shtau I, Yun F, He L, Morkoc H, Zhou X, Tamargo M, Alfano R (2002) Backilluminated GaN/AlGaN heterojunction ultraviolet photodetector with high internal gain. Applied physics letters 81:4862
[53] Zhang JP, Hu X, Bilenko Y, Deng J, Lunev A, Shur MS, Gaska R, Shatalov M, Yang JW, Khan MA (2004) AlGaN-based 280 nm light-emitting diodes with continuous-wave power exceeding 1 mW at 25 mA. Applied Physics Letters 85 (23):5532. doi:10.1063/1.1831557
[54] Acroname.com Hamamatsu Flame Sensor UVTRON http://www.acroname.com /robotics/parts/R66-R2868.pdf

[55] Kim J-H, Lattimer BY (2015) Real-time probabilistic classification of fire and smoke using thermal imagery for intelligent firefighting robot. Fire Safety Journal 72:40-49. doi:10.1016/j.firesaf.2015.02.007
[56] Miyashita T, Sugawa O, Imamura T, Kamiya K, Kawaguchi Y (2014) Modeling and analysis of water discharge trajectory with large capacity monitor. Fire Safety Journal 63:1-8. doi:10.1016/j.firesaf.2013.09.028
[57] Nomura K, Koshizuka S, Oka Y, Obata H (2001) Numerical Analysis of Droplet Breakup Behavior using Particle Method. Journal of Nuclear Science and Technology 38 (12):1057-1064. doi:10.1080/18811248.2001.9715136
[58] Pastor, Jose V., Jean Arregle, and Alberto Palomares. "Diesel spray image segmentation with a likelihood ratio test." *Applied Optics* 40.17 (2001): 2876-2885.
[59] Jeong, Haeyoung, Kihyung Lee, and Yuji Ikeda. "Investigation of the spray characteristics for a secondary fuel injection nozzle using a digital image processing method." *Measurement Science and Technology* 18.5 (2007): 1591.
[60] Nanda, Harsh, and Larry Davis. "Probabilistic template based pedestrian detection in infrared videos." *IEEE Intelligent Vehicle Symposium*. Vol. 1. 2002.
[61] Shao, Jiaqing, and Yong Yan. "Digital imaging based measurement of diesel spray characteristics." *Instrumentation and Measurement, IEEE Transactions on* 57.9 (2008): 2067-2073.
[62] Zhao-dong, An Cheng-jin Niu, and Li Zhi-jun Chen Zeng-ping. "Otsu Threshold Comparison and SAR Water Segmentation Result Analysis [J]." *Journal of Electronics & Information Technology* 9 (2010): 033.
[63] KANG, Huai-qi, and Bao-guo CHEN. "Improved Otsu Segmentation Algorithm for IR Image Based on Fractal Algorithm [J]." *Infrared Technology* 6 (2009): 014.
[64] C. Stauffer, and W. E. L. Grimson, "Learning patterns of activity using real-time tracking", IEEE PAMI 22(8) (2000), pp. 747–757.
[65] Latecki, Longin Jan, Roland Miezianko, and Dragoljub Pokrajac. "Tracking motion objects in infrared videos." *Advanced Video and Signal Based Surveillance, 2005. AVSS 2005. IEEE Conference on*. IEEE, 2005.
[66] L. Matthies, P. Bellutta, and M. McHenry, "Detecting water hazards for autonomous off-road navigation," Proceedings of SPIE, Vol. 5083, Orlando, FL, pp. 231-242, April 2003.
[67] M. Iqbal, O. Morel, and F. Meriaudeau, "A survey of outdoor water detection," The 5th International Conference on Information & Communication Technology and Systems (ICTS), Indonesia, 2009.
[68] A. Pandian, "Robot navigation using stereo vision and polarization imaging," Masters thesis, Institut Universitaire de Technologie IUT Le Creusot, Universite de Bourgogne, 2008.
[69] A. Sarwal, J. Nett, and D. Simon, "Detection of small water bodies," PercepTek Robotics Technical Report, Littleton, CO, (Available at: http://www.dtic.mil, AD# ADA433004), 2004.
[70] B. Xie, Z. Xiang, H. Pan, and J. Liu, "Polarization-based water hazard detection for autonomous off-road navigation," Proceedings of the IEEE/RSJ International Conference on Intelligent Robots and Systems, San Diego, CA, pp. 3186-3190, 2007.
[71] H. Kwon, D. Rosario, N. Gupta, M. Thielke, D. Smith, P. Rauss, P. Gillespie, and N. Nasrabadi, "Hyperspectral Imaging and Obstacle Detection for Robotics Navigation" U.S. Army Research Laboratory Technical Report #ARL-TR-3639, September 2005.

[72] T. Hong, S. Legowik, and M. Nashman, “Obstacle Detection and Mapping System,” National Institute of Standards and Technology (NIST) Technical Report NISTIR 6213, pp. 1-22, 1998.
[73] T. Hong, C. Rasmussen, T. Chang, and M. Shneier, “Fusing Ladar and Color Image Information for Mobile Robot Feature Detection and Tracking,” 7th International Conference on Intelligent Autonomous Systems, Marina Del Ray, CA, 2001.
[74] M. Fischler, C. Connolly, and R. Bolles. Unpublished work performed during the U.S. Army Research Laboratory funded Robotics Collaborative Technology Alliances program by SRI International, Menlo Park, CA, 2004.
[75] Rankin, Arturo, and Larry Matthies. "Daytime water detection based on color variation." *Intelligent Robots and Systems (IROS), 2010 IEEE/RSJ International Conference on*. IEEE, 2010.
[76] Santana, Pedro, Raphael Mendonca, and José Barata. "Water detection with segmentation guided dynamic texture recognition." *Robotics and Biomimetics (ROBIO), 2012 IEEE International Conference on*. IEEE, 2012.
[77] Qiao, Cheng, et al. "An adaptive water extraction method from remote sensing image based on NDWI." *Journal of the Indian Society of Remote Sensing* 40.3 (2012): 421-433.
[78] Mettes, Pascal, Remco Veltkamp, and Robby Tan. "On the segmentation and classification of water in videos." *9th International Conference on Computer Vision Theory and Applications*. 2014.
[79] Minghan, Zhu, Luo Dayong, and Cao Qianxia. "Moving objects detection algorithm based on two consecutive frames subtraction and background subtraction [J]." *Computer Automated Measurement & Control* 3 (2005).
[80] F. Yuan, "Video-based smoke detection with histogram sequence of LBP and LBPV pyramids," *Fire safety journal,* vol. 46, pp. 132-139, 2011.
[81] R. M. Haralick, K. Shanmugam, and I. H. Dinstein, "Textural features for image classification," *Systems, Man and Cybernetics, IEEE Transactions on,* pp. 610-621, 1973.
[82] M. K. Tsatsanis and G. B. Giannakis, "Object and texture classification using higher order statistics," *IEEE Transactions on Pattern Analysis and Machine Intelligence,* vol. 14, pp. 733-750, 1992.
[83] Boland, M.V.: Quantitative description and automated classifica- tion of cellular protein localization patterns in fluorescence micro- scope images of mammalian cells. Ph.D. Thesis, Carnegie Mellon University, Pittsburgh (1999)
[84] Clausi, D.A.: An analysis of co-occurence texture statistics as a function of grey level quantization. Can. J. Remote Sensing **28**(1), 45–62 (2002)
[85] Soh, L.-K., Tsatsoulis, C.: Texture analysis of SAR sea ice imagery using gray level co-occurrence matrices. IEEE Trans. Geosci. Remote Sensing **37**(2), 780–795 (1999)
[86] O. Kramer, "K-Nearest Neighbors," in *Dimensionality Reduction with Unsupervised Nearest Neighbors*, ed: Springer, 2013, pp. 13-23.
[87] P. Harrington, *Machine Learning in Action*: Manning Publications Co., 2012.
[88] D. J. Hand, H. Mannila, and P. Smyth, *Principles of data mining*: MIT press, 2001.
[89] Kotsiantis, Sotiris B., I. Zaharakis, and P. Pintelas. "Supervised machine learning: A review of classification techniques." (2007): 3-24.
[90] F. Van Der Heijden, R. Duin, D. De Ridder, and D. M. Tax, *Classification, parameter estimation and state estimation: an engineering approach using MATLAB*: John Wiley & Sons, 2005.

[91] R. Kohavi, "A study of cross-validation and bootstrap for accuracy estimation and model selection," in *IJCAI*, 1995, pp. 1137-1145.
[92] K. Deb, *Multi-objective optimization using evolutionary algorithms* vol. 16: John Wiley & Sons, 2001.
[93] Li, Zhonghai, and Jianwei Li. "Control system design of directional fire-fighting monitor based on video." *Control and Decision Conference (CCDC), 2015 27th Chinese*. IEEE, 2015.
[94] Fincke, James Russell, et al. "Diagnostics and control in the thermal spray process." *Surface and Coatings Technology* 146 (2001): 537-543.
[95] T. Miyashita, O. Sugawa, Y. Wada, Y. Kawaguchi, Three-dimensional simulation model for water and fire-foam discharge using MPS method, J. Jpn. Soc. Saf. Eng., Jpn. Soc. Saf.Eng. (JSSE) 51 (2) (2012) 96–105.
[96] T. Miyashita, O. Sugawa, Y. Wada, R. Ishikawa, Y. Kawaguchi, Development of two-dimensional simple simulation model and evaluation of discharge ability for water discharge of firefighting, Bull. Jpn. Assoc. Fire Sci. Eng. (JAFSE) 62 (1) (2012) 13–19.
[97] S. Koshizuka, MPS Method, JSCES, MARUZEN Publishing Corp (2005) 63–66 (pp. 1–28).
[98] T. Miyashita, R. Ishikawa, O. Sugawa, T. Imamura, K. Kamiya, Y. Kawaguchi, 2011. Development of simulation model for water and fire-foam discharge using MPS method, in: Proceedings of Asia Pacific Symposium on Safety (APSS2011), The Korean Society of Safety, pp. 254–257.
[99] R. Ishikawa, T. Miyashita, O. Sugawa, T. Imamura, K. Kamiya, 2011. Experi- mental study of the water discharge behavior for firefighting, in: Proceedings of Asia Pacific Symposium on Safety (APSS2011), The Korean Society of Safety, pp. 340–343.
[100] Vajda, Steven. *Fibonacci and Lucas numbers, and the golden section: theory and applications*. Courier Corporation, 2007.
[101] Arora, Jasbir. *Introduction to optimum design*. Academic Press, 2004.
[102] Khan, M. J., Imam, M. R., Uddin, J., & Sarkar, M. R. (2012, December). Automated fire fighting system with smoke and temperature detection. In*Electrical & Computer Engineering (ICECE), 2012 7th International Conference on* (pp. 232-235). IEEE.
[103] Manjunatha, K. C. (2015). Implementation of Computer Vision Based Industrial Fire Safety Automation by Using Neuro-Fuzzy Algorithms.
[104] Liu, Xiao Xu, Xiao Li Huang, and Lin Cao. "The Design of Intellingent Fire Monitor System Based-On Digital Image." *Advanced Materials Research*. Vol. 433. 2012.
[105] Liu JX, Chen XB, “Design of fire targeting device for large space auto tracking jet suppression system,” Science and Technology Innovation Herald, 2013, 11:243-246.
[106] Chen, X., & Li, X. (2015, April). An automatic jet fire extinguishing device based on video. In *2015 International Conference on Mechatronics, Electronic, Industrial and Control Engineering (MEIC-15)*. Atlantis Press.
[107] B.C. Ko, K.H. Cheong, J.Y. Nam, Fire detection based on vision sensor and support vector machines, Fire Saf. J. 44 (2009) 322–329.
[108] T. Celik, H. Demirel, H. Ozkaramanli, M. Uyguroglu, Fire detection using statistical color model in video sequences,, J. Vis. Commun. Image Represent. 18 (2007) 176–185.
[109] T.H. Chen, Y.H. Yin, S.F. Huang, Y.T.Ye, The smoke detection for early fire alarming system base on video processing, in: Proceedings of the International Conference on

Intelligent Information Hiding and Multimedia Signal Processing, 2006. IIH-MSP'06, 2006.
[110] S. Verstockt, S. Van Hoecke, T. Beji, B. Merci, B. Gouverneur, A.E. Cetin, et al., A multi-modal video analysis approach for car park fire detection, Fire Saf. J. 57 (2013) 44–57.
[111] Y.-F. Li, J. Wikander, "Discrete-time sliding mode control of a dc motor and ball-screw driven positioning table," in *Proc. IFAC 15th Triennial World Congress, Barcelona Spain*, 2002, pp. 2436-2441.
[112] Wang, H. Van Brussel, J. Swevers, "Robust perfect tracking control with discrete sliding mode controller," *Journal of Dynamic Systems, Measurement, and Control*, vol. 125, no. 1, pp. 27-32, 2003.
[113] Drakunov, S., et al. "Nonlinear control of a rodless pneumatic servoactuator, or sliding modes versus Coulomb friction." *Automatica* 33.7 (1997): 1401-1408.
[114] Southward, Steve C., Clark J. Radcliffe, and C. R. MacCluer. "Robust nonlinear stick-slip friction compensation." *Journal of Dynamic Systems, Measurement, and Control* 113.4 (1991): 639-645.
[115] Patron, Roberto Salvador Felix, Ruxandra Mihaela Botez, and Dominique Labour. "Vertical profile optimization for the Flight Management System CMA-9000 using the golden section search method." *IECON 2012-38th Annual Conference on IEEE Industrial Electronics Society*. IEEE, 2012.